Faruk Geles

Non-local correlations in the Hubbard model and real material calculations

DOCTORAL THESIS

For obtaining the academic degree of

Doktor der Naturwissenschaften

Doctoral Programme of Natural Sciences
Technical Physics

Graz University of Technology

Supervisor:

Univ.- Prof. Dr. Enrico Arrigoni

Co-Supervisor:

Ass.- Prof. Dr. Markus Aichhorn

Institute of Theoretical and Computational Physics

Graz, December 2015

EIDESSTATTLICHE ERKLÄRUNG

AFFIDAVIT

Ich erkläre an Eides statt, dass ich die vorliegende Arbeit selbstständig verfasst, andere als die angegebenen Quellen/Hilfsmittel nicht benutzt, und die den benutzten Quellen wörtlich und inhaltlich entnommenen Stellen als solche kenntlich gemacht habe. Das in TUGRAZonline hochgeladene Textdokument ist mit der vorliegenden Dissertation identisch.

I declare that I have authored this thesis independently, that I have not used other than the declared sources/resources, and that I have explicitly indicated all material which has been quoted either literally or by content from the sources used. The text document uploaded to TUGRAZonline is identical to the present doctoral dissertation.

Datum / Date

Unterschrift / Signature

Abstract

Correlation effects show fascinating phenomena in many compounds, especially in materials with partially filled d-and f-bands. Since band theory within the density-functional theory (DFT) fails to describe the electronic states in these materials, in some cases even qualitatively, many-body methods have to be applied to deal with the electronic correlations. In this work, we use the variational cluster approximation (VCA) and other many body methods for this problem.

First we use the variational cluster approximation for the generation of a non-local correlation measure, which is applied on the 1D, 2D and 3D Hubbard model. There we see a clear hint towards exact limit direction of dynamical mean field theory (DMFT) in the infinite dimensions. In the 1D case non-local correlations are long ranged and they decay very slowly. But for the two dimensional case there is stonger decay of the long-range correlations. But the decay speed which is observed from the 1D case to the 2D case can not be observed from the 2D to 3D.

Next we study the effect of non-local electronic correlations at all length scales on the Mott-Hubbard metal insulator transition in the frustrated and unfrustrated 2D Hubbard model in collaboration. Therefore we use dynamical vertex approximation, lattice quantum Monte Carlo, and variational cluster approximation. We show that the long range antiferromagnetic fluctuations open a spectral gap in the paramagnetic phase of the two-dimensional Hubbard model. These antiferromagnetic fluctuations can be referred as "Slater-like paramagnons". They lead to an insulating phase in paramagnetic phase at low enough temperatures and there is no Mott-Hubbard metal insulator transition for any finite interaction U.

Finally we go a step further from the Hubbard model to the real material calculations. Starting from density-functional theory calculations, we construct a low-energy model by Wannier function construction. Adding multi-orbital Coulomb interactions, we arrive at a many-body Hamiltonian which is solved within the VCA. As a benchmark of the method, we compare our results with continuous-time quantum Monte Carlo (CT-QMC) calculations for the intensively studied vanadate $SrVO_3$. Compared to CT-QMC, the VCA has the advantage that its applicability and performance only slightly depends on the actual structure of the local interacting Hamiltonian. Therefore, full rotational invariant interactions as well as spin-orbit coupling can be treated much more efficiently. Applying this method, we investigate the influence of spin-orbit coupling on the electronic band structure and Fermi surfaces in ruthenates, e.g., $SrRuO_3$.

Kurzfassung

Korrelationseffekte bringen faszinierende Phänomene in vielen Materialen hervor, im Besonderen in Materialen mit teilweise gefüllten d- und f-Schalen. Die Bandtheorie innerhalb der Dichte Funktional Theorie (DFT) ist nicht in der Lage ist die elektronischen Zustände in diesen Materialen zu beschreiben. In vielen Fällen scheitert DFT sogar qualitativ, deswegen muss man Vielteichenmethoden für die Befassung von elektronischen Korrelationen verwenden. In diesem Arbeit verwenden wir die variationelle Cluster Näherung (VCA) und andere Vielteichenmethoden für dieses Problem.

Zuerst starten wir mit der Generierung eines Nicht-Localitätsmaßes für die Korrelationen. Diesen wenden wir auf das 1D, 2D, und 3D Hubard Modell. Dabei sehen wir eine klare Tendenz in Richtung der exakten Grenzfall von unendlichen Dimensionen von der dynamischen Molekularfeldnäherung (DMFT). Im eindimensionalen Fall sind die nicht lokale Korrelationen sehr reichweitig weil sie ein schwaches Abklingen mit der Distanz aufweisen. Aber im zweidimensionalen Fall beobachtet man ein starkes Abklingen von diesen lang-reichweitigen Korrelationen. Von 2D zum 3D gibt es noch immer eine Tendenz in Richtung von Aussterben der nicht lokalen Korrelationen aber diese ist verlangsamt.

Als Nächstes schauen wir den Impakt von elektronischen Korrelationen auf allen Längenskalen auf den Mott-Hubbard Metal Isolator Übergang im frustrierten und nicht frustrierten 2D Hubbard Modell. Dafür verwenden wir die dynamische Vertexnäherung, Gitter Quantum Monte Carlo und die variationelle Cluster Näherung. Wir sehen, dass die lang reichweitigen antiferromagnetischen Fluktuationen eine spektrale Lücke in der paramagnetischen Phase eröffnen. Diese antiferromagnetische Fluktuationen können als Slater-ähnliche Paramagnonen gesehen werden. Sie führen auf ein isolierendes Verhalten in der paramagnetischen Phase bei ausreichend niedrigen Temperaturen und es gibt keinen Mott-Hubbard Metal Isolator Übergang bei allen endlichen Wechselwirkungen U.

Am Ende gehen wir einen Schritt weiter von dem einfachen Hubbard Modell zu realistischen Material Berechnungen. Wie starten mit einer Diche Funktional Theorie Rechnung und dann konstruieren wir ein Nieder-Energie Modell durch die Wannier Konstruktion. Durch das Hinzufügen der Multi-Orbital Coulomb Wechselwirkungen gelangen wir zu einem Viel-Körper Hamilton, welches mit VCA gelöst wird. Als Benchmark-Test für diese Methode vegleichen wir unsere Ergebnisse mit kontinuierlichen Zeit Quantum Monte Carlo (CT-QMC) Rechnungen für das intensiv studierte Vanadat $SrVO_3$. Verglichen mit CT-QMC, VCA hat den Vorteil das dessen Leistung nur leicht von aktuellen Strucktur von lokalen Wechselwirkungshamilton abhängt. Deswegen können voll rotationssymmetrische Wechselwirkungen sowie Spin-Orbit Kopplung effizienter behandelt werden. Durch die Anwendung diese Methode können wir den Einfluss von Spin-Orbit Kopplung auf die elektronischen Bandstruktur und Fermioberfläche in Ruthenaten wie zum Beispiel $SrRuO_3$ untersuchen.

Contents

1 INTRODUCTION

Strong correlated electronic systems cannot be dealt with standard established solid state methods like density functional theory (DFT) implementations like the local density approximation (LDA)[1, 2] or generalized-gradient approximations (GGA)[3]. These systems are generally associated with compounds which contain partially filled d- and f-shell materials like the transition metals, rare earths and actinide elements and exhibit fascinating properties from the theoretical as well as from experimental point of view. In such class of materials the spectrum of these exciting phenomena range from one dimensional conductors, two dimensional high-T_C superconductivity in copper-oxides[4] and iron pnictides[5], huge volume collapses in $4f$ and $5f$ materials, metal-insulator transition in transition metal oxides to three dimensional heavy fermion materials.

These phenomena are observed by the powerful experimental techniques like the angle resolved photo emission spectroscopy (APPES), inverse photo emission spectroscopy, electron loss spectroscopy, Raman scattering, neutron scattering measurements. Also theoretical studies on simple models deliver much information concerning the physical mechanisms behind these exciting effects. Nevertheless to cut a long story in shot many of these effects can be traced back to the interplay between the kinetic and the interaction energy, which can be considered in the electronic models for correlated materials. Unfortunately it is very hard for find analytical solutions for these models. Therefore numerical methods have opened new possibilities out of this dilemma and have induced great progress.

For this area some very promising approaches have been devised in the last decades. One of the most encouraging methods is the dynamical mean field theory (DMFT)[6, 7], which includes the local correlations exact and neglects the non-local ones. For many applications and physical effects these non-local correlations are essential for an appropriate description. The inclusion of these non-local correlations is a great challenge from the mathematical and numerical point of view. Because of this there are different approaches to this problem. The first class of methods are based on cluster approaches or on cluster extensions of DMFT[8, 9, 10] and the second class of methods are based on diagrammatic techniques. In this work we will use the cluster methods like cluster perturbation theory (CPT)[11, 12] or variational cluster approximation (VCA)[13] and diagrammatic methods like the dynamical vertex approximation (DΓA)[14] and quantum Monte Carlo(QMC) methods for the investigation of the non-local correlations.

We proceed step by step and make many preparations for our investigation. The composition of this work is the following. In Chapter 2 some basics about the Green's functions are refreshed. It starts with the general form of the complicated many body Schrödinger equation. This equation can be simplified within the Born Oppenheimer approximation, which is still not solvable because of the electron-electron interactions

which lead to the correlation effects. The approximative solutions within the density functional theory (DFT) approach delivers Kohn Sham energies and eigenvalues which are related to the electronic band structures. Therefore we proceed with a short introduction into the reasons behind the band formation and their experimental verifications within the angle resolved photo emission spectroscopy. These measured quantities can be directly related to the Green's functions. Therefore we will give an overview over different type of Green's functions. Within the linear response theory it can be shown that the many body Green's function can be written as the expectation value of two operators. Using this we can introduce different kind of Green's function, which are useful for the many body description of the correlated electronic systems. Then we will show that the inclusion of non-local correlations is reflected into the momentum vector $\mathbf{k}$ dependency of the Green's function.

In Chapter 3 we will go into the details of the methods for the calculation of the many body Green's function in the respect of taking into account the local and non-local correlations. In DMFT non-local correlations are totally neglected. For the consideration of short-range correlations we start with the general form of the one-particle and two-particle operators, because the many body Hamiltonian of the solids consists out of these operators. Then we will go on with the setup for the exact diagonalization techniques based on Lanczos- and Band Lanczos algorithm. Because of the exponential increase of the basis states in the exact diagonalization we will go on with the CPT for the treatment of infinite large systems. The lack of a self-consistency condition prevents the application of this method to many problems with the symmetry-broken phases. Therefore this approach can be improved within the self-energy functional theory (SFA)[15] which includes a variational principle. Its application to clusters is referred to as VCA. Here we give also a small overview of the DΓA, which takes into account long range correlations. After this general overview of methods we can give a possible application of the VCA on the correlated materials. Therefore we use the DFT results as an input for the VCA calculations for the generation of an effective model, like the DFT+DMFT[16, 17, 18, 19] for the consideration of correlated materials. Therefore we use for the downfolding of the DFT results the maximally localized Wannier functions. At this point the only missing point is the determination of the external parameters of this effective model. This can be done by an ab-initio constrained RPA calculation.

In the following Chapter we use the VCA method for the construction of a non-locality correlation measure. We apply this axiomatically generated measure to the 1D, 2D, and 3D Hubbard model. Through this we can extract an estimate for the decrease of non-local correlations within dimensionality and cluster geometry.

In the Chapter 5 we consider the influence of the non-local correlations on the Mott-Hubbard metal-insulator transition in the 2D Hubbard model at half filling for the frustrated and unfrustrated cases. The main results obtained in this Chapter are calculated in collaboration and are published in Ref. [20]. There we compared the results from the DMFT, VCA, DΓA, and the extrapolating lattice Blankenbecler-Scalapino-Sugar (BSS)-QMC[21, 22] results. The necessary VCA results for this analysis were calculated within this thesis and DΓA calculations were done by our collaborators Thomas Schäfer, Alessandro Toschi, Karsten Held, Georg Rohringer and the BSS-QMC calculations were

done by Nils Blümer.

In the Chapter 6 we consider the DFT+VCA approach applied on the correlated compounds $SrVO_3$ and $SrRuO_3$ and compare this results with the very successful DFT+DMFT results. In the last Chapter we summarize and give an outlook for the prospective calculations.

2 THEORETICAL BACKGROUND

2.1 Introduction

In solid state physics the starting point is the Hamiltonian, which describes the whole physics of the many body system

$$\begin{aligned} H &= -\sum_{i}^{N_e} \frac{\hbar^2 \nabla_i^2}{2m_e} - \sum_{\alpha}^{N_i} \frac{\hbar^2 \nabla_\alpha^2}{2m_\alpha} - \frac{1}{4\pi\epsilon_0} \sum_{j=1}^{N_e} \sum_{\alpha=1}^{N_i} \frac{Z_\alpha e^2}{|r_j - R_\alpha|} + \frac{1}{4\pi\epsilon_0} \sum_{j<k}^{N_e} \frac{e^2}{|r_j - r_k|} \\ &+ \frac{1}{4\pi\epsilon_0} \sum_{\alpha,\beta}^{N_i} \frac{Z_\alpha Z_\beta}{|R_\alpha - R_\beta|}, \end{aligned} \tag{2.1}$$

where the first two terms describe electronic and ionic kinetic energies and the second two terms describe electron-ion and electron-electron interactions and the last term ion-ion interaction.

The next step is straightforward, as expected one writes down the many body Schrödinger equation and tries to solve this equation which is not possible. Therefore Born-Oppenheimer approximation, which says that the nuclei are much heavier and therefore much slower than the electrons is used to simplify this problem. Consequently, one can assume that electrons follow the configuration of the nuclei. The motion of electrons is important and the effect of nuclei becomes an external potential to the moving electrons. So one obtains the following much simpler Hamiltonian (in atomic units)

$$H = -\frac{1}{2} \sum_{i=1}^{N} \nabla_i^2 + \sum_{i=1}^{N} V(\mathbf{r_i}) + \frac{1}{2} \sum_{i=1}^{N} \sum_{j \neq i} \frac{1}{|\mathbf{r_i} - \mathbf{r_j}|}, \tag{2.2}$$

where $V(\mathbf{r_i}$ is the external potential, which is still difficult to solve because of the electron-electron interaction. Materials for which the electron-electron interaction is not sufficiently screened and where the electron-electron interaction is an important quantity are strongly correlated systems. The emerging correlation effects cannot be dealt with the methods mentioned above, because they are mainly based on the single electron picture. In order to get a solution out of these problems, methods which include the effects beyond single particle picture are needed. Correlation effect can be included more properly by the improvement of the approximation of the exchange correlation term[3, 23] in DFT, by diagrammatic methods or by construction of simple models, which can explain the physical nature of effects coming from correlations. The simplest model for the correlation physics is the well known Hubbard model:

$$H = -\sum_{i,j,\sigma} t_{ij} c_{i\sigma}^{\dagger} c_{j\sigma} + U \sum_{i} n_{i\uparrow} n_{i\downarrow} + \epsilon_0 \sum n_{i\sigma}, \tag{2.3}$$

which was proposed by three physicists (J. Hubbard, M. C. Gutzwiller, J. Kanamori) simultaneously for the explanation of the ferromagnetism in the $3d$ transition metals[24, 25, 26]. In this chapter we start with some basics about the nature of the electronic structure i.e. band formation in compounds and the effect of correlations on the band structure using the references [27, 28]. Then we will proceed with the mathematical description of the correlations by the method of Green's functions and the extraction of important information out of the Green's functions according to the references [29, 30]. The level of correlations which can be captured is reflected in the approximation within the calculation of the Green's function. This leads to some restrictions for the description of physical effects where long range correlations are the driving force. Therefore we will proceed step by step and analyze the development of such effects with regard to correlations, which is taken into account. This opens new possibilities for the description of many phenomena, which will be clarified in the next chapter.

2.2 Many body theory of electronic structure

The physical origin of the electronic band structure can be explained in the following two ways. In the first variant one starts with atoms which are brought together to form a crystal. At this point discrete energy levels of these atoms split into groups of levels which then form energy bands. In the second option the starting point is the free homogeneous electron gas, but through the influence of the lattice potential the continuous energy spectrum of the free electron gas is broken at certain characteristic energies and momenta because at their passage through the crystal the electrons suffer Bragg reflexions from the lattice. In this approach the solid can be understood as an electron gas which is subjected to the periodic potential of ions. This kind of consideration of a solid is demonstrated in the following sketch in figure 2.1.

Typically the word ion is referring to the nuclei and core electrons which are tightly bound in closed shells. From the considerations of an ideal reference system i.e. homogeneously distributed electrons and ions and free valence electrons some basic concepts can be derived which can be also transferred to an interacting system of electrons. These are the concept of Fermi energy E_F, density of states in an energy interval which are connected to the Pauli's exclusion principle, Fermi Dirac distribution of fermions. Let us start with some assumption that the ions and electrons are homogeneously distributed and the valence electrons can be considered as free particles, which fulfill the one particle Schrödinger equation with the solutions

$$\psi_{\mathbf{k},s}(\mathbf{r}) = e^{\imath\mathbf{kr}}\chi_s \quad , \quad E = \frac{\hbar k^2}{2m}, \tag{2.4}$$

where χ_s is the spinpart with two eigenvalues for spin up and spin down. We can assume some volume V with periodic boundary conditions and obtain a k mesh with density of states of $V/(2\pi)^3$. At each $\mathbf{k}$ point a state with energy $\epsilon_{\mathbf{k}}$ can be occupied by two electrons with different spin and the occupation is given by Fermi-Dirac distribution

$$f(\epsilon, T) = \frac{1}{e^{\frac{\epsilon-\mu(T)}{k_B T}} + 1}. \tag{2.5}$$

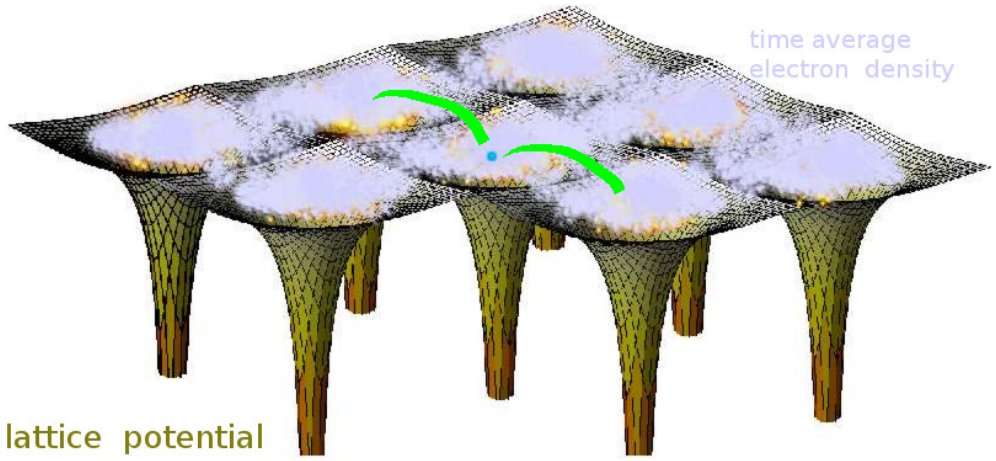

Figure 2.1: Representation of the solid as a kind of electron gas subjected to the periodic potential of ions. Solutions of this problem are given in terms of Bloch wave functions and energy bands.

At the limit $T \to 0K$ one obtains the step function $\Theta(\epsilon_F - \epsilon)$, where $\mu(0) = \epsilon_F$ is the Fermi energy. All the states in the interval $0 \leq \epsilon \leq \epsilon_F$ are occupied and for $\epsilon > \epsilon_F$ are unoccupied. Here one can calculate the density of states, i.e., electronic states per spin direction in an energy interval $[\epsilon, \epsilon + \delta\epsilon]$

$$N(\epsilon) = \int n(\epsilon') f(\epsilon', T) d\epsilon'. \tag{2.6}$$

In the case of the non-interacting fermionic system of electrons (free electron approximation for valence electrons) in the ground state all of the electronic states up to the Fermi energy $\epsilon = \epsilon_F$ are occupied and therefore ϵ_F is called the band width. In this approximation the important electron-electron interaction is neglected and the effects of the ionic lattice are underestimated, therefore the validity for the band structure calculations is constricted. If one switch on the periodic lattice potential in a perturbative way, i.e., if we assume that the periodic lattice potential is weak, then at the edges of the Brillouin zone(unit cell in **k**-space), where the Bragg reflexions occur band degeneracies are lifted. Therefore bands are separated by energy ranges in which there are no states i.e. energy gaps emerge. The next improvement is done within the Hartree Fock Theory, where an electron feels an effective electrostatic potential generated by a distribution of charges, which takes into account the effect of other electrons. This charge is the total charge of the system minus an exchange charge. This exchange charge is generated due to the Pauli principal.

In this approximation the electron-electron interaction is taken into account in a mean

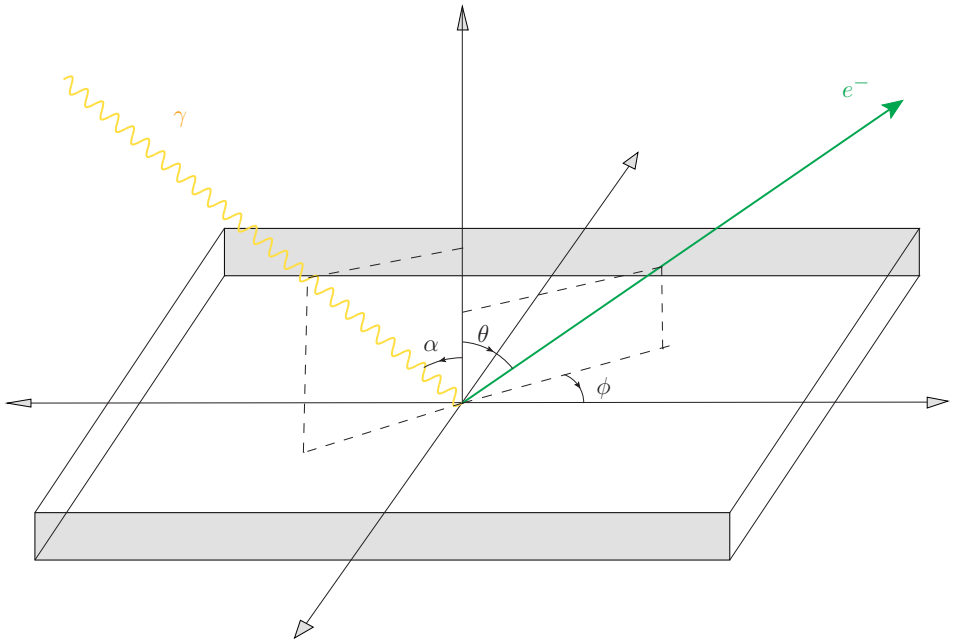

Figure 2.2: Geometrical representation of the angle-resolved photo emission spectroscopy experiment. Monochromatical light is subjected onto a sample and the energy and angle of the outcoming photoelectrons are measured.

field manner and one would still end up in an one particle Schrödinger equation which has to be solved. This approximation is very powerful for atomic physics and molecular physics but still many body effects are not included. The inclusion of the many body effects happen in the density functional theory within the local density approximation and its extensions. Although density functional theory delivers good results for band structure calculations for many compounds it fails dramatically, for the correlated electronic systems, because correlation effects can not be dealt within the one particle picture.

For a better physical understanding of the meaning of electronic band structure we want to show here one of the most reliable methods concerning the empirical measurement of the band structure. Over the years many reliable methods concerning the determination of the electronic structure have been developed. Angle resolved photoemission spectroscopy (ARPES) and bremsstrahlung isochromat spectroscopy (ARBIS) are among the class of most accurate methods.

In a typical photo emission spectroscopy experiment monochromatic light is directed on a sample and the photons with the adequate energy are absorbed by the electrons. From the kinetic energy of the emitted electrons the binding energy can be calculated. Using this and the angle of the emission also the momentum of the electrons can be extracted. Geometrical representation of the angle-resolved photo emission spectroscopy experiment (ARPES) is shown in figure 2.2. The kinetic energy of the emitted electrons

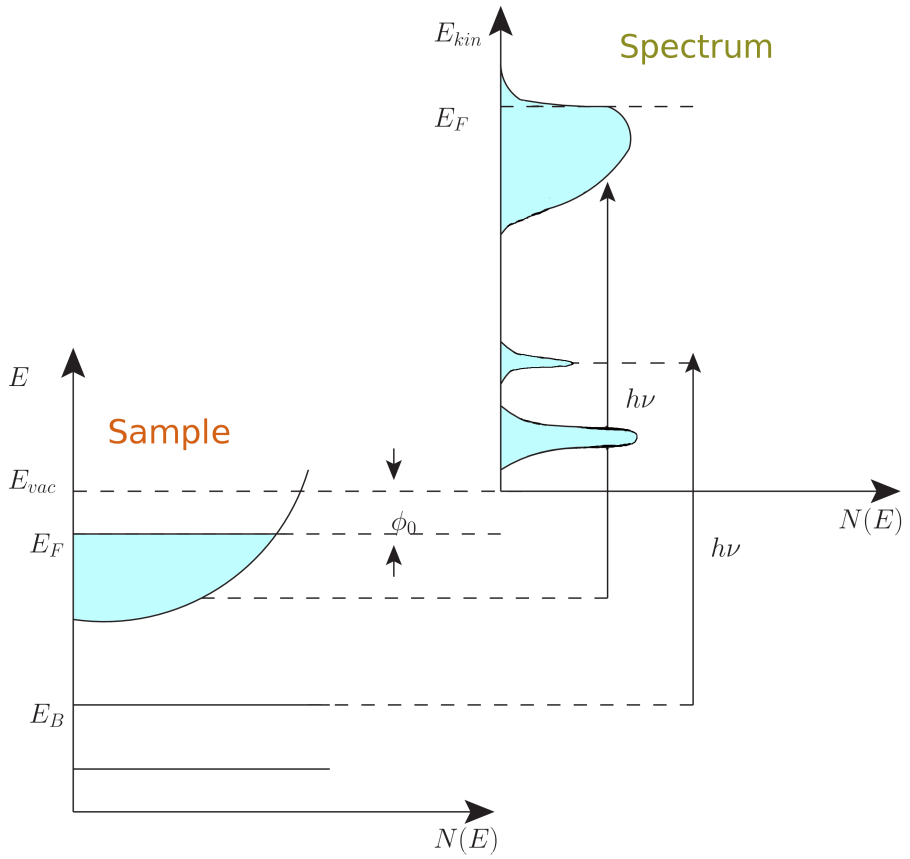

Figure 2.3: Energy diagram of photoemession spectroscopy in one-particle approximation picture .

is given by

$$E_{kin} = h\nu - E_B - \phi_0, \tag{2.7}$$

where the term ϕ_0 denotes the work function. The quantities E_{kin}, ϕ and θ can be measured and from this one can obtain the momentum by using the following relations

$$\begin{aligned} |\mathbf{K}| &= \frac{1}{\hbar}\sqrt{(2mE_{kin})}, \\ K_x &= |\mathbf{K}|\sin(\theta)\cos(\phi), \\ K_y &= |\mathbf{K}|\sin(\theta)\sin(\phi), \\ K_z &= |\mathbf{K}|\cos(\theta). \end{aligned}$$

Using the conservation laws $E_{kin} = h\nu - E_B - \phi_0$ and $\mathbf{K} = \mathbf{k} + (\mathbf{k}_\gamma)$ one can obtain the binding energy E_B and momentum $\mathbf{k}$ of the solid and the energy spectrum is demonstrated in figure 2.3. From this the obtained ARPES signal $I(\mathbf{k}, \epsilon)$ is direct proportional

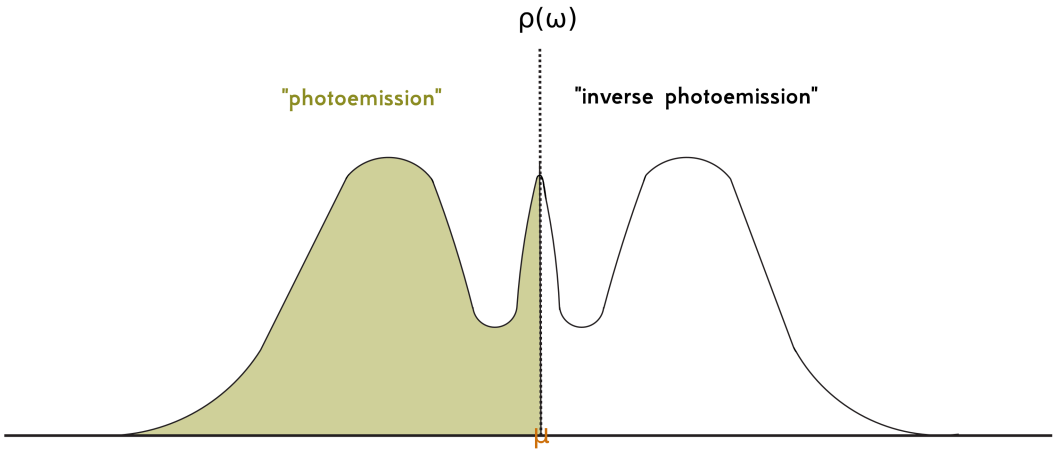

Figure 2.4: Photoemession spectroscopy and inverse spectroscopy in many body framework . A sketch of momentum integrated spectral function $\rho(\omega)$.

to the removal part of the spectral function which is the imaginary part of the Green's function

$$A(\mathbf{k},\omega) = -\frac{1}{\pi}\mathrm{Im}G(\mathbf{k},\omega). \tag{2.8}$$

In this context we can say that the spectral function gives the probability of removing or adding an electron at energy ω and momentum $\mathbf{k}$ from the N-electron system which is sketched in figure 2.4.

As mentioned photo emission spectroscopy and inverse photo emission spectroscopy are related to the one-particle Green's function. Therefore we will next consider the definition and properties of the one-particle Green's function.

2.3 Green's Functions

Green's functions, also correlation functions deliver important quantities which are essential for the description of the dynamical properties of the many body systems. For better understanding of the physics behind these objects let us start very elementary and consider them as a method for dealing with differential equations. Therefore we start with the definition of a general differential equation of the form

$$Lf(\mathbf{x}) = g(\mathbf{x}), \tag{2.9}$$

where L is a linear differential operator and $g(\mathbf{x})$ and $f(\mathbf{x})$ are C^n functions. An arbitrary inhomogeneity of a differential equation can be represented by delta function

$$g(\mathbf{x}) = \int \delta(\mathbf{x}-\mathbf{x}')g(\mathbf{x}')d\mathbf{x}'. \tag{2.10}$$

Now we can study another related equation of the form

$$LG(\mathbf{x}, \mathbf{x}') = \delta(\mathbf{x} - \mathbf{x}'), \tag{2.11}$$

where the differential operator L acts only on the argument $\mathbf{x}$ and $G(\mathbf{x}, \mathbf{x}')$ is the Green's function of the differential equation. Once the Green's function is known, the general form of the solution for the differential equation can be written down as

$$f(\mathbf{x}) = \int G(\mathbf{x}, \mathbf{x}')g(\mathbf{x}')d\mathbf{x}'. \tag{2.12}$$

Here we can verify the correctness of this result easily

$$Lf(\mathbf{x}) = \int LG(\mathbf{x}, \mathbf{x}')g(\mathbf{x}')d\mathbf{x}' = \int \delta(\mathbf{x} - \mathbf{x}')g(\mathbf{x}')d\mathbf{x}' = g(\mathbf{x}). \tag{2.13}$$

The solution becomes unique once the boundary conditions are specified. This method represented here can be generalized for the solution of the many body Schrödinger equation. Let us first apply this method on the single particle Schrödinger equation

$$\left[i\partial_t - H_0(\mathbf{r}) - V(\mathbf{r})\right] \psi(\mathbf{r}, t) = 0, \tag{2.14}$$

and treat $V(\mathbf{r})$ as a perturbation. In the similar way above we define here the corresponding Green's functions

$$\left[i\partial_t - H_0(\mathbf{r})\right] G_0(\mathbf{r}, t; \mathbf{r}', t') = \delta(\mathbf{r} - \mathbf{r}')\delta(t - t') \tag{2.15}$$

$$\left[i\partial_t - H_0(\mathbf{r}) - V(\mathbf{r})\right] G(\mathbf{r}, t; \mathbf{r}', t') = \delta(\mathbf{r} - \mathbf{r}')\delta(t - t'). \tag{2.16}$$

Now we can write the solution of the time-dependent Schrödinger equation

$$\psi(\mathbf{r}, t) = \psi_0(\mathbf{r}, t) + \int d\mathbf{r}' \int dt' G_0(\mathbf{r}, t; \mathbf{r}, t')V(\mathbf{r}')\psi(\mathbf{r}', t'). \tag{2.17}$$

Green's function is often called propagator because if the wave function is known at some time then the wave function at a later time is obtained by

$$\psi(\mathbf{r}, t) = \int d\mathbf{r}' \int dt' G(\mathbf{r}, t; \mathbf{r}', t')\psi(\mathbf{r}', t'). \tag{2.18}$$

Another more obvious way to see this is by following expression

$$G(\mathbf{r}, t; \mathbf{r}', t') = -i\Theta(t - t')\langle \mathbf{r}|e^{-iH(t-t')}|\mathbf{r}'\rangle, \tag{2.19}$$

which is also a solution of the partial differential equation defining the Green's function and gives the transition amplitude for the propagation of a state as demonstrated in the figure 2.5. In order to find a closed expression for the Green's function we start with the response of the system on a time dependent perturbation.

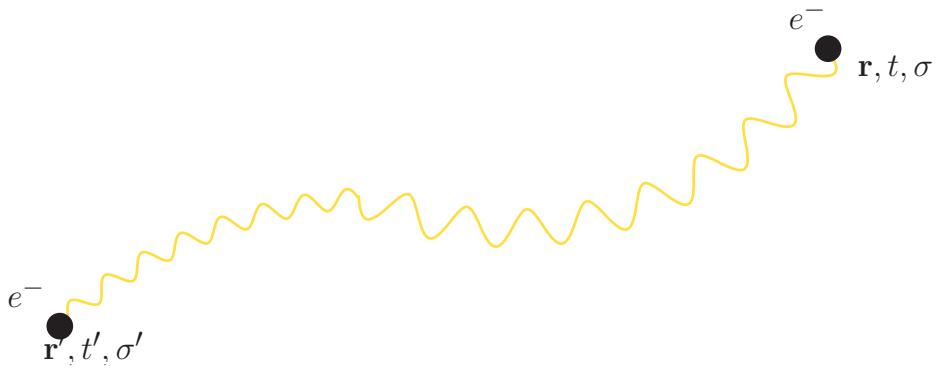

Figure 2.5: Demonstration of the explanation of the Green's function as the probability that an electron at the time and position $(\mathbf{r}', t')$ propagates to the position and at the time $(\mathbf{r}, t)$.

2.3.1 Linear response theory

Linear response theory is a very widely used concept in physics. It states that the response to a weak perturbation of a system is proportional to the perturbation itself. Let us assume that a physical system is described by a time independent Hamiltonian H_0 at equilibrium. For such a system a general observable can be calculated using the following relation

$$\langle A \rangle = \frac{1}{Z_0} \sum_n \langle n|A|n\rangle exp(-\beta E_n) \quad , \quad Z_0 = \sum_n exp(-\beta E_n). \tag{2.20}$$

Here we can apply a time dependent perturbation on this system at the time t_0 and this leads to a time-dependent Hamiltonian

$$H(t) = H_0 + V(t)\Theta(t - t_0). \tag{2.21}$$

At this point the time-dependent expectation value of an observable is defined the following relation

$$\langle A \rangle_t = \frac{1}{Z_0} \sum_n \langle n(t)|A|n(t)\rangle exp(-\beta E_n) \quad , \quad Z_0 = \sum_n exp(-\beta E_n). \tag{2.22}$$

The basis states $|n(t)\rangle$ have to satisfy the time-dependent Schrödinger equation

$$i\hbar \frac{\partial n(t)}{\partial t} = H(t)|n(t)\rangle. \tag{2.23}$$

The interaction picture representation for the basis states $|n(t)\rangle$ is given by

$$|n(t)\rangle = e^{-\frac{i}{\hbar} H_0 t} U(t, t_0)|n\rangle, \tag{2.24}$$

where the unitary operator $U(t,t_0)$ is used for the time evolution of a state from time t_0 to the time t. This unitary operator is defined by the following differential equation

$$\frac{\partial}{\partial t}U(t,t_0) = -\frac{i}{\hbar}V(t)U(t,t_0), \tag{2.25}$$

which is obtained from the condition that the time derivative of the equation (2.24)

$$\frac{\partial}{\partial t}|n(t)\rangle = -\frac{i}{\hbar}H_0|n(t)\rangle + e^{-\frac{i}{\hbar}Ht}\frac{\partial}{\partial t}U(t,t_0)|n\rangle \tag{2.26}$$

has to satisfy the Schrödinger equation. The differential equation in (2.25) can be solved iteratively and using the time ordering operator $\mathcal{T}$, we obtain the following compact form for the unitary operator(Appendix A)

$$U(t,t_0) = \mathcal{T}\left(e^{-\frac{i}{\hbar}\int_{t_0}^{t}dt'V(t')}\right). \tag{2.27}$$

This operator in the linear approximation is given by

$$U(t,t_0) \approx \mathbb{1} - \frac{i}{\hbar}\int_{t_0}^{t}V(t')dt'. \tag{2.28}$$

Now we can insert this into equation (2.22) and obtain the following form for the expectation value in linear response

$$\begin{aligned}\langle A\rangle_t &= \langle A\rangle_0 - i\int_{t_0}^{t}dt'\frac{1}{Z_0}\sum_n e^{-\beta E_n}\langle n(t_0)|A(t)V(t') - V(t')A(t)|n(t_0)\rangle \\ &= \langle A\rangle_0 - i\int_{t_0}^{t}dt'\langle\big[A(t),V(t')\big]\rangle_0.\end{aligned} \tag{2.29}$$

One can rewrite this equation as

$$\begin{aligned}\langle\Delta A\rangle_t &= \langle A\rangle_t - \langle A\rangle_0 \\ &= \int_{t_0}^{\infty}C_{AV}(t,t')e^{-\eta(t-t')}dt',\end{aligned} \tag{2.30}$$

where the expression in the brackets is called retarded correlation function or response function or Green's function

$$C^R_{AV}(t,t') = -i\Theta(t-t')\langle\big[A(t),V(t')\big]\rangle_0 \tag{2.31}$$

of two operators. This Green's function is called retarded because of it's causality i.e. the perturbation at the time t' is prior to the response at the time t. The step function $\Theta(t-t')$ is here to ensure that the condition $t > t'$ is fulfilled. The exponential factor $exp(-\eta(t-t'))$ is used for the decay of the response at the time t and in the end one has to carry the limit $\eta \to 0^+$.

2.3.2 Green's functions for many body systems

The concrete expression for the retarded Green's function derived in the case of the linear response theory can be transferred to the many body systems by replacing the general operators ($A(t)$, $B(t')$) with the field operators ($\psi_\sigma(\mathbf{r},t)$, $\psi^\dagger_{\sigma'}(\mathbf{r}',t')$). As mentioned the Green's function gives the transition amplitude for a particle on a position $\mathbf{r}'$ at time t' to a position $\mathbf{r}$ at time t. The retarded single-particle Green's function is defined by following expression

$$G^{ret}(\mathbf{r},\sigma,t;\mathbf{r}',\sigma',t') = i\Theta(t-t')\langle\Big[\psi_\sigma(\mathbf{r},t),\psi^\dagger_{\sigma'}(\mathbf{r}',t')\Big]\rangle, \tag{2.32}$$

where ψ's here correspond to the field operators and they can be translated to the conventional operators by a basis change

$$G^{ret}(\nu,\sigma,t;\nu',\sigma',t') = i\Theta(t-t')\langle\Big[a_{\nu\sigma}(t),a^\dagger_{\nu'\sigma'}(t')\Big]\rangle. \tag{2.33}$$

These single particle Green's functions are important because they describe the propagation of single particles governed by the many body Hamiltonian. For translational invariant systems where the Green's function depend only on the difference $\mathbf{r}-\mathbf{r}'$ one can perform a Fourier transformation and obtain the retarded Green's function in the $\mathbf{k}$-space

$$G^{ret}(\mathbf{r}-\mathbf{r}',\sigma t,\sigma' t') = \frac{1}{V}\sum_{\mathbf{k}} e^{i\mathbf{k}(\mathbf{r}-\mathbf{r}')}G^R(\mathbf{k},\sigma t,\sigma' t'), \tag{2.34}$$

$$G^{ret}(\mathbf{k},\sigma t,\sigma' t') = -i\Theta(t-t')\langle\Big[a_{\mathbf{k}\sigma}(t),a^\dagger_{\mathbf{k}\sigma'}(t')\Big]\rangle. \tag{2.35}$$

For the sake of completeness we can give here the definition of another type of Green's function where the time ordering operator $\mathcal{T}$ is used. This Green's function is called the causal Green's function

$$G(\mathbf{k},\sigma t,\sigma' t') = -i\langle\mathcal{T}a_{\mathbf{k}\sigma}(t)a^\dagger_{\mathbf{k}\sigma'}(t')\rangle, \tag{2.36}$$

where the time ordering operator $\mathcal{T}$ is defined as

$$\mathcal{T}\left(a_{\nu\sigma}(t)a^\dagger_{\nu'\sigma'}(t')\right) = \Theta(t-t')a_{\nu\sigma}(t)a^\dagger_{\nu'\sigma'}(t) - \Theta(t'-t)a^\dagger_{\nu'\sigma'}(t')a_{\nu\sigma}(t). \tag{2.37}$$

In order to learn more about the definition and extraction of physical information from the Green's function we are going to introduce some important concepts in the next subsections.

2.3.3 Lehman representation

Lehman representation is the expression of the retarded Green's function in the eigenbasis of the Hamiltonian. Let us skip here the spin indices for clarify. Here it is useful

to define the so-called greater and lesser Green's functions

$$G^{>}(\mathbf{k}, t-t') = -i\langle a_{\mathbf{k}}(t) a_{\mathbf{k}}^{\dagger}(t')\rangle, \tag{2.38}$$

$$G^{<}(\mathbf{k}, t-t') = i\langle a_{\mathbf{k}}^{\dagger}(t) a_{\mathbf{k}}(t')\rangle, \tag{2.39}$$

$$G^{ret}(\mathbf{k}, t-t') = \Theta(t-t')\left[G^{>} - G^{<}\right], \tag{2.40}$$

where $G^{>}$ gives the propagation of electrons and $G^{<}$ the propagation of holes, which would correspond the photon emission and inverse photon spectroscopy as demonstrated in the figure 2.4. We insert the completeness relation

$$\mathbb{1} = \sum_{m} |m\rangle\langle m|, \tag{2.41}$$

and the corresponding time evolution of these operators and get the following result for the greater Green's function

$$\begin{aligned} G^{>}(\mathbf{k}, t-t') &= -i\langle a_{\mathbf{k}}(t) a_{\mathbf{k}}^{\dagger}(t')\rangle \\ &= -i\frac{1}{Z}\sum_{m,n} e^{\beta E_n}\langle n|a_{\mathbf{k}}(t)|m\rangle\langle m|a_{\mathbf{k}}^{\dagger}(t')|n\rangle \\ &= -i\frac{1}{Z}\sum_{m,n} e^{\beta E_n} e^{iE_n t} e^{-iE_m t} e^{iE_m t'} e^{-iE_n t'}\langle n|a_{\mathbf{k}}|m\rangle\langle m|a_{\mathbf{k}}^{\dagger}|n\rangle \\ &= -i\frac{1}{Z}\sum_{m,n} e^{\beta E_n}|\langle n|a_{\mathbf{k}}|m\rangle|^2 e^{i(E_n - E_m)(t-t')}. \end{aligned} \tag{2.42}$$

The equivalent derivation can be done for the lesser Green's function. Consequently we can write an analytic expression for the retarded Green's function

$$\begin{aligned} G^{ret}(k, t-t') &= -i\Theta(t-t')\frac{1}{Z}\sum_{m,n} e^{\beta E_n} \\ &\times \left[|\langle n|a_{\mathbf{k}}|m\rangle|^2 e^{i(E_n - E_m)(t-t')} + |\langle n|a_{\mathbf{k}}^{\dagger}|m\rangle|^2 e^{i(E_n - E_m)(t-t')}\right]. \end{aligned} \tag{2.43}$$

Because the Propagator evolves periodically in time i.e. it depends on $t - t'$ we can transform from time domain t to the frequency domain ω

$$G^{ret}(\mathbf{k}, \omega) = \frac{1}{Z}\sum_{m,n} e^{-\beta E_n}\left(\frac{|\langle n|a_{\mathbf{k}}|m\rangle|^2}{\omega + (E_n - E_m) + i\eta} + \frac{|\langle n|a_{\mathbf{k}}^{\dagger}|m\rangle|^2}{\omega - (E_n - E_m) + i\eta}\right). \tag{2.44}$$

From this expression it is obvious that the evaluation of the Green's function needs the eigenvalues and eigenstates of the system of interest.

2.3.4 Green's function on the Matsubara axis

Another Green's function can be obtained by replacing the time or frequency argument by so-called imaginary time or imaginary frequency which are referred as Matsubara

Green's function. This is a mathematical tool but it delivers the opportunity to many simplifications, e.g., calculation of the Green's function in terms of Feynman diagrams in diagrammatic perturbation theory.

Matsubara Green's function in real space or in ν-representation is defined in a similar way like the retarded Green's function

$$G^M(\mathbf{r},\sigma,\tau;\mathbf{r}',\sigma',\tau') = \langle \mathcal{T}_\tau \psi_\sigma(\mathbf{r},\tau)\psi^\dagger_{\sigma'}(\mathbf{r}',\tau')\rangle, \tag{2.45}$$

$$G^M(\nu,\sigma,\tau;\nu',\sigma',\tau') = \langle \mathcal{T}_\tau a_{\nu\sigma}(\tau)a^\dagger_{\nu'\sigma'}(\tau')\rangle, \tag{2.46}$$

but the real time is substituted by an imaginary time $i\tau$

$$t \longrightarrow i\tau, \tag{2.47}$$

where τ is a real number and $\mathcal{T}_\tau$ is the time ordering operator in imaginary time

$$\mathcal{T}_\tau(a_{\nu\sigma}(\tau)a^\dagger_{\nu'\sigma'}(\tau')) = \Theta(\tau-\tau')a_{\nu\sigma}(\tau)a^\dagger_{\nu'\sigma'}(\tau') - \Theta(\tau'-\tau)a^\dagger_{\nu'\sigma'}(\tau')a_{\nu\sigma}(\tau). \tag{2.48}$$

Let us note some properties of the Matsubara Green's function for a better understanding of the internal structure.

1. The Matsubara Green's function depends only of the time difference i.e. for the case $\tau > \tau'$ this can be verified

$$\begin{aligned} G^>_{\nu\nu'}(\tau,\tau') &= \langle a_\nu(\tau)a^\dagger_{\nu'}(\tau')\rangle \\ &= -\frac{1}{Z}Tr\left[e^{-\beta H}e^{\tau H}a_\nu e^{-\tau H}e^{\tau' H}a^\dagger_{\nu'}e^{-\tau' H}\right] \\ &= -\frac{1}{Z}Tr\left[e^{-\beta H}e^{\tau H}e^{-\tau' H}a_\nu e^{-\tau H}e^{\tau' H}a^\dagger_{\nu'}\right] \\ &= -\frac{1}{Z}Tr\left[e^{-\beta H}e^{(\tau-\tau')H}a_\nu e^{-(\tau-\tau')H}a^\dagger_{\nu'}\right] \\ &= G^>_{\nu\nu'}(\tau-\tau'), \end{aligned} \tag{2.49}$$

   where for clearness we skipped the spin index. The same calculation can also be done for the other case $\tau < \tau'$.

2. The convergence of the $G^>(\nu,\tau;\nu',\tau')$ is only guaranteed in the interval $-\beta < \tau-\tau' < \beta$, which can be verified by using the Lehman representation.

3. Fermionic Matsubara Green's function is anti-periodic in β i.e. $G^>_{\nu\nu'}(t+\beta) = -G^>_{\nu\nu'}(t+\beta)$ and the proof of this for the case $\tau < 0$ is given by:

$$\begin{aligned} G^>_{\nu\nu'}(\tau+\beta) = &= -\frac{1}{Z}Tr\left[e^{-\beta H}e^{(\tau+\beta)H}a_\nu e^{-(\tau+\beta)H}a^\dagger_{\nu'}\right] \\ &= -\frac{1}{Z}Tr\left[e^{\tau H}a_\nu e^{-\tau H}e^{-\beta H}a^\dagger_{\nu'}\right] \\ &= -\frac{1}{Z}Tr\left[a_\nu(\tau)e^{-\beta H}a^\dagger_{\nu'}\right] \\ &= -\frac{1}{Z}Tr\left[e^{-\beta H}\mathcal{T}_\tau(a_\nu(\tau)a^\dagger_{\nu'})\right] \\ &= G^>_{\nu\nu'}(\tau). \end{aligned} \tag{2.50}$$

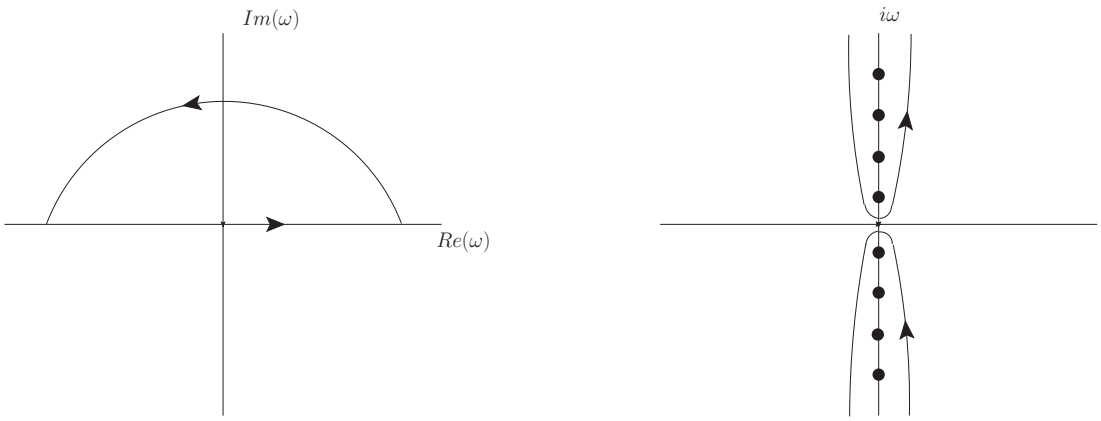

Figure 2.6: Green's function analyticity: retarded Green's function, right:Matsubara Green's function. The poles of the Matsubara Green's function are on the imaginary axis while the poles of the retarded Green's function are on the real axis

These properties can be used to calculate the Fourier transformation of the Matsubara Green's function in the interval $[-\beta, \beta]$

$$G_{\nu\nu'}(i\omega_n) = \int_0^\beta e^{i\omega_n(\tau-\tau')} G_{\nu\nu'}(\tau - \tau')d\tau. \tag{2.51}$$

The variable ω_n is the so-called Matsubara frequency and it can take the values $\omega_n = (2n+1)\pi/\beta$ for fermions, where n is an integer number. In analogous manner the Lehman representation for the Matsubara Green's function can also be derived which looks like the standard retarded Green's function but the frequency ω is replaced by the complex valued frequency $i\omega$

$$G^M(\mathbf{k}, i\omega_n) = \frac{1}{Z}\sum_{m,n} e^{-\beta E_n}\left(\frac{|\langle n|a_\mathbf{k}|m\rangle|^2}{i\omega_n + (E_n - E_m)} + \frac{|\langle n|a_\mathbf{k}^\dagger|m\rangle|^2}{i\omega_n - (E_n - E_m)}\right). \tag{2.52}$$

One essential point missing here concerns the analytical continuation which means if one has the Matsubara or retarded Green's function the other is obtained by analytical continuation. For clearness we can consider the analyticity of the retarded and Matsubara Green's function which is demonstrated in the following sketch in figure 2.6. If we have an analytic form of the Matsubara Green's function, the retarded Green's function can be calculated at the upper half plane by the following expression

$$G^{ret}(\omega) = G^M(i\omega \to \omega + i\theta). \tag{2.53}$$

For the general case it is not so obvious how to perform this transformation.

2.3.5 Spectral function

We have considered up to this point many kinds of Green's function with their particular properties. The next step is the extraction of important quantities out of the Green's function. One of these relevant quantities is the spectral function, which includes all information for the description of the energies of the single particle excitations implicitly. Consequently it can be used for the calculation of quantities like the quasi-particle dispersion relation or the total density of states. The energy of a peak in this function corresponds to the excitation energy at which an extra electron or hole can propagate.

The spectral function is proportional to the imaginary part of the single particle Green's function and is given at the energy ω and momentum $\mathbf{k}$ by the following expression

$$A(\mathbf{k},\omega) = -\frac{1}{\pi}\mathrm{Im}G(\mathbf{k},\omega). \tag{2.54}$$

Let us derive the spectral function for a non-interacting systems of fermions, which is given by the following Hamiltonian

$$H_0 = \sum_{\mathbf{k}\sigma} c^{\dagger}_{\mathbf{k}\sigma} c_{\mathbf{k}\sigma}. \tag{2.55}$$

Because the Hamiltonian is diagonal in momentum $\mathbf{k}$ and spin σ, we obtain the following expressions for the lesser, greater and retarded Green's function

$$\begin{aligned}
G_0^{>}(k,t-t') &= -i(1-n_F(\epsilon_k))e^{-i\epsilon_k(t-t')}, && (2.56)\\
G_0^{<}(k,t-t') &= in_F(\epsilon_k)e^{-i\epsilon_k(t-t')}, && (2.57)\\
G_0^{ret}(k,t-t') &= -i\theta(t-t')e^{-i\epsilon_k(t-t')}, && (2.58)
\end{aligned}$$

and if we transform this retarded Green's function for non-interacting fermions into the frequency domain ω we get

$$\begin{aligned}
G_0(\mathbf{k},\omega) &= -i\int_{-\infty}^{\infty} dt\theta(t-t')e^{-i\epsilon_k(t-t')\eta(t-t')}\\
&= \frac{1}{\omega-\epsilon_{\mathbf{k}}+i\eta}. && (2.59)
\end{aligned}$$

By exploiting the following relation

$$lim_{\eta\to 0^+}\frac{1}{x+i\eta} = P\frac{1}{x} - i\pi\delta(x), \tag{2.60}$$

we can easily calculate the spectral function for non-interacting fermions

$$A_0(\mathbf{k},\omega) = \delta(\omega-\epsilon_{\mathbf{k}}), \tag{2.61}$$

which has the form of a delta function with excitations at $\omega = \epsilon_{\mathbf{k}}$. This result does not hold for the interacting fermions because, e.g., in the solid the electron-phonon or electron-electron interactions lead to the broadening of this delta peaked structure.

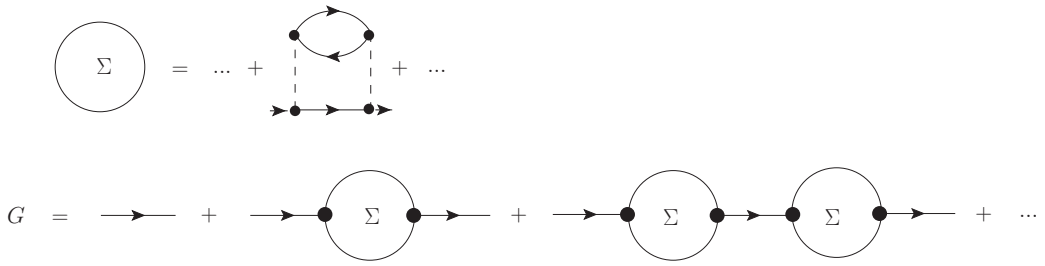

Figure 2.7: Green's function calculated by a diagrammatic expansion with the self-energy insertion.

2.3.6 Self-energy

The self-energy is another relevant quantity which can be extracted from the Green's function or which can be used to obtain it. As mentioned in a many body system the self-energy gives the difference between an interacting and a non-interacting system. In other words all the contributions due to the interactions are contained in this term. Summing all kind of interactions in all orders as shown in the figure 2.7 gives us the following closed form for the Green's function

$$\begin{aligned} G(\mathbf{k},\omega) &= G_0 + G_0\Sigma G_0 + G_0\Sigma G_0\Sigma G_0 + ... \\ &= \frac{1}{G_0^{-1} - \Sigma}, \end{aligned}$$

which is referred to as the Dyson equation. Here we can insert the exact expression for the free Green's function (2.59)

$$G(\mathbf{k},\omega) = \frac{1}{\omega - \epsilon_{\mathbf{k}} - \Sigma(\mathbf{k},\omega)}. \tag{2.62}$$

Self-energy in general is a complex term, so we can split it in a real and imaginary part

$$G(\mathbf{k},\omega) = \frac{1}{\omega - \epsilon_{\mathbf{k}} - \mathrm{Re}\Sigma(\mathbf{k},\omega) - i\mathrm{Im}\Sigma(\mathbf{k},\omega)}. \tag{2.63}$$

At small energies ω and for the $\mathbf{k}$ vectors close to the Fermi vector k_F the inverse Green's function can be expanded in powers of $\mathbf{k} - k_F$ and ω

$$\begin{aligned} G^{-1}(\mathbf{k},\omega) &\approx \left(\omega - \omega\frac{\partial}{\partial\omega}\mathrm{Re}\Sigma - (\mathbf{k}-k_F)\frac{\partial}{\partial\omega}(\epsilon + \mathrm{Re}\Sigma) - i\mathrm{Im}\Sigma\right) \\ &= (1 - \frac{\partial}{\partial\omega}\mathrm{Re}\Sigma)\left(\omega - (\mathbf{k}-k_F)\frac{\partial}{\partial\omega}(\epsilon+\mathrm{Re}\Sigma)\frac{1}{(1-\frac{\partial}{\partial\omega}\mathrm{Re}\Sigma)} - i\mathrm{Im}\Sigma\frac{1}{(1-\frac{\partial}{\partial\omega}\mathrm{Re}\Sigma)}\right) \\ &= Z^{-1}\left(\omega - (\mathbf{k}-k_F)\frac{\partial}{\partial\omega}(\epsilon+\mathrm{Re}\Sigma)Z - i\mathrm{Im}\Sigma Z\right) \\ &= Z^{-1}\left(\omega - \tilde{\epsilon}_{\mathbf{k}} + \frac{i}{2\tau_{\mathbf{k}}(\omega)}\right), \end{aligned} \tag{2.64}$$

where the variables Z (quasi-particle renormalization), $\tilde{\epsilon}_{\mathbf{k}}$ (effective energy) and $\tau_{\mathbf{k}}$ (average quasi-particle lifetime) are defined as

$$Z = (1 - \frac{\partial}{\partial\omega}\mathrm{Re}\Sigma)|_{\omega=0}, \tag{2.65}$$

$$\tilde{\epsilon}_{\mathbf{k}} = (\mathbf{k}-k_F)\frac{\partial}{\partial\omega}(\epsilon+\mathrm{Re}\Sigma)Z|_{k=k_F}, \tag{2.66}$$

$$\frac{1}{\tau_{\mathbf{k}}} = -2Z\mathrm{Im}\Sigma(\mathbf{k},\omega). \tag{2.67}$$

Through the consideration of this quasi-particle regime we have seen that the real part of the self energy is connected to the change of the energy dispersion relation and imaginary part of self energy is connected to the average lifetime of the quasi particles. One can use this result to calculate the complete spectral function by supplementing it with the incoherent part which comes from many particle excitations

$$\begin{aligned} A(\mathbf{k},\omega) &= -\frac{1}{\pi}\mathrm{Im}G(\mathbf{k},\omega) \\ &= Z\delta(\omega - \tilde{\epsilon}_{\mathbf{k}}) + A^{incoh}(\mathbf{k},\omega), \end{aligned} \tag{2.68}$$

where the first part comes from Fermi liquid theory, and the second one are the incoherent excitations.

2.4 Local and non-local correlations

The previous section clarifies the effect of the interactions in the many body systems. There they change the quasi-particle peak size and induce incoherent peaks. These incoherent peaks are a correlation effect, therefore one has to go beyond the one-particle picture.

The Green's function method gives a systematic may for the description of correlations. It can be obtained by diagrammatic methods where one has to sum up infinite diagrams representing different kind of interactions which is shown in figure 2.7. The bubble is referred as self-energy Σ which is giving the difference between an interacting and

non-interacting Green's function. The summation of all of the diagrams give the Dyson equation

$$G(\mathbf{k},\omega) = \frac{1}{G_0^{-1}(\mathbf{k},\omega) - \Sigma(\mathbf{k},\omega)}, \tag{2.69}$$

where the self energy is in general not known and many approximative solutions are possible. One can assume that the non-local correlations are negligible small and that they can be set to zero and self-energy becomes momentum independent $\Sigma(\omega)$. Such approximations are very useful in many applications, but in cases where non-local correlations are important to describe some physical effects they fail to give accurate results. Within some extensions short range or long range correlations can be included, which will be explained in more details in the next chapter.

3 METHODS

3.1 Introduction

In the last chapter we have shown that the correlations are described by correlation functions or Green's functions, which are in general not known. In the last decades some powerful methods have been emerged in order to calculate the Green's function in good approximations. Let us give a rough overview of these methods with the aspect of the correlation level taken into account.

In the standard mean field theory the lattice problem is replaced by a single site effective problem with less degrees of freedom. The dynamics of this site is maintained by the interaction of the local degrees of freedom at this site with an external bath or mean field formed by all other degrees of freedom on the other lattice sites. In contrary, in DMFT the external bath or mean field is not a number but a function of energy ω. In this approach the fluctuations among the four different atomic lattice site configurations are included. There are two essential steps leading to the development of the dynamical mean field theory for the many body systems[31].

1. In the limit of infinite coordination (neighbors) the self-energy for the interacting fermionic models becomes local, i.e., momentum dependency cancels, so there is no momentum dependency any more. In other words spatial fluctuations die out because the neighbors of a lattice site behave or can be treated as an external bath[6].

2. The lattice model is mapped on a self-consistent quantum impurity model, i.e., one has to solve the impurity problem which is self-consistently coupled to a dynamical field[7].

In DMFT the self-energy of the lattice problem is determined by mapping the lattice problem to the single impurity periodic Anderson model, that means one has to solve the corresponding Hamiltonian

$$\begin{aligned} H_{AIM} &= H_{atom} + H_{bath} + H_{coupling} \\ &= H_{atom} + \sum_{i,\sigma} \epsilon_i^{bath} n_{i\sigma} + \sum_{i,\sigma} V_i \left(b_{i\sigma}^\dagger c_\sigma + c_\sigma^\dagger b_{i\sigma} \right), \end{aligned} \tag{3.1}$$

where the original problem is separated in three parts, in the first term only atomic degrees of freedom are taken into account. The second term is a reservoir of non interacting lattice sites or bath sites with the energy levels ϵ_i^{bath}, and the task of the last term is to combine the first two separated terms by the hybridization or hopping V_i between

the atomic energy levels and bath energy levels. One can combine these parameters in a generalized hybridization function

$$\Delta(\omega) = \sum_i \frac{|V_i|^2}{\omega - \epsilon_i^{bath}}, \tag{3.2}$$

which corresponds to the dynamical mean field. The electrons described by the bath sites are the same as the electrons of the impurity. The parameters ϵ_i^{bath} and V_i in the generalized hybridization function has to be elected in such a way that the Green's function of the Anderson impurity model coincides with the Green's function of the lattice model. Because of this fact the hybridization function is determined from the following self-consistency condition[31, 32]

$$G(\omega) = \sum_{\mathbf{k}} \frac{1}{\Delta(\omega) + G^{-1}(\omega) - \epsilon_{\mathbf{k}}}. \tag{3.3}$$

The only approximation in DMFT up to this point is that all of the non-local compounds of the self-energy are neglected, i.e., they are set to zero

$$\Sigma_{i,j} \simeq \Sigma_{imp} \quad , \quad \Sigma_{i \neq j} \simeq 0. \tag{3.4}$$

This means that DMFT in the atomic limit (i.e. separated atoms with local self-energy $\Sigma(\omega)$ and vanishing hybridization function $\Delta(\omega) = 0$) yields exact results. It becomes also exact in the non interacting limit $U = 0$, because the self-energy vanishes and only the free on-site Green's function is left. The third exact limit is the limit of the infinite coordination with vanishing spatial fluctuations which has been derived from diagrammatic considerations[6]. This approach takes into account local quantum fluctuations, i.e., temporal fluctuations between possible quantum states at a given lattice site, while spatial fluctuations are completely frozen or neglected.

For many applications these spatial non-local correlations are essential, e.g, for the Luttinger liquid physics of low dimensional correlated systems[33], d-wave pairing in the two dimensional cuprate high T_C superconductors[34], ARPES spectra of 3D ferromagnetic iron with momentum $\mathbf{k}$ dependent self-energy effects[35], variations of the quasi-particle residue, the quasi-particle lifetime and the effective mass, exotic orders with order parameters involving several sites such as staggered flux or dimerization[9], or short ranged spin correlations in the metallic state[10].

Because of all these reasons it is necessary to include the spatial non-local correlations, but there is no method which can keep them exactly. In many applications it is enough to take them into account up to short length scales because in many correlated compounds momentum dependence of the self-energy is assumed to be less important than the frequency dependence. This argumentation is based on the fact that physical properties are dominated by a weakly dispersive feature of the electronic spectra near the Fermi surface[10]. Here we can differentiate between methods where short ranged correlations are captured and long ranged correlations are neglected and on the other side methods where long ranged correlations in different channels are also captured. Among

the first class of methods are cluster extensions of DMFT like cluster or cellular DMFT (C-DMFT)[8, 9] or dynamical cluster approximation (DCA)[10]. C-DMFT is a generalization of the standard DMFT where the cluster degrees of freedom are treated exactly and the other degrees of freedom are considered as a reservoir of non interacting sites. The challenge here is to find a appropriate self-consistency condition without breaking symmetries or generating non-physical solutions which violets the causality condition. In this approach the unknown quantity self-energy is estimated by the cluster self-energy which depends on the cluster shape and can be chosen in such a way to minimize the finite size effects[8]. Another method which can also be related with DMFT within the self-energy functional approach is variational cluster approximation (VCA)[15, 13]. In this approach also short range correlations up to the size of the regarded clusters are taken into account.

Among the second class of methods, which capture simultaneously the local correlations of DMFT and the long range correlations beyond DMFT are Dynamical vertex approximation (DΓA)[14] and Dual Fermions approach[36]. These methods can reproduce DMFT results in the limit of vanishing non-local correlations and are based on diagrammatic expansions[14, 36].

After this rough overview of the methods dealing with correlations we want to consider the details of the VCA which is based on the exact diagonalization techniques and on the cluster perturbation theory. We start very elementary by the second quantized version of the many body Hamiltonian using the many body approach for solids following the book by Bruus and Flensberg[29]. Then we will argue how the Hubbard model is obtained from this general Hamiltonian in the second quantization. We will use Hubbard model for the derivation of the exact diagonalization techniques for the many body methods based on diagonalization algorithms (like standard Lanczos or band Lanczos). Because of the strong limitation of these techniques we will use cluster perturbation theory in order to calculate large systems. Cluster perturbation theory has many limitations due to the absence of a self-consistency condition or variational principle. This shortcoming can be overcomed within variational cluster approach. Then we will look very briefly to the DΓA, which is a powerful method for dealing with long-range correlations. In the last subsections we will introduce a method which combines density functional theory with VCA for the correlated compounds.

3.2 One- and two-particle operators in the second quantization and the Hubbard model

The many body Hamiltonian of the solids consists of one-particle and two-particle operators. Kinetic energy operator $-\frac{\hbar^2}{2m}\nabla^2_{\mathbf{r}_j}$ or external potential $v(\mathbf{r}_j)$ are one-particle operators, Coulomb interaction $V(\mathbf{r}_i-\mathbf{r}_j)=\frac{e^2}{4\pi\epsilon_0}\frac{1}{|\mathbf{r}_i-\mathbf{r}_j|}$ is a two-particle operator. These operators in second quantization are given by the following expressions

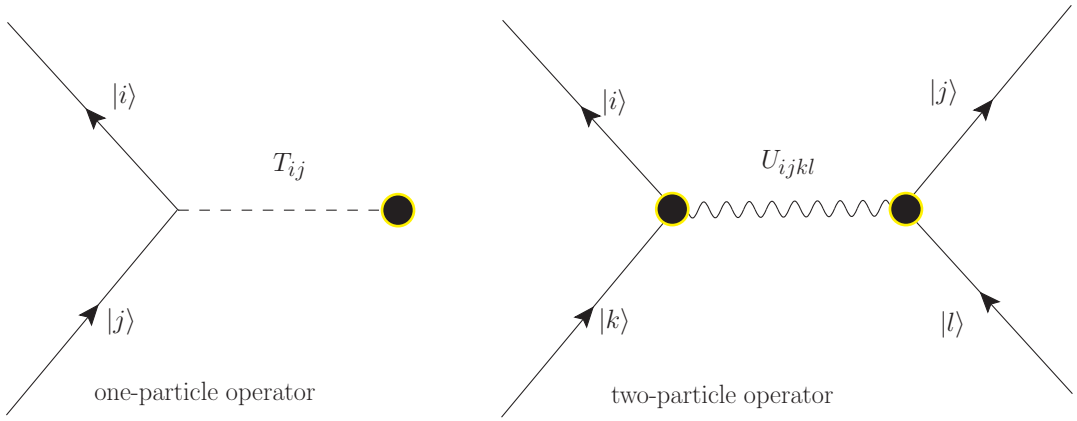

Figure 3.1: Diagrammatic representation of the one-particle and two-particle operators.

$$T_{tot} = \sum_{i,j} T_{ij} a_i^\dagger a_j, \tag{3.5}$$

$$V_{tot} = \frac{1}{2} \sum_{i,j,k,l} U_{ijkl} a_i^\dagger a_j^\dagger a_l a_k, \tag{3.6}$$

whose representations in Feynman's diagrammatic theory are shown in figure 3.1.

For the purpose of a rough derivation of these expressions let us consider a many body system with N-particles, which is described by the N-particle state or wave function $\psi(\mathbf{r}_1, \mathbf{r}_2, ..., \mathbf{r}_N)$ as a complex function in the $3N$-dimensional configuration space. This wave function can be also written as a product state of one particle functions with the corresponding symmetrization of fermions or bosons

$$\psi(\mathbf{r}_1, \mathbf{r}_2, ..., \mathbf{r}_N) = \sum_{\nu_1,...,\nu_N} B_{\nu_1,\nu_2,...\nu_N} \hat{S}_\pm \psi_{\nu_1}(\mathbf{r}_1)\psi_{\nu_2}(\mathbf{r}_2)...\psi_{\nu_N}(\mathbf{r}_N). \tag{3.7}$$

The one-particle operator for a single particle system in the first quantization is described by the coordinate $\mathbf{r}_j$ given by

$$T_j = \sum_{\nu_a,\nu_b} T_{\nu_a,\nu_b} |\psi_{\nu_b}(\mathbf{r}_j)\rangle\langle\psi_{\nu_a}(\mathbf{r}_j)|, \tag{3.8}$$

where

$$T_{\nu_a,\nu_b} = \int d\mathbf{r}_j \psi^*_{\nu_b}(\mathbf{r}_j) T(\mathbf{r}_j, \nabla_{\mathbf{r}_j}) \psi_{\nu_a}(\mathbf{r}_j). \tag{3.9}$$

The total one particle operator is the summation of each of these operators

$$T_{tot} = \sum_{j=1}^{N} T_j. \tag{3.10}$$

On the other side the two-particle operator in first quantization with coordinates $\mathbf{r}_i$, $\mathbf{r}_j$ with the basis states and $|\psi_{\nu_a}(\mathbf{r}_i)\rangle|\psi_{\nu_b}(\mathbf{r}_j)\rangle$ is arranged in the following way

$$V_{ij} = \sum_{\nu_a,\nu_b,\nu_c,\nu_d} V_{\nu_c\nu_d,\nu_a\nu_b}|\psi_{\nu_c}(\mathbf{r}_i)\rangle|\psi_{\nu_d}(\mathbf{r}_j)\rangle\langle\psi_{\nu_a}(\mathbf{r}_i)|\langle\psi_{\nu_b}(\mathbf{r}_j)|, \tag{3.11}$$

where,

$$V_{\nu_c\nu_d,\nu_a\nu_b} = \int d\mathbf{r}_i d\mathbf{r}_j \psi^*_{\nu_c}(\mathbf{r}_i)\psi^*_{\nu_d}(\mathbf{r}_j)V(\mathbf{r}_i - \mathbf{r}_j)\psi_{\nu_a}(\mathbf{r}_i)\psi_{\nu_b}(\mathbf{r}_j). \tag{3.12}$$

The total two-particle operator is

$$V_{tot} = \sum_{i>j}^{N} V_{ij} = \frac{1}{2}\sum_{i,j\neq i} V_{ij}. \tag{3.13}$$

We can apply T_{tot} and V_{tot} on a generalized state in the second quantization and get the results in the equations (3.5) and (3.6)[29]. For some cases the many body Hamiltonian in second quantization representation is reduced to much simpler terms. For instance if the localization of electrons is strong, then the interaction term reduces for the single band case to the following expression

$$V_{ijkl} = \left\{ \begin{array}{rl} V_{iiii} = U & \text{for single band model} \\ 0 & \text{else} \end{array} \right\}. \tag{3.14}$$

For the kinetic energy or hopping part, one can restrict the overlap between orbitals to the nearest neighbors, consequently leading to us a reduced expression for the many body Hamiltonian

$$\begin{aligned} H &= -\sum_{i,j,\sigma} t_{ij} c^\dagger_{i\sigma} c_{j\sigma} + U\sum_i n_{i\uparrow}n_{i\downarrow} + \epsilon_0 \sum n_{i\sigma} \\ &= -\sum_{<i,j>,\sigma} t c^\dagger_{i\sigma} c_{j\sigma} + \frac{U}{2}\sum_{i\sigma\sigma'} n_{i\sigma}n_{i\sigma'} + \epsilon_0 \sum n_{i\sigma}, \end{aligned} \tag{3.15}$$

which is the famous Hubbard model. In the one dimensional cases of the Hubbard model there are powerful techniques referred to as Bethe Ansatz techniques[37] or density matrix renormalization group (DMRG)[38, 39]. For the infinite dimensional case DMFT delivers exact results, but for the two or three-dimensional cases there are still many open questions. Here exact diagonalization or related methods give some insight, which is of tremendous importance for new developments from a methodological as well as

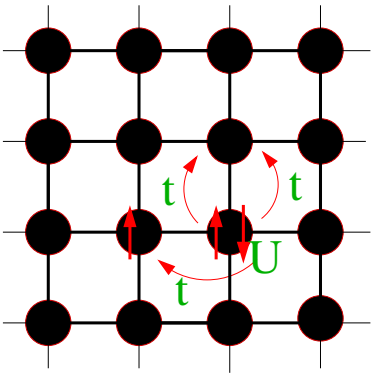

Figure 3.2: Graphical representation of the physical processes (hopping=kinetic term, interaction=on-site term) occurring in the Hubbard model for a quadratic two-dimensional lattice.

a physical point of view. For this purpose we want to show how exact diagonalization techniques are applied on the Hubbard model. The Hubbard model describes a collection of single orbital atoms placed at the nodes R_i of a periodic lattice. The orbitals overlap from site to site, so that the fermions can hop with an amplitude t_{ij}. If there is no hopping term then each of these atoms will have 4 eigenstates

$$|0\rangle, |\uparrow\rangle, |\downarrow\rangle, |\uparrow\downarrow\rangle, \tag{3.16}$$

with the corresponding energies

$$0, \epsilon_0, \epsilon_0, U + 2\epsilon. \tag{3.17}$$

The Hubbard model describes electrons with two spin directions $\sigma =\uparrow$ or $\sigma =\downarrow$, which are moving between localized states at neighboring lattice sites i and j. There is only an interaction between electrons, if two electrons meet on the same lattice site i, but they have simultaneously to satisfy the Pauli's principle. The Pauli principle applied to this case says if two electrons meet on the same lattice site i they have to have opposite spin directions. From this explanations, we can conclude that the kinetic energy is characterized by the hopping term t_{ij} and the interaction energy by the Coulomb repulsion U, which is sketched in figure 3.2. There is a competition between this two terms, because on the one side the kinetic part favors the electrons to be as mobile as possible, while on the other side the interaction energy is minimal, if the electrons stay far from each other, that means if the electrons are localized on different sites.

In the Hubbard model the long ranged Coulomb interaction is replaced by a extreme short ranged on-site interaction. Despite this rough reduction of the original system the Hubbard model captures many interesting properties of solids which range from metallic behaviour, insulating behaviour, metal-insulator transition, antiferromagnetism, ferromagnetism, superconductivity depending on the choice of parameters t, U, electron

filling, lattice type and spatial dimension[40]. Now we can consider some important cases for the Hubbard model:

1. $U \gg t$: doubly occupied states are energetically unfavoured. The main contribution to the low lying eigenstates comes from the configurations where there are few doubly occupied states as possible.

2. $n = 1$, half filling: Half filling means that the number of lattice sites is equal to the number of electrons, which occupy these sites. Also the partition of electrons between the two spin directions is equal. That means that half of the electrons have spin up and the other half the spin down direction.The movement of electrons is prevented by a potential energy barrier of height U. Depending on the dimensionality the system is insulating beyond the critical values U_C. If U is zero, then the system is a perfect metal at half filling.

3.3 Exact Diagonalization

In the last section we have considered some elementary properties of the Hubbard model, which are obtained by some analytical and numerical methods. Exact diagonalization techniques belong to these class of methods and they are very useful for many applications. They are often used as a reference for a new introduced many body method. Moreover these techniques serve as a basis for more advanced approaches like CPT[11, 12] or VCA[15, 13]. For these reasons let us give some overview over exact diagonalization techniques.

3.3.1 Generation of configurations for the Hubbard model

For the application of exact diagonalization to Hubbard- or Hubbard-like lattice models an important issue is the choice of a convenient basis. Binary representation of two spin states ± 1

$$n_i = \frac{\sigma_i + 1}{2} \in \{0, 1\}, \tag{3.18}$$

matches into this category and can be utilized for the generation of the basis states. In this way a series of basis states with fixed number of spins N^σ can be generated. Let us assume we have a fixed number of particles i.e. spins then the possible basis states and their integer representations are

$$\begin{aligned}
|\psi_1\rangle &= \{0, 0, \cdots, 0, 0, 1, 1, 1, \cdots, 1, 1\} & I_1 &= 2^N - 1 \\
|\psi_2\rangle &= \{0, 0, \cdots, 0, 1, 0, 1, 1, \cdots, 1, 1\} & I_2 &= 2^{N^\uparrow+1} - 1 + 2^{N^\uparrow-1} \\
|\psi_3\rangle &= \{0, 0, \cdots, 0, 1, 1, 0, 1, \cdots, 1, 1\} & I_3 &= 2^{N^\uparrow+1} - 1 + 2^{N^\uparrow-2} \\
&\vdots & &\vdots \\
|\psi_L\rangle &= \{1, 1, 1, \cdots, 1, 1, 0, 0, \cdots, 0, 0\} & I_L &= 2^N - 2^{N-N^\uparrow}.
\end{aligned}$$

For electronic systems the situation is different. In single band Hubbard Model a lattice site can be occupied by none, one spin-↑, spin-↓ or simultaneously by two electrons with spin-↑ and spin-↓. Therefore one needs a representation where this prescription in the occupation is included. In the second quantization representation we can in general write such a state as the application of creation operators of electrons on a vacuum state which is defined as

$$|\psi\rangle = \prod_{i=1}^{N^{\uparrow}} a_{i,\uparrow}^{\dagger} \prod_{j=1}^{N^{\downarrow}} a_{j,\downarrow}^{\dagger} |0\rangle, \tag{3.19}$$

or

$$|\psi\rangle = \prod_{i=1}^{N} \left(a_{i,\uparrow}^{\dagger}\right)^{n_i} \prod_{j=1}^{N} \left(a_{j,\downarrow}^{\dagger}\right)^{n_j} |0\rangle, \tag{3.20}$$

where,

$$n_i, n_j \in \{0, 1\}. \tag{3.21}$$

Let us assume creation operators are applied on the vacuum state and, thereby a state, which is occupied by two up and two down electrons $|\uparrow, 0, \downarrow, \uparrow\downarrow\rangle$ is generated. This state can be represented by $n^{\uparrow} = \{1, 0, 0, 1\}$ and $n^{\downarrow} = \{0, 0, 1, 1\}$, which can also be alternatively represented by two integer numbers, i.e., in this case by $I = \{9, 3\}$. This all means that a lattice site can be empty, occupied by a spin up electron ↑ by a spin down electron ↓ or by two electrons with different spin. The resulting number of basis states is 4^N. Because of the exponential increase of these basis states with the lattice sites, conservation principles, respectively quantum numbers, have to be taken into account. We can take the spin as a quantum number to reduce the number of basis states. The z-component of the spinoperator S^z

$$S^z = \sum_{i=1}^{N} S_i^z, \tag{3.22}$$

commutes with the Hamiltonian, therefore the Hamiltonian is block diagonal in the sections with fixed S^z values, i.e, fixed numbers N^{σ} of σ-spins. The number of basis states for fixed number of spins N^{σ} becomes

$$L = \begin{pmatrix} N \\ N^{\uparrow} \end{pmatrix} \cdot \begin{pmatrix} N \\ N^{\downarrow} \end{pmatrix}. \tag{3.23}$$

The translation and rotation invariance reduces the number of basis states even further. The basis states with the spin quantum number generated by this way can be used to calculate the matrix elements.

3.3.2 Calculation of matrix elements for the Hubbard model

The next important point for exact diagonalization is the evaluation of the matrix elements,

$$H_{\mu\nu} = \langle\psi_\mu|H|\psi_\nu\rangle. \tag{3.24}$$

For this purpose we can split the Hubbard Hamiltonian into two parts, the hopping part (kinetic part) and the onsite part (interaction part), which can be separately calculated. Let us start with the calculation of the onsite part

$$H_{onsite} = U\sum_i n_{i\uparrow}n_{i\downarrow} + \epsilon_0\sum n_{i\sigma}. \tag{3.25}$$

The basis states are characterized by occupation numbers $|\psi_\nu\rangle = |\{n_{i,\sigma}\}\rangle$, for all lattice sites i and spin directions σ, $n_{i\sigma} \in \{0,1\}$. Obviously this part is diagonal in our basis. On the other side the hopping part of the Hamiltonian

$$H_{hop} = -\sum_{i,j,\sigma} t\left(c^\dagger_{i\sigma}c_{j\sigma} + c^\dagger_{j\sigma}c_{i\sigma}\right), \tag{3.26}$$

is off-diagonal in the occupation basis. Here one can perform a Fourier transformation, which will result into a diagonal hopping term

$$H_{hop} = \frac{1}{\sqrt{N}}\sum_{\mathbf{k}} \epsilon_{\mathbf{k}} c^\dagger_{\mathbf{k}}c_{\mathbf{k}}, \tag{3.27}$$

where,

$$c^\dagger_{i\sigma} = \frac{1}{N}\sum_{\mathbf{k}} e^{i\mathbf{k}\mathbf{r}_i}c^\dagger_{\mathbf{k}\sigma}, \tag{3.28}$$

$$\epsilon_{\mathbf{k}} = -2t\sum_{j=1}^{D} cos(\mathbf{k}_j) \quad , \quad D\text{...dimension}, \tag{3.29}$$

but in the **k**-space onsite term becomes off diagonal. The straight forward calculation of the hopping part of the Hubbard Hamiltonian is not so easy. To simplify the consideration and also the calculation procedure, we look at the hopping part for fixed lattice sites and fixed spin

$$H^l = -t\left(c^\dagger_{i_0\sigma_0}c_{j_0\sigma_0} + c^\dagger_{j_0\sigma_0}c_{i_0\sigma_0}\right). \tag{3.30}$$

Application of H^l to a basis state $|\psi_\nu\rangle = |\{n^\nu_{i\sigma}\}\rangle$ results in zero if $n_{i_0\sigma_0}$ and $n_{j_0\sigma_0}$ are both occupied or empty, i.e.,

$$H^l|\{n^\nu_{i\sigma}\}\rangle = 0 \quad \text{if} \quad n_{i_0\sigma_0} = n_{j_0\sigma_0}. \tag{3.31}$$

Otherwise it leads to another basis state $|\{n_{i\sigma}^{\nu'}\}\rangle$, which differs from the basis state $|\{n_{i\sigma}^{\nu}\}\rangle$ through the exchange of occupation number $n_{i_0\sigma_0}^{\nu}$ and $n_{j_0\sigma_0}^{\nu}$. Indeed there is only one hopping process H^l mediating between two basis states. The crucial question at this point is the value of this matrix element. We get for the matrix element the following condition

$$h_{\nu'\nu} = \left\{ \begin{array}{lll} -tS & \text{if} & \begin{array}{rl} n_{i,-\sigma_0}^{\nu'} = n_{i,-\sigma_0}^{\nu} & \forall i \\ n_{i,\sigma_0}^{\nu'} = n_{i,\sigma_0}^{\nu} & \forall i \neq i_0, j_0 \\ n_{i_0,\sigma_0}^{\nu'} = n_{j_0,\sigma_0}^{\nu} & \\ n_{j_0,\sigma_0}^{\nu'} = n_{i_0,\sigma_0}^{\nu} & \end{array} \\ 0 & \text{else} & \end{array} \right\}. \tag{3.32}$$

The hopping process leads to a sign S, because the electrons are fermions and they have to satisfy Fermi-Dirac statistics. Therefore we have to take care of the sign in the calculation of the matrix elements concerning the hopping part.

3.3.3 Lanczos algorithm

After studying the generation of the basis states and the evaluation of the matrix elements, we are going on with the diagonalization, in order to determine the ground state and the corresponding energy. We are interested in the ground state energy and excited states, because the quantum features of many body systems show up at very low temperatures. It is advantageous to have a basis in which the Hamiltonian matrix is sparse, i.e., most of the matrix elements are zero. This is fulfilled for the Hubbard model in the occupation basis. Because these matrices grow exponentially with increasing lattice sites one needs methods which can handle the diagonalisation of large matrices. The Lanczos Algorithm[41] belongs to this class of methods. In this algorithm the diagonalisation is not done in the full Hilbert space $\mathcal{H}$ ($\dim\mathcal{H} = N$), instead in a subspace called Krylov space $\mathcal{K}$ ($\dim\mathcal{K} = M$), where $M \ll N$.

The starting point is a normalized random state vector $|x_0\rangle$, which may fulfill a desired symmetry, in order to guarantee the convergence towards the lowest energy. The new basis vectors are obtained by repeated application of the Hamiltonian on this basis state

$$\left\{H|x_0\rangle, H^2|x_0\rangle, \cdots, H^M|x_0\rangle\right\}. \tag{3.33}$$

By this sequence the convergence towards the ground state can be easily reached, which

can be verified for large M

$$\begin{aligned} H^M|x_0\rangle &= H^M \sum_{j=0}^{N} c_j|\psi_j\rangle \\ &= \sum_{j=0}^{N} c_j \epsilon_j^M |\psi_j\rangle \\ &= c_0\epsilon_0^M \left(|\psi_0\rangle + \sum_{j=1}^{N} \frac{c_j}{c_0} \left(\frac{\epsilon_j}{\epsilon_0}\right)^M |\psi_j\rangle \right), \end{aligned} \tag{3.34}$$

where ϵ_j and $|\psi_j\rangle$ are eigenvalues and eigenvectors of the Hamiltonian. The obtained condition $|\epsilon_0| < |\epsilon_j|$ for $j > 0$ and the requirement of large M ensures that the expression $H^M|x_0\rangle$ converges to the ground state $|\psi_0\rangle$. This kind of calculation can be enhanced by incorporating Gram Schmidt processes of orthogonalization. This is done within the Lanczos algorithm, where firstly the energy expectation value relative to the randomly chosen $|x_0\rangle$ state is calculated in the following way

$$a_0 = \langle x_0|H|x_0\rangle. \tag{3.35}$$

The next basis state is generated by the application of the Hamilton operator on this state vector

$$|\tilde{x}_1\rangle = H|x_0\rangle - a_0|x_0\rangle. \tag{3.36}$$

This new basis state is orthogonal to the first basis state

$$\begin{aligned} \langle x_0|\tilde{x}_1\rangle &= \langle x_0|\{H|x_0\rangle - a_0|x_0\rangle\} \\ &= \langle x_0|H|x_0\rangle - a_0\langle x_0|x_0\rangle = 0, \end{aligned}$$

and has to be normalized like the first starting state

$$|x_1\rangle = \frac{|\tilde{x}_1\rangle}{||\tilde{x}_1||}. \tag{3.37}$$

One can go on and generate another basis state from the first two basis states using the relation

$$|\tilde{x}_2\rangle = H|x_1\rangle - a_1|x_1\rangle - b_1|x_0\rangle. \tag{3.38}$$

The coefficients a_1 and b_1 can be selected in such a way, which guarantees that the basis state $|\tilde{x}_2\rangle$ is orthogonal to the basis states $|\tilde{x}_0\rangle$ and $|\tilde{x}_1\rangle$. To find an expression for a_1 and b_1 we consider the dot product of $|\tilde{x}_2\rangle$ with $|x_0\rangle$ and $|x_1\rangle$

$$\langle x_0|\tilde{x}_2\rangle = \langle x_0|H|x_1\rangle - a_1\langle x_0|x_1\rangle - b_1\langle x_0|x_0\rangle = 0,$$

$$\Rightarrow b_1 = \langle x_0|H|x_1\rangle, \tag{3.39}$$

$$\langle x_1|\tilde{x}_2\rangle = \langle x_1|H|x_1\rangle - a_1\langle x_1|x_1\rangle - b_1\langle x_1|x_0\rangle = 0,$$

$$\Rightarrow a_1 = \langle x_1|H|x_1\rangle. \tag{3.40}$$

These procedures for the generation of the basis states can be generalized and for any basis state $|x_{n+1}\rangle$ the following recursion relations are defined by

$$\begin{aligned} |\tilde{x}_{n+1}\rangle &= H|x_n\rangle - a_n|x_n\rangle - b_n|x_{n-1},\rangle \\ a_n &= \langle x_n|H|x_n\rangle, \\ b_n &= \langle x_{n-1}|H|x_n\rangle, \\ |x_{n+1}\rangle &= \frac{|\tilde{x}_{n+1}\rangle}{||\tilde{x}_{n+1}||}. \end{aligned}$$

The Hamiltonian matrix is tridiagonal in this orthogonal basis

$$H_{i,j} = \begin{pmatrix} a_0 & b_1 & 0 & 0 & 0 & \cdots \\ b_1 & a_1 & b_2 & 0 & 0 & \cdots \\ 0 & b_2 & a_2 & b_3 & 0 & \cdots \\ 0 & 0 & b_3 & a_3 & b_4 & \\ \vdots & \vdots & & \ddots & \ddots & \ddots \end{pmatrix} \tag{3.41}$$

and can be diagonalized easily.

3.3.4 Band Lanczos algorithm

The Band Lanczos algorithm[42] is a generalized version of the conventional Lanczos algorithm. Here, at the beginning instead of a random vector $|x_0\rangle$ a set of vectors

$$\{|x_1\rangle, |x_2\rangle, \cdots, |x_L\rangle\}, \tag{3.42}$$

is used. It is applicable for problems like matrices with multiple or clustered eigenvalues. Band Lanczos is efficient to deal with many vectors simultaneously. Again the basis here for the block Krylov space is generated by successive application of the Hamiltonian on these basis states

$$\begin{aligned} \{|x_1\rangle, |x_2\rangle, \cdots, |x_L\rangle\} \quad &, \quad \{H|x_1\rangle, H|x_2\rangle, \cdots, H|x_L\rangle\} \\ &\cdots \quad \left\{H^M|x_1\rangle, H^M|x_2\rangle, \cdots, H^M|x_L\rangle\right\}. \end{aligned} \tag{3.43}$$

The aim here is to find orthonormal vectors

$$\{|x_1\rangle, |x_2\rangle, \cdots, |x_j\rangle\}, \tag{3.44}$$

which give a basis for the subspace spanned by the first j linear independent vectors of the block Krylov sequence. Band Lanczos with multiple starting vectors bring some difficulties, which should be considered and this is related to deflation of Krylov sequence. In the case of a single starting vector the Lanczos algorithm terminates after j iterations, if the next vector is linearly dependent of the previous vectors. In this way the full Kyrlov space is exhausted and adding additional vectors would not expand the Krylov subspace. In the case of multiple starting vectors the appearance of linearly dependent vectors do not give any hint that the Kylov space is exhausted. These linearly dependent vectors do not give any new information, therefore they have to be identified and eliminated. The process of identifying and eliminating of linearly dependent vectors is called exact deflation.

3.3.5 Many body Green's function

After the determination of the ground state and ground state energy by exact diagonalization techniques the many body Green's function can be evaluated by the Lehman representation

$$\begin{aligned} G_{ij}(\omega) &= G_{ij,e}(\omega) + G_{ij,h}(\omega) \\ &= \langle\psi_0|c_i^\dagger \frac{1}{\omega - (H - E_0)} c_j|\psi_0\rangle + \langle\psi_0|c_i \frac{1}{\omega + (H - E_0)} c_j^\dagger|\psi_0\rangle, \end{aligned} \tag{3.45}$$

where the first term is related to photo emission spectroscopy (PES) and the second one gives the inverse photo emission spectroscopy (IPES). The indices i and j of the operator contain the lattice site, spin and orbital quantum number. Let us constrain ourselves here on the first term. We can insert the completeness relation

$$\mathbb{1} = \sum_\nu |\psi_\nu\rangle\langle\psi_\nu|, \tag{3.46}$$

into the first term and obtain

$$\langle\psi_0|c_i^\dagger \frac{1}{\omega - (H - E_0)} c_j|\psi_0\rangle = \sum_\nu \langle\psi_0|c_i^\dagger|\psi_\nu\rangle \frac{1}{\omega - E_\nu + E_0} \langle\psi_\nu|c_j|\psi_0\rangle. \tag{3.47}$$

The same procedure can also be applied to the second term. Here one can introduce the following notations for the first and second term

$$Q_{i\nu}^e = \langle\psi_0|c_i^\dagger|\psi_\nu\rangle \quad , \quad Q_{j\nu}^{e*} = \langle\psi_\nu|c_j|\psi_0\rangle, \tag{3.48}$$

$$E_\nu^e = E_\nu - E_0 < 0 \quad , \quad E_\mu^h = -E_\mu + E_0 > 0, \tag{3.49}$$

and using these abbreviations we get the following compact form for the complete Green's function

$$G_{ij}(\omega) = \sum_\nu \frac{Q_{i\nu}^e \cdot Q_{j\nu}^{e*}}{\omega - E_\nu^e} + \sum_\mu \frac{Q_{i\mu}^{h*} \cdot Q_{j\mu}^h}{\omega - E_\mu^h}. \tag{3.50}$$

This can be rewritten in a more compact version by combining the E^e_ν and E^h_μ into the $E_{\tilde{\nu}}$ and also in a equivalent way the terms Q^e and Q^h into the Q

$$G_{ij}(\omega) = \sum_{\tilde{\nu}} \frac{Q_{i\tilde{\nu}} \cdot Q_{j\tilde{\nu}}}{\omega - E_{\tilde{\nu}}}. \tag{3.51}$$

The ground state $|\psi_0\rangle$ is calculated by the standard Lanczos technique. Note that using the Band Lanczos algorithm, all matrix elements $\langle\psi_0|c_i^\dagger|\psi_\nu\rangle$ and $\langle\psi_\nu|c_j|\psi_0\rangle$ can be calculated at once, using the set $|x_i\rangle = c_i^\dagger|\psi_0\rangle$ as starting vectors. For details we refer to Ref[43].

Here let us recapitulate our status at this point. Using exact diagonalization techniques and Lehman representation many body Green's can be calculated. Unfortunately one is here restricted to very small systems, because of the exponential increase of the basis states. Here one needs some clever ideas out of this dilemma to calculate the Green's function of an infinite large system. Cluster perturbation theory (CPT), which will be explained in the next section, is a simple way of doing this.

3.4 Cluster perturbation theory

In the Hubbard-I approximation the starting point is the atomic limit, because the local part of the Hubbard model can be solved easily. Then one embeds the atom into the lattice. So the approximation in the Hubbard I approximation is, that the self-energy of the lattice system is replaced by the self-energy of the atomic system. This self-energy can be used to calculate one electron Green's function. A more general form of this simple approximation is the CPT[11, 12]. For a rough derivation of the CPT let us start with the Hubbard model written with lattice site position vector $\mathbf{R}$ and spin index σ

$$H = -\sum_{<\mathbf{R},\mathbf{R}'>,\sigma} t c^\dagger_{\mathbf{R}\sigma} c_{\mathbf{R}'\sigma} + \frac{U}{2} \sum_{\mathbf{R}\sigma\sigma'} n_{\mathbf{R}\sigma} n_{\mathbf{R}\sigma'}. \tag{3.52}$$

In the cluster perturbation theory the lattice with L sites is separated into L/L_C disconnected clusters. Here L_C is the number of lattice sites inside each cluster. After this procedure the lattice Hamiltonian can be written as

$$\begin{aligned} H &= H' + V \\ &= \sum_{\mathbf{R},a,b} H_0^{cl}(\mathbf{R})_{a,b} + H_I^{cl}(\mathbf{R})_{a,b} + \sum_{\mathbf{R},\mathbf{R},a,b'} H_0^{icl}(\mathbf{R},\mathbf{R}')_{a,b}, \end{aligned} \tag{3.53}$$

where H' is the cluster Hamiltonian and V contains the hopping terms between the clusters and is treated perturbatively. This procedure is sketched in figure 3.3. The first sum in the second line includes the hopping and interaction processes inside the cluster, the second sum gives the intra cluster coupling, $\mathbf{R}$ denotes the individual clusters and a,b are quantum numbers within the cluster.

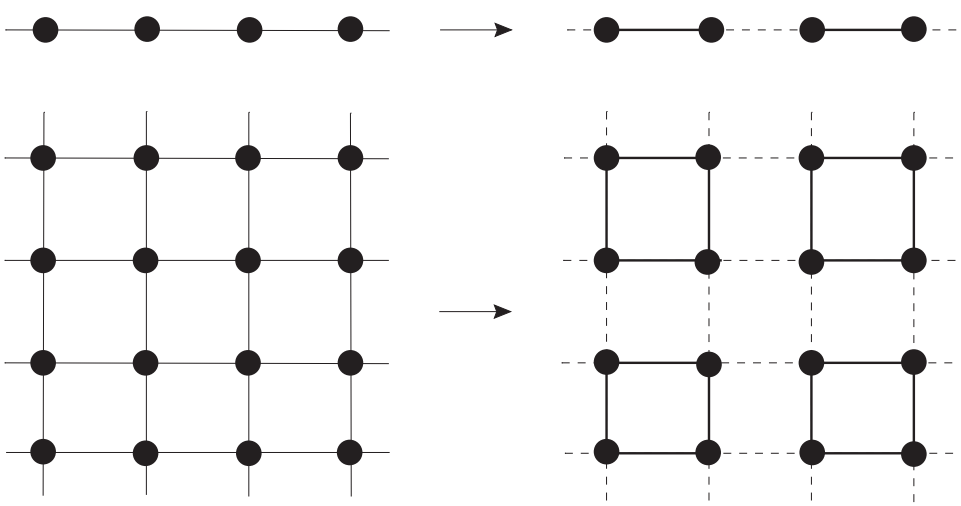

Figure 3.3: Schematic representation of the cluster perturbation theory. The original lattice system is replaced by a system of equivalent clusters. These clusters are connected in a perturbative way. In two-dimensional systems the shape of the chosen clusters is not unique as it is the case for the one-dimensional clusters.

By the method of strong coupling perturbation theory[44, 45] the following expression is obtained for the lattice Green's function in the lowest order

$$G^{-1}_{\mathbf{R}a,\mathbf{R}'b}(\omega) = G'^{-1}_{\mathbf{R},a,b}(\omega) - V_{\mathbf{R}a,\mathbf{R}'b}, \tag{3.54}$$

where G' is the cluster Green's function. Because of the tiling of the original system into finite clusters translational invariance is lost. We can restore the translational invariance in terms of wave vectors $\mathbf{k}$, which belong to the super lattice of the corresponding Brillouin zone. So we can perform a partial Fourier transformation and the following expression is obtained for the Green's function

$$G^{-1}_{a,b}(\mathbf{k},\omega) = G'^{-1}_{a,b}(\omega) - V_{a,b}(\mathbf{k}). \tag{3.55}$$

At this point we have a mixed representation of quantum numbers a and b within the cluster and $\mathbf{k}$ wave vector within the super cell BZ. This obstacle can be overcomed by a Fourier transformation at the level of clusters because the translation invariance is broken at this level. Finally the restoration of the translational invariance is re-established by this Fourier transformation and the final result is given by

$$G_{per.}(\mathbf{k},\omega) = \frac{1}{L_C}\sum_{\mathbf{r}_a,\mathbf{r}_b} e^{-i\mathbf{k}(\mathbf{r}_a-\mathbf{r}_b)} G_{a,b}(\mathbf{k},\omega), \tag{3.56}$$

where $\mathbf{r}_a, \mathbf{r}_b$ are the lattice position vectors according to the quantum number a and b.

In CPT the self-energy of the original system, which is in general not known, is approximated by the self-energy of the chosen cluster. This can be shown by using CPT equation and the Dyson equation

$$\begin{aligned} G^{-1}(\mathbf{k},\omega) &= G'(\omega) - V(\mathbf{k}) \\ G^{-1}(\mathbf{k},\omega) &= G_0(\mathbf{k},\omega) - \Sigma(\omega). \end{aligned} \tag{3.57}$$

From these equations we can extract the so-called cluster Green's function G' and free non-interacting Green's function G_0

$$\begin{aligned} G'^{-1}(\mathbf{k},\omega) &= \omega - t' - \Sigma'(\omega) \\ G_0^{-1}(\mathbf{k},\omega) &= \omega - t' - V(\mathbf{k}), \end{aligned} \tag{3.58}$$

and inserting these equations into the CPT Green's function we obtain an expression

$$\begin{aligned} G^{-1}(\mathbf{k},\omega) &= \omega - t' - \Sigma'(\omega) - V(\mathbf{k}) \\ &= G_0^{-1}(\mathbf{k},\omega) - \Sigma'(\omega), \end{aligned} \tag{3.59}$$

which looks like the Dyson equation with the cluster self-energy Σ'. So in the CPT approximation the self-energy of the whole lattice problem is replaced by self-energy of the cluster. Only for the case of small clusters the self-energy can be calculated exactly by some numerical methods (e.g. Lanczos algorithm). The inter cluster hopping V can be treated as a perturbation of the system of disconnected clusters with intra cluster hopping t'. The Green's function can be calculated by the summation of diagrams in perturbation theory to all orders in U and V. Within the CPT the vertex corrections are neglected[46]. CPT becomes exact in the limits where cluster sites are infinite $L_C \to \infty$, $U = 0$ and $t/U = 0$. Correlations beyond cluster extensions are neglected. There is no self consistent condition, i.e. there is no feedback of the resulting Green's function on the cluster embedding and there is no feedback of the Weiss mean field. For these reasons CPT cannot describe different phases of a thermodynamic system or phase transitions. Consequently this approach cannot describe metal-insulator transition. Many of these drawbacks can be overcomed in the framework of the variational cluster approximation.

3.5 Variational cluster approximation (VCA)

To overcome the drawbacks of CPT one needs a self consistent embedding scheme. This comes from a variational principle of a general thermodynamic potential, defined in terms of dynamical quantities such as self-energy or Green's function. These are related to the one-particle excitation spectrum and static quantities like the grand potential which is connected to thermodynamics. The physical self-energy is obtained by requiring that the thermodynamic potential be stationary. Such a thermodynamic potential can be derived by using the Luttinger Ward functional $\hat{\Phi}_U[G]$[47, 46].

Luttinger Ward functional is the sum over all closed linked Feynman diagrams as shown in figure 3.4[48]. In practice such a sum over infinitely many diagrams can not be

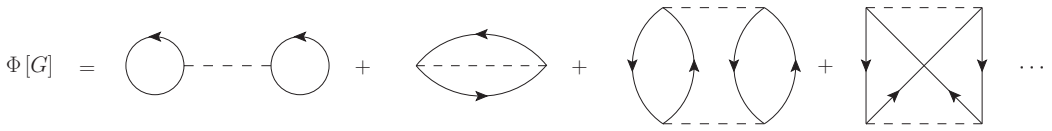

Figure 3.4: Diagrammatic expansion of the Luttinger Ward functional $\Phi\,[G]$.

done. There is the possibility the truncate the Luttinger Ward functional, i.e., a selected class of diagrams are taken into account. In many cases these diagrams are the ladder and bubble diagrams. One of such approximations is the GW approximation. Here we will take another way as the truncation of the Luttinger Ward functional. For this purpose let us consider some properties of Luttinger Ward functional obtained from the study of the diagrammatic perturbation theory. Luttinger Ward functional is universal in interaction U, i.e., two systems with the same interaction, but different one-particle parameter t are described by the same Luttinger Ward functional and it is vanishing for a non-interacting fermionic system. Functional derivative of the Luttinger Ward functional gives another functional

$$\frac{1}{T}\frac{\partial\hat{\Phi}_U[G]}{\partial G} = \hat{\Sigma}_U[G], \tag{3.60}$$

and the evaluation of this functional on the physical Green's function gives the real physical self-energy

$$\hat{\Sigma}_U[G_{t,U}] = \Sigma_{t,U}. \tag{3.61}$$

At this point we can do a Legendre transformation of the Luttinger Ward functional

$$\hat{F}_U[\Sigma] = \hat{\Phi}_U[\hat{G}_U[\Sigma]] - Tr(\Sigma\hat{G}_U[\Sigma]), \tag{3.62}$$

and obtain a functional which depends on the self-energy. The functional derivative of this Legendre transformed Luttinger Ward functional gives also another functional

$$\begin{aligned}
\frac{1}{T}\frac{\delta\hat{F}_U[G]}{\delta\Sigma} &= \frac{1}{T}\frac{\delta}{\delta\Sigma}\left(\hat{\Phi}_U[\hat{G}_U[\Sigma]] - Tr(\Sigma\hat{G}_U[\Sigma]\right) \\
&= \frac{\delta\hat{\Phi}_U[\hat{G}_U[\Sigma]]}{\delta G}\frac{\delta\hat{G}[\Sigma]}{\delta\Sigma} - \hat{G}[\Sigma] - \Sigma\frac{\delta\hat{G}[\Sigma]}{\delta\Sigma} \\
&= \Sigma\frac{\delta\hat{G}[\Sigma]}{\delta\Sigma} - \hat{G}[\Sigma] - \Sigma\frac{\delta\hat{G}[\Sigma]}{\delta\Sigma} \\
&= -\hat{G}[\Sigma],
\end{aligned} \tag{3.63}$$

and the evaluation of this functional on the physical real self-energy gives the Green's function

$$\hat{G}[\Sigma] = G. \tag{3.64}$$

We can use this expression to define the self-energy functional

$$\hat{\Omega}_{t,U}[\Sigma] = \mathrm{Trln}\left(\frac{1}{G_{t,0}^{-1} - \Sigma}\right) + \hat{F}_U[\Sigma]. \tag{3.65}$$

The functional derivative of the self-energy functional gives an expression

$$\frac{1}{T}\frac{\delta\hat{\Omega}_{t,U}[\Sigma]}{\delta\Sigma} = \frac{1}{G_{t,0}^{-1} - \Sigma} - \hat{G}[\Sigma], \tag{3.66}$$

which is very similar to the Dyson equation. It is obvious that the stationary point of the self-energy functional

$$\frac{\delta\hat{\Omega}_{t,U}[\Sigma]}{\delta\Sigma} = 0 \tag{3.67}$$

corresponds to the solution of the equation

$$\hat{G}[\Sigma] = \frac{1}{G_{t,0}^{-1} - \Sigma}, \tag{3.68}$$

where no closed form for the functional exists. We haven't used any approximation up to this point. It is generally not possible to calculate the self-energy functional. Therefore some approximations are necessary for the construction and evaluation of the stationary point of the self-energy functional. One needs an approximation, which can be systematically improved. Variational cluster approach matches into this criterion.

In variational cluster approximation one restricts the domain of the functional, i.e., a mapping to a reference system is done, where it is possible to evaluate the self-energy functional

$$\hat{\Omega}_{t',U}[\Sigma] = \mathrm{Trln}\left(\frac{1}{G_{t',0}^{-1} - \Sigma}\right) + \hat{F}_U[\Sigma]. \tag{3.69}$$

For the original system and for the reference system the Legendre transformed Luttinger Ward functionals $F_U[\Sigma]$ are the same because of the universality of $F_U[\Sigma]$. This can be exploited or utilized to obtain an expression, which is independent of $F_U[\Sigma]$ by subtracting the self-energy functional for the original system from the self-energy functional for the reference system:

$$\hat{\Omega}_{t,U}[\Sigma] = \hat{\Omega}_{t',U}[\Sigma] + \mathrm{Trln}\left(\frac{1}{G_{t,0}^{-1} - \Sigma}\right) - \mathrm{Trln}\left(\frac{1}{G_{t',0}^{-1} - \Sigma}\right).$$

We consider a reference system with fixed U, but different one particle parameters t' and assume that the self energy of the reference system can be obtained for any t'. This is demonstrated in figure 3.6.

Then the grand potential functional can be evaluated on the subspace of self-energies $\Sigma_{t',U}$ parametrized by one particle parameter t'. This idea is visualized in figure 3.5,

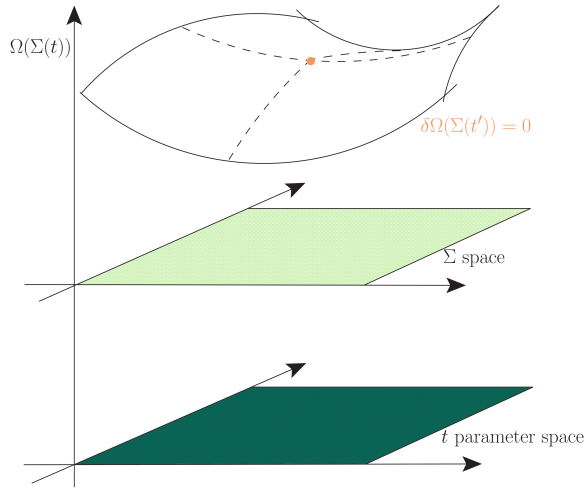

Figure 3.5: Grand potential Ω is calculated in the space of the trial reference self-energies $\Sigma(t)$ parametrized in the space of one-particle parameters. The optimal values for the one-particle parameters are reached at the point, where the grand potential Ω becomes stationary.

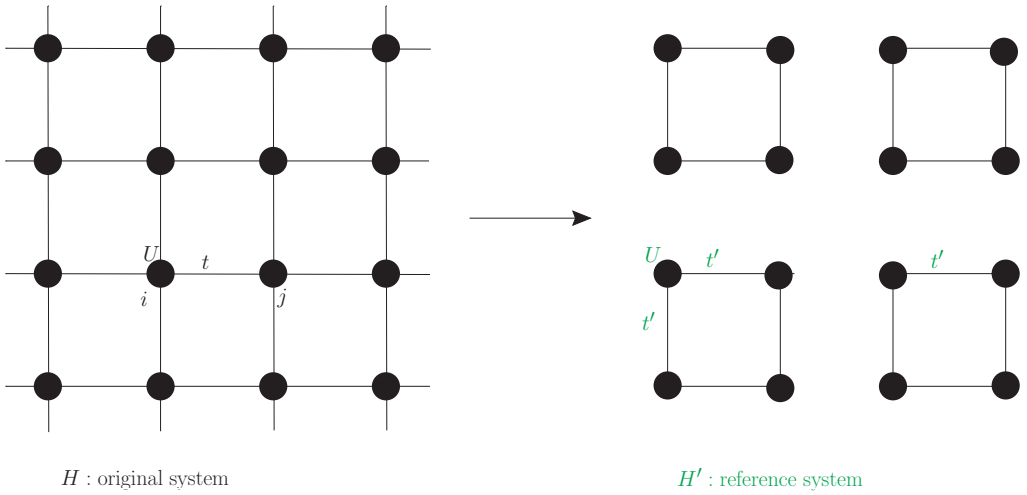

Figure 3.6: Grand potential calculation of the original system is replaced by an accessible system, e.g., clusters with the restored symmetry with optimized parameters.

where for a area of one particle parameters a space of self-energies is identified. At the physical self-energy with optimized one-particle parameters the grand potential is minimized. For this procedure one can select clusters as the reference system, because their self-energy $\Sigma_{t',U}$ for different one-particle parameters is exactly available. If we insert these self-energies into the self-energy functional it becomes an ordinary function

$$\Omega(t') \equiv \hat{\Omega}_{t,U}(\Sigma_{t',U}) \tag{3.70}$$

Here we can make use of Green's function of the cluster perturbation theory (CPT). In this approximation the following expression is obtained for the grand potential functional[15, 13, 46]

$$\Omega(t') = \Omega^{Cl} + \mathrm{Trln}\left(\mathbf{G}_{\mathrm{CPT}}\right) - \mathrm{Trln}\left(\mathbf{G}^{(Cl)}\right). \tag{3.71}$$

The final step is to find a stationary point of this function

$$\frac{\partial \Omega(t')}{\partial t'} = 0 \quad \text{for} \quad t' = t_{\mathrm{opt}}. \tag{3.72}$$

An explicit expression for this equation can be obtained either by exact frequency integration or by numerical frequency integration[43, 49].

3.6 Dynamical vertex approximation (DΓA)

Until now we have considered the methods, where the correlations are kept up to small cluster sizes. But correlations in larger order can be included within the within interaction channels of diagrammatic methods.

Dynamical vertex approximation belongs to the diagrammatic class of methods, which goes beyond standard DMFT. It keeps on the one hand the important local correlations of DMFT and on the other hand also the non-local correlations. Therefore DΓA allows us to deal with many physical phenomena such as spin fluctuations, magnons, quantum criticality, superconductivity appearing at low temperatures because of non-local correlations. DΓA can be seen as the natural extension to the DMFT, because in DMFT the one-particle fully irreducible vertex is assumed to be local, i.e., the self energy is completely local. On the other side DΓA approach assumes that the n-particle fully irreducible vertex Γ_{ir} is local[14], which goes beyond DMFT and is demonstrated in figure 3.7[50].

Let us consider the main steps of the DΓA algorithm. The starting point is an arbitrarily chosen local Green's function $G_{ii}(\omega)$. The next step is the calculation of the fully irreducible vertex Γ_{iiii} from the diagrammatic studies. In a practical calculation Γ_{iiii} is calculated through local parquet equations[51, 52, 53] out of the three frequency charge and spin susceptibilities obtained by the solution of the Anderson impurity model numerically via exact diagonalization or CT-QMC.

The second step is the calculation of the non-local irreducible vertex Γ_{ijkl} out of the fully irreducible vertex Γ_{iiii}. For this purpose one has to sum over all reducible

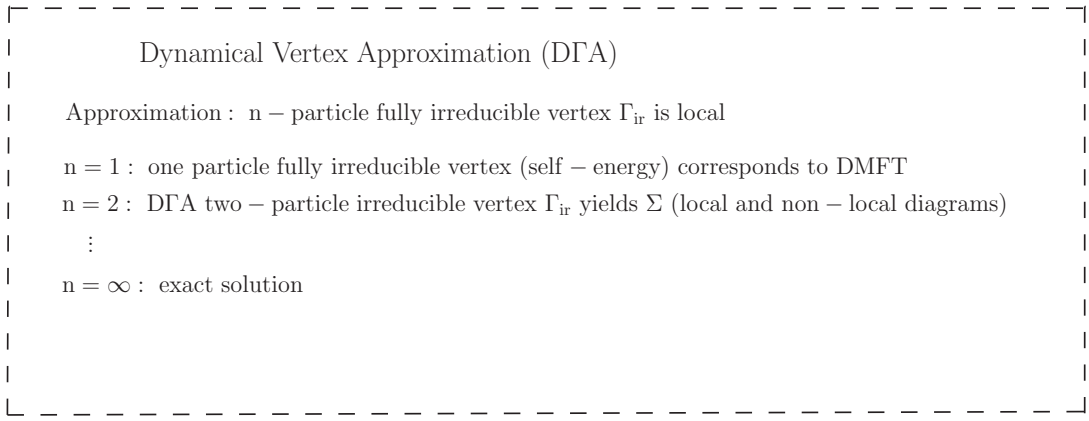

Figure 3.7: Dynamical vertex approximation and its connection to DMFT in a short schematic table representation.

diagrams. This summation can be in principle done within the parquet equations, but in a practical application this evaluation is a intricate challenge. Therefore the evaluation of the parquet equations in this step can be approximated by restricting the summation of the Parquet diagrams to the particle-hole channels, i.e, the particle-particle channels are neglected. This approximation here is justified for cases like the antiferromagnetic phase transition, where the Parquet diagrams to the particle-hole channels are dominating. On the other side for the considerations of physical phenomena like the superconductivity one has also to take into account the Parquet diagrams to the particle-particle channels.

In the third step the non local self-energy $\Sigma_{ij}(\mathbf{k},\omega)$ can be easily extracted from the non-local irreducible vertex Γ_{ijkl} through an exact equation[52, 53]:

$$\Sigma(\mathbf{k},\omega) = U\frac{n}{2} - T^2U \sum_{\mathbf{k}'\mathbf{q}\nu\nu'} \Gamma^{\nu\nu'\omega}_{\mathbf{k}\mathbf{k}'\mathbf{q}} G(\mathbf{k}'+\mathbf{q},\nu'+\nu)G(\mathbf{k}',\nu')G(\mathbf{k}+\mathbf{q},\omega+\nu'), \quad (3.73)$$

derived from the Heisenberg equation of motion, where $\mathbf{k}$, $\mathbf{k}'$, $\mathbf{q}$ are the wave vectors and ω, ν, ν' are the corresponding Matsubara frequencies, n is the number of electrons per lattice site, $\Gamma^{\nu\nu'\omega}_{\mathbf{k}\mathbf{k}'\mathbf{q}}$ is the reducible four point vertex, Gs are the Fourier transformation non local Green's functions G_{ij}.

At the last step one can write the local and non-local Green's function by Dyson equation

$$G(\mathbf{k},\omega) = \frac{1}{i\omega - \epsilon_{\mathbf{k}} + \mu - \Sigma(\mathbf{k},\omega)}, \quad (3.74)$$

and then go back to the step one and iterate until convergence is reached. This method is very powerful compared to VCA or C-DMFT, but it's practical implementation is a great challenge from the mathematical and numerical point of view.

3.7 Density functional theory combined with VCA

After the introduction of variational cluster approximation as a many body method, we are going to combine it with the density functional theory for the correlated compounds. Before, it is useful to give a small overview of density functional theory. This is useful on the one side for the identification of the important steps and approximations and on the other site for the interpretation of results which are used as the input for VCA calculations.

3.7.1 Overview over density functional theory

There are approximate solutions of the Schrödinger equation for the electronic wave function with several electrons. In density functional theory (DFT) instead of putting effort on the electronic wave function, an alternative approach is done, where the central quantity of interest is the electron density function $n(\mathbf{r})$. There are two essential advantages of DFT which should be considered here. DFT focuses on the quantities in the 3-dimensional space like the electronic density of ground state $n_0(\mathbf{r})$ or the exchange correlation hole density $n_{xc}(\mathbf{r}, \mathbf{r}')$, which describes the effect of the presence of an electron at the point $\mathbf{r}$ diminish the total density of the other electrons at the point $\mathbf{r}'$ and the linear response function $\chi(\mathbf{r}, \mathbf{r}', \omega)$. It describes the change of the total density at point $\mathbf{r}$ due to the perturbing potential at the point $\mathbf{r}'$ with frequency ω.

These quantities are physical and easily visible even for large systems. Their understanding provides a transparent and complementary insight into the nature of multiparticle systems.

The second advantage of DFT is the practicality of this approach. Traditional multiparticle wave function methods are restricted to a certain number of atoms (e.g. $N \approx 10$ for systems without symmetries). Therefore for problems where the consideration of much more interacting atoms is necessary, they are not applicable and alternative approaches are required. DFT fills this gap, because with this approach much more atoms ($N = O(10^2) - O(10^3)$) can be handled.

There are a few steps which lead to the formulation of the DFT. The first one is the lemma of Hohenberg and Kohn[1] which says that the ground state density $n(\mathbf{r})$ of an electronic system in an external potential $v(\mathbf{r})$ is uniquely determined. In other words the system is determined by the knowledge of the ground state density. Let us verify the Hohenberg-Kohn Theorem for a non-degenerate ground state: We start with the assumption that the $n(\mathbf{r})$ is the density in a potential $v_1(\mathbf{r})$, with the corresponding ground state ψ_1 and ground state energy E_1. The ground state energy is then defined as

$$E_1 = \langle \psi_1 | H_1 | \psi_1 \rangle = \int v_1(\mathbf{r}) n(\mathbf{r}) d\mathbf{r} + \langle \psi_1 | T + U | \psi_1 \rangle, \tag{3.75}$$

with H_1 as the total Hamiltonian and T the kinetic energy operator and U the potential energy operator. Here we will proceed with a second assumption for the existence of a second external potential $v_2(\mathbf{r})$ not equal to $v_1(\mathbf{r}) + const$ with the same ground state

density $n(\mathbf{r})$. For this case the ground state energy is defined as

$$E_2 = \langle\psi_2|H_2|\psi_2\rangle = \int v_2(\mathbf{r})n(\mathbf{r})d\mathbf{r} + \langle\psi_2|T+U|\psi_2\rangle, \tag{3.76}$$

which results in a different Hamiltonian H_2 due to external potential v_2. Here we can make use of the Rayleigh-Ritz principle, which says that the total energy E_0 of a system in ground state $|\psi_0\rangle$ is smaller than the expectation value for the arbitrary states $|\psi\rangle$

$$E_0 < \langle\psi|H|\psi\rangle. \tag{3.77}$$

Hence we get the following relations

$$E_1 < \langle\psi_2|H_1|\psi_2\rangle = \int v_1(\mathbf{r})n(\mathbf{r})d\mathbf{r} + \langle\psi_2|T+U|\psi_2\rangle, \tag{3.78}$$

$$E_2 < \langle\psi_1|H_2|\psi_1\rangle = \int v_2(\mathbf{r})n(\mathbf{r})d\mathbf{r} + \langle\psi_1|T+U|\psi_1\rangle. \tag{3.79}$$

These two inequalities can be rewritten by adding and subtracting the term with external potential

$$E_1 < E_2 + \int (v_1(\mathbf{r}) - v_2(\mathbf{r}))n(\mathbf{r})d\mathbf{r}, \tag{3.80}$$

$$E_2 < E_1 + \int (v_2(\mathbf{r}) - v_1(\mathbf{r}))n(\mathbf{r})d\mathbf{r}. \tag{3.81}$$

We can add these to inequalities and get

$$E_2 + E_2 < E_1 + E_2, \tag{3.82}$$

which leads to a contradiction of our assumption. This contradiction shows that, there exist no second external potential which leads to the same ground state density. Through this proof we have seen that the density $n(\mathbf{r})$ determines the external potential $v(\mathbf{r})$. Consequently it gives the total Hamiltonian H and implicitly all quantities which are obtained by the solution of many body Schrödinger equation. For the determination of the ground state density Hohenberg-Kohn minimal principle is used. In contrast to the Rayleigh Ritz minimal principle

$$E_0 = min\left(\langle\tilde{\psi}|H|\tilde{\psi}\rangle\right), \tag{3.83}$$

where the ground state energy is found by trial functions $|\tilde{\psi}\rangle$. Hohenberg-Kohn minimal principle is formulated in terms of trial densities $\tilde{n}(\mathbf{r})$, which correspond to trial functions

$\tilde{\psi}$. The minimization is done in two steps. The starting point is the energy functional $E_\nu[\tilde{n}(\mathbf{r})]$ with fixed density $\tilde{n}(\mathbf{r})$

$$\begin{aligned} E_\nu[\tilde{n}(\mathbf{r})] &= min_\alpha \left(\langle \tilde{\psi}^\alpha_{\tilde{n}} | H | \tilde{\psi}^\alpha_{\tilde{n}} \rangle \right) \\ &= \int v(\mathbf{r}) \tilde{n}(\mathbf{r}) d\mathbf{r} + F[\tilde{n}(\mathbf{r})], \end{aligned} \tag{3.84}$$

with

$$F[\tilde{n}(\mathbf{r})] = min \left(\langle \tilde{\psi}^\alpha_{\tilde{n}} | (T+U) | \tilde{\psi}^\alpha_{\tilde{n}} \rangle \right), \tag{3.85}$$

as a universal functional of density $\tilde{n}(\mathbf{r})$. The next step is the minimization of $E_\nu[\tilde{n}(\mathbf{r})]$ over all $\tilde{n}$.

$$E_\nu[\tilde{n}(\mathbf{r})] = min_{\tilde{n}(\mathbf{r})} E_\nu[\tilde{n}(\mathbf{r})]. \tag{3.86}$$

For the ground state the minimum is obtained, when $\tilde{n}(\mathbf{r})$ is the ground state density. Now we want to derive the self-consistent Kohn-Sham equations[2] for the description of the electronic structure using Hohenberg Kohn variational principle. In this case the energy functional for fixed density has the following form

$$\begin{aligned} E_\nu[\tilde{n}(\mathbf{r})] &= min_\alpha \left(\langle \tilde{\psi}^\alpha_{\tilde{n}} | H | \tilde{\psi}^\alpha_{\tilde{n}} \rangle \right) \\ &= \int v(\mathbf{r}) \tilde{n}(\mathbf{r}) d\mathbf{r} + F[\tilde{n}(\mathbf{r})] \\ &= \int v(\mathbf{r}) \tilde{n}(\mathbf{r}) d\mathbf{r} + T_S[\tilde{n}(\mathbf{r})] + \frac{1}{2} \int \frac{\tilde{n}(\mathbf{r}) \tilde{n}(\mathbf{r}')}{\mathbf{r} - \mathbf{r}'} d\mathbf{r} d\mathbf{r}' + E_{xc}[\tilde{n}(\mathbf{r})]. \end{aligned} \tag{3.87}$$

The second term $T_S[\tilde{n}(\mathbf{r})]$ is the kinetic energy functional for non-interacting electrons and the term $E_{xc}[\tilde{n}(\mathbf{r})]$ is the exchange correlation energy functional. The corresponding Euler Lagrange equations for a fixed number of electrons are

$$\delta E_\nu[\tilde{n}(\mathbf{r})] = \int \tilde{n}(\mathbf{r}) \left(v_{eff}(\mathbf{r}) + \frac{\delta}{\delta \tilde{n}(\mathbf{r})} T_S[\tilde{n}(\mathbf{r})]|_{\tilde{n}(\mathbf{r})=n(\mathbf{r})} - \epsilon \right) d\mathbf{r} = 0, \tag{3.88}$$

where

$$v_{eff}(\mathbf{r}) = v(\mathbf{r}) + \int \frac{n(\mathbf{r}')}{\mathbf{r} - \mathbf{r}'} d\mathbf{r}' + v_{xc}(\mathbf{r}), \tag{3.89}$$

and

$$v_{xc}(\mathbf{r}) = \frac{\delta}{\delta \tilde{n}(\mathbf{r})} E_{xc}[\tilde{n}(\mathbf{r})]|_{\tilde{n}(\mathbf{r})=n(\mathbf{r})}. \tag{3.90}$$

This equation looks like the equation for non-interacting particles moving in an effective external potential $v_{eff}(\mathbf{r})$. The condition of the minimization is fulfilled by the solution of the one-particle equation

$$\left(-\frac{1}{2} \nabla^2 + v_{eff}(\mathbf{r}) - \epsilon_j \right) \psi_j(\mathbf{r}) = 0, \tag{3.91}$$

$$n(\mathbf{r}) = \sum_{j=1}^{N} |\psi(\mathbf{r})|^2, \tag{3.92}$$

$$v_{eff}(\mathbf{r}) = v(\mathbf{r}) + \int \frac{n(\mathbf{r}')}{\mathbf{r} - \mathbf{r}'} d\mathbf{r}' + v_{xc}(\mathbf{r}). \tag{3.93}$$

These self-consistent equations are called Kohn-Sham equations. Through the solution of these equations the ground state density can be obtained, which would be used to calculate the ground state energy

$$E = \sum_{j=1}^{N} \epsilon_j + E_{xc}[n(\mathbf{r})] - \int v_{xc}(\mathbf{r}) n(\mathbf{r}) d\mathbf{r} - \frac{1}{2} \int \frac{n(\mathbf{r}) n(\mathbf{r}')}{\mathbf{r} - \mathbf{r}'} d\mathbf{r} d\mathbf{r}'. \tag{3.94}$$

If one omits the terms E_{xc} and v_{xc}, the self consistent Kohn-Sham equations would end up in the self consistent Hartree equations. So it is obvious that the many body effects are included in these terms, which are in general not known. One of the simplest but powerful approximations for these terms is the local density approximation (LDA)[1, 54, 55].

3.7.2 Practical application of DFT

There is still need of some approximation for the functionals $F[n(\mathbf{r})]$ in Hohenberg Kohn formulation and $E_{xc}[n(\mathbf{r})]$ in the Kohn Sham formulation. We start with a general expression for $E_{xc}[n(\mathbf{r})]$

$$E_{xc}[n(\mathbf{r})] = \int e_{xc}(\mathbf{r}; [n(\mathbf{r}')]) n(\mathbf{r}) d\mathbf{r}, \tag{3.95}$$

where $e_{xc}(r; [n(\mathbf{r}')])$ is a functional of density $n(\mathbf{r}')$ and exhibits the exchange correlation energy per particle at the position $\mathbf{r}$. We still do not have an explicit expression for $E_{xc}[n(\mathbf{r})]$, therefore in the next step we introduce the simplest approximation, the so called local density approximation

$$E_{xc}[n(\mathbf{r})] = \int e_{xc}(n(\mathbf{r})) n(\mathbf{r}) d\mathbf{r}, \tag{3.96}$$

where $e_{xc}(n)$ is the exchange correlation energy of a uniform electron gas of density n. This term is composed of a exchange part $e_x(n)$ and a correlation part $e_c(n)$

$$\begin{aligned} e_{xc}[n(\mathbf{r})] &= e_x(n) + e_c(n) \\ &= -\frac{0.458}{r_s} - \frac{0.44}{r_s + 7.8}. \end{aligned} \tag{3.97}$$

Obviously LDA is exact for a homogeneous electron gas, and it delivers good results for systems with slowly varying densities (at the scale of local Fermi wavelength λ_F). There are other approximative schemes for exchange correlation term $E_{xc}[n(\mathbf{r})]$ beyond LDA, which contain different versions of generalized gradient approximations (GGA), hybrid

methods, LDA+U[56] etc. After we have considered all of the ingredients of the DFT, we can write a sketch for the implementation for the DFT algorithm, which is drawn below. Here we can assume this algorithm has been implemented, and the so-called Kohn-Sham orbitals ψ_j and Kohn-Sham eigenvalues ϵ_j have been calculated. But still one has to consider their physical interpretation.

In Hartree Fock theory the eigenvalues represent the energy which is necessary to add or remove an electron from the an orbital. This interpretation is given by Koopman's theorem. In DFT there is an equivalent theorem the so-called Janak's theorem[57]

$$\frac{\partial E}{\partial n_j} = \epsilon_j, \tag{3.98}$$

which says that the highest occupied ϵ_f relative to the vacuum equals the ionization energy, but neither the Kohn-Sham orbitals ψ_j nor the energies ϵ_j have any strict physical meaning except the connection between the Kohn-Sham orbitals ψ_j and the physical density $n(\mathbf{r})$. Nevertheless it has been observed in many cases that the eigenvalues give a reasonable description of the physical band structure.

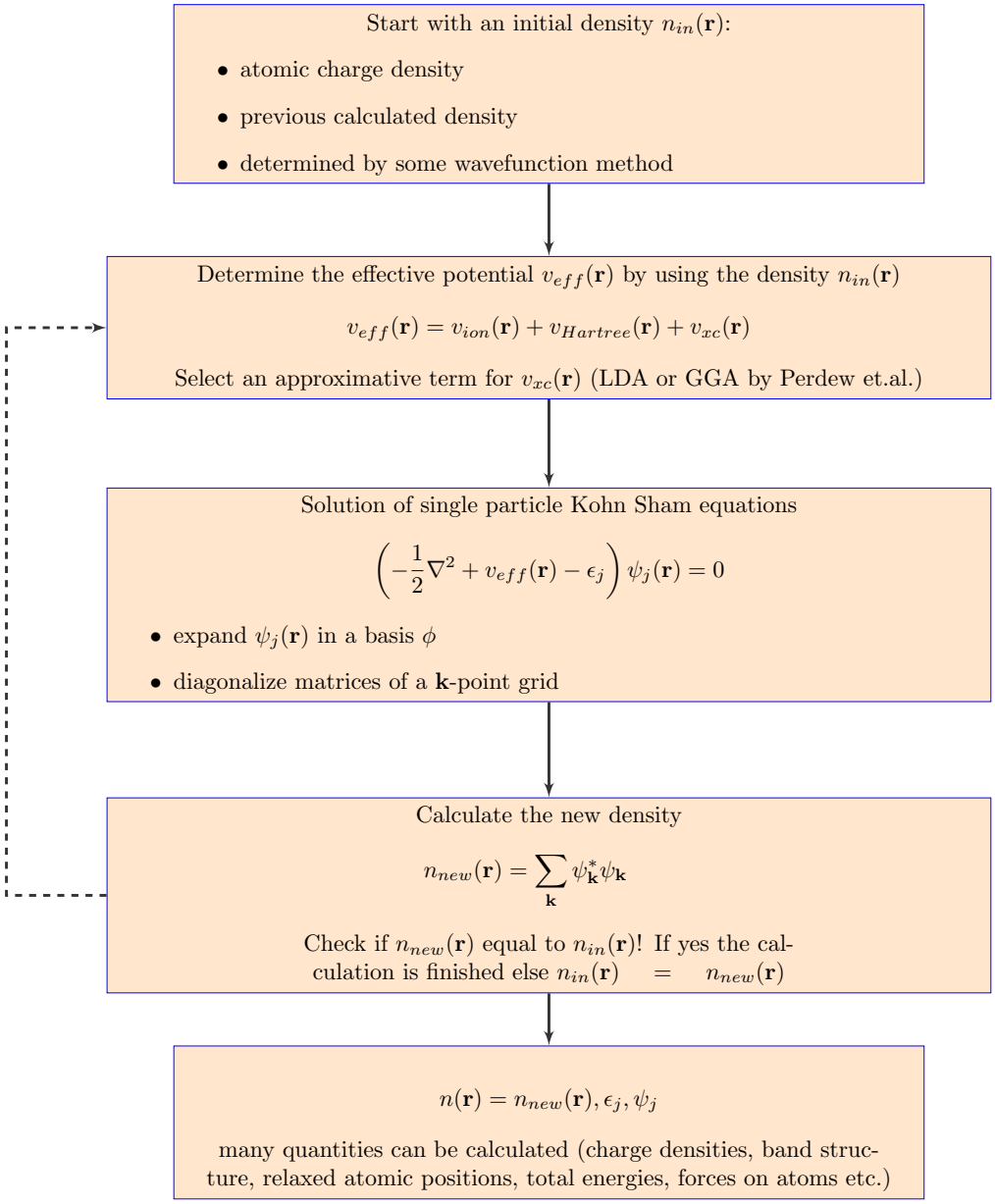
Start with an initial density $n_{in}(\mathbf{r})$:
• atomic charge density
• previous calculated density
• determined by some wavefunction method
Determine the effective potential $v_{eff}(\mathbf{r})$ by using the density $n_{in}(\mathbf{r})$
$v_{eff}(\mathbf{r}) = v_{ion}(\mathbf{r}) + v_{Hartree}(\mathbf{r}) + v_{xc}(\mathbf{r})$
Select an approximative term for $v_{xc}(\mathbf{r})$ (LDA or GGA by Perdew et.al.)
Solution of single particle Kohn Sham equations
$\left(-\frac{1}{2}\nabla^2 + v_{eff}(\mathbf{r}) - \epsilon_j\right)\psi_j(\mathbf{r}) = 0$
• expand $\psi_j(\mathbf{r})$ in a basis ϕ
• diagonalize matrices of a $\mathbf{k}$-point grid
Calculate the new density
$n_{new}(\mathbf{r}) = \sum_{\mathbf{k}} \psi^*_{\mathbf{k}}\psi_{\mathbf{k}}$
Check if $n_{new}(\mathbf{r})$ equal to $n_{in}(\mathbf{r})$! If yes the calculation is finished else $n_{in}(\mathbf{r}) = n_{new}(\mathbf{r})$
$n(\mathbf{r}) = n_{new}(\mathbf{r}), \epsilon_j, \psi_j$
many quantities can be calculated (charge densities, band structure, relaxed atomic positions, total energies, forces on atoms etc.)

3.7.3 Bloch functions and Wannier functions

In the last subchapter we gave an overview over density functional theory, which is also often referred as first principle calculations, because one is tackling the many body Schrödinger equation directly without any modeling. The Kohn-Sham equations are solved in terms of Bloch functions, they fulfill special properties which are required for the calculation of the electronic structure of periodic materials. Bloch functions $\psi_{n\mathbf{k}}(\mathbf{r})$ exhibit a band index n and a crystal momentum $\mathbf{k}$. The crystal electrons were described by Bloch functions and are named Bloch electrons. Bloch functions can be written as

$$\psi_{n\mathbf{k}}(\mathbf{r}) = \exp(i\mathbf{k}.\mathbf{r})u_{n\mathbf{k}}(\mathbf{r}). \tag{3.99}$$

If we set $u_{n\mathbf{k}}(\mathbf{r})$ to a constant value we will end up with the eigenfunctions of free particles or electrons. The periodic lattice potential modulates the plane wave by a term $u_{n\mathbf{k}}(\mathbf{r})$, which has the lattice periodicity. If we insert the Bloch functions into the eigenvalue equation we see that the eigenvalues E_n depend on $\mathbf{k}$

$$E_n = E_n(\mathbf{k}). \tag{3.100}$$

Because of

$$\psi_{n,\mathbf{k}}(\mathbf{r}) = \psi_{n,\mathbf{k}+\mathbf{K_m}}(\mathbf{r}), \tag{3.101}$$

it is sufficient to know the solutions of Schrödinger equation and the corresponding $E_n(\mathbf{k})$ in terms of $\mathbf{k}$ in the first Brillouin zone (Wigner Seitz cell in the $\mathbf{k}$-space). The function $E_n(\mathbf{k})$ gives for every fixed $\mathbf{k}$ value a discrete energy spectrum ($n = 1, 2, ...$), which represents the energy bands. The complete $E_n(\mathbf{k})$ is referred to as the band structure.

Alternatively for the electronic structure calculations instead of extended Bloch functions spatially localized Wannier functions can be used. We can use the relation, which says that the Bloch functions are periodic in $\mathbf{k}$-space to rewrite the Bloch functions as a Fourier series

$$\psi_{n,\mathbf{k}} = \frac{1}{\sqrt{N}} \sum_m w_n(\mathbf{R_m}, \mathbf{r}) \exp(i\mathbf{k}.\mathbf{R_m}). \tag{3.102}$$

The terms $w_n(\mathbf{R_m}, \mathbf{r})$ in this expansion are identified as Wannier functions. We can invert this equation to find an expression for Wannier functions

$$\begin{aligned} w_n(\mathbf{R_m}, \mathbf{r}) &= \frac{1}{\sqrt{N}} \sum_k \exp(-i\mathbf{k}.\mathbf{R_m})\psi_{n,\mathbf{k}}(\mathbf{r}) \\ &= \frac{1}{\sqrt{N}} \sum_{\mathbf{k}} \exp(i\mathbf{k}.(\mathbf{r} - \mathbf{R_m}))u_{n\mathbf{k}}(\mathbf{r}). \end{aligned} \tag{3.103}$$

The summation is over all $\mathbf{k}$ vector values in the first Brillouin zone. Let us consider some properties of Wannier functions. The Wannier functions depend only on the difference $w_n(\mathbf{r} - \mathbf{R_m})$, therefore they are centered on the midpoint of a Wigner-Seitz cell. For different bands n and different primitive translations $\mathbf{R_m}$ they are orthogonal

$$\begin{aligned}\int w_n^*(\mathbf{R}_m - \mathbf{r}) w_{n'}(\mathbf{R}'_m - \mathbf{r}) d\mathbf{r} &= \frac{1}{N}\sum_{\mathbf{k},\mathbf{k}'} \exp(i(\mathbf{k}.\mathbf{R}_m - \mathbf{k}'.\mathbf{R}_{m'})) \int \psi^*_{n,\mathbf{k}}(\mathbf{r})\psi_{n',\mathbf{k}'}(\mathbf{k}) d\mathbf{r} \\ &= \frac{1}{N}\sum_{\mathbf{k},\mathbf{k}'} \exp(i(\mathbf{k}.\mathbf{R}_m - \mathbf{k}'.\mathbf{R}_{m'}))\delta_{n,n'} \\ &= \delta_{m,m'}\delta_{n,n'}. \end{aligned} \tag{3.104}$$

Wannier functions with their special properties are very useful in some cases for characterizing the special properties of solids. There is no unique way how to construct the Wannier functions because of the arbitrariness of the phases of Bloch functions. To demonstrate this in a better way, let us consider the effect of a gauge transformation on the lattice periodic part of the Bloch functions

$$u_{n\mathbf{k}}(\mathbf{r}) \longrightarrow e^{i\phi_n(\mathbf{k})} u_{n\mathbf{k}}(\mathbf{r}), \tag{3.105}$$

on the Wannier functions. This phase does not change the overall phases of the Wannier functions but their shape and spatial extent will be effected. If we have not a simple isolated band but a set of isolated bands then the gauge transformation would look like

$$u_{n\mathbf{k}}(\mathbf{r}) \longrightarrow \sum_{m=1}^{N} U^{(\mathbf{k})}_{mn} u_{n\mathbf{k}}(\mathbf{r}), \tag{3.106}$$

where $U^{(\mathbf{k})}_{mn}$ are unitary matrices which mix the bands at wave vector $\mathbf{k}$. We can now use this expression to write a generalized form of Wannier functions

$$w_n(\mathbf{R} - \mathbf{r}) = \frac{V}{(2\pi)^3}\int_{BZ}\left(\sum_m U^{(\mathbf{k})}_{mn} u_{n\mathbf{k}}(\mathbf{r})\right)\exp(i\mathbf{k}.\mathbf{r})d\mathbf{k}. \tag{3.107}$$

The gauge transformation U can be utilized to construct optimized Wannier functions.

3.7.4 Maximally localized Wannier functions

The arbitrariness in the phases of Bloch functions can be used to construct maximally localized Wannier functions[58, 59]. For this purpose the phases in the expression (3.107) have to be fixed, which is done by a delocalization or spread functional defined as

$$\begin{aligned}\Omega_{deloc} &= \sum_n \left(\langle w_n(0)|r^2|w_n(0)\rangle - \langle w_n(0)|\mathbf{r}|w_n(0)\rangle^2\right) \\ &= \sum_{n=1}^{N}\left(\langle r^2\rangle_n - \langle \mathbf{r}\rangle_n^2\right), \end{aligned} \tag{3.108}$$

where the sum is over a set of bands and

$$\langle \mathbf{r}\rangle_n = \int r|w_n(\mathbf{R} - \mathbf{r})|^2 dr. \tag{3.109}$$

This functional can be seen as a measure for the spread of the Wannier functions. The aim here is to find values for the phases $U_{mn}^{(\mathbf{k})}$, that minimize this functional. The procedure of finding maximally localized Wannier functions works in the following way. The starting point is a set of Bloch functions $\psi_{n\mathbf{k}}(\mathbf{r})$, which are discretized on a mesh of $\mathbf{k}$ points. The explicit expression for the delocalization functional in terms of overlaps between Bloch functions

$$M_{m,n}^{(\mathbf{k},\mathbf{h})} = \langle u_{m\mathbf{k}} | u_{n,\mathbf{k}+\mathbf{h}} \rangle \tag{3.110}$$

can be derived (AppendixB), where h corresponds to vectors which are connecting neighboring mesh points. The aim is to find the unitary matrices $U_{mn}^{(\mathbf{k})}$ in equation (3.107) with the condition that the value of the delocalization functional Ω_{deloc} is minimized. So we have to calculate the gradient of delocalization functional

$$\nabla\Omega_{decol} = \frac{d\Omega_{decol}}{dW}, \tag{3.111}$$

with respect to an infinitesimal unitary rotation of a set of Bloch functions

$$|u_{n\mathbf{k}}\rangle = |u_{n\mathbf{k}}\rangle + \sum_m dW_{mn}^{(\mathbf{k})} |u_{m\mathbf{k}}\rangle, \tag{3.112}$$

where $dW_{mn}^{(\mathbf{k})}$ is a infinitesimal antiunitary matrix i.e. $dW^\dagger = -dW$ such that

$$U_{mn}^{(\mathbf{k})} = \delta_{mn} + dW_{mn}^{(\mathbf{k})}. \tag{3.113}$$

Through this steps we get an equation of motion for the evolution of the unitary matrices $U_{mn}^{(\mathbf{k})}$ and Wannier functions towards the minimum of the delocalization functional until the minimum is reached.

3.7.5 Construction of the model-Hamiltonian

As mentioned in section 2.2 strongly correlated materials can not be dealt with by ab-initio methods. There is a large discrepancy which arise from strong effective electron-electron interaction[60]. In the recent years ab-initio calculations combined with many body techniques produced many results which are in good agreement with the empirical ARPES measurements. An example for such a success story is LDA+DMFT. Here minimal low energy models, which deal with the conduction bands, are constructed. These are used to include the electronic correlations adequately[61, 17, 62, 63], but it implicates that there is still much effort for similar applications necessary.

Variational cluster approximation as a powerful many body technique can be also utilized for such an approach. To use the variational cluster approximation for correlated materials one needs a Hamiltonian which contains the multi-orbital character of the real materials. Therefore we will spend some time on the construction of such a Hamiltonian. The multi-orbital Hamiltonian which we want to construct consists of many parts, where

each part is physically motivated. The first part is equivalent to the hopping part of a single band Hubbard model.

$$H_{wan} = \sum_{i,j} t^{i,j}_{m,n} c^{\dagger}_{i\alpha\sigma} c_{j\beta\sigma}, \tag{3.114}$$

and corresponds to the kinetic energy of the system of interest. This part is completely delocalized and is obtained by density functional theory. From the Bloch basis a Wannier basis is constructed through an unitary transformation. At the end we get the kinetic part of our Hamiltonian in the Wannier basis.

The second part of the Hamiltonian is the interaction, which is given by

$$H_{int} = \frac{1}{2} \sum_{i,\alpha\beta\gamma\delta,\sigma\sigma'} U_{\alpha\beta\gamma\delta} c^{\dagger}_{i\alpha\sigma} c^{\dagger}_{i\beta\sigma'} c_{i\delta\sigma'} c_{i\gamma\sigma}. \tag{3.115}$$

Choosing as basis states spherical harmonics Y_L we can write:

$$\begin{aligned} H_{int} &= \sum_{L_i,m,\sigma\sigma'} \sum_{k=0}^{2l} \frac{4\pi F^k_l}{2k+1} \langle Y_{L_a} \mid Y_{km} \mid Y_{Lc} \rangle \\ &\times \langle Y_{L_d} \mid Y_{km} \mid Y_{Lb} \rangle c^{\dagger}_{L_a\sigma} c^{\dagger}_{L_b\sigma'} c_{L_d\sigma'} c_{L_c\sigma}, \end{aligned}$$

where F^k are Slater integrals.

$F^0 = U$ is the usual Hubbard U commonly calculated by constrained LDA, while the rest of Slater integrals are computed using atomic physics. One can give also some relations between the Slater integrals

$$J = \frac{(F^2 + F^4)}{14}, \tag{3.116}$$

$$\frac{F^2}{F^4} \approx 0.625 [64, 65]. \tag{3.117}$$

At this point it is quite useful to do a table for values of Slater integrals F^k calculated from atomic orbitals

1. p-electrons : $F^0 = U$, $F^2 = 5J$
2. d-electrons : $F^0 = U$, $F^2 = \frac{14}{1+0.625} J$, $F^4 = 0.625 F^2$
3. f-electrons : $F^0 = U$, $F^2 = \frac{6435}{286+195\times0.668+250\times0.494} J$, $F^4 = 0.668 F^2$, and $F^6 = 0.494 F^2$

Let us go on with our analysis of the interaction part. Assume that we are only interested in the local part of the interaction, i.e., density-density part. Then we can consider which assumptions are necessary to get only local part. Two conditions have to be satisfied:

1. $\alpha = \delta$ and $\beta = \gamma$ and $\sigma = \sigma' \Rightarrow U_{\alpha\beta\beta\alpha}$
2. $\alpha = \gamma$ and $\beta = \delta \Rightarrow U_{\alpha\beta\alpha\beta}$

Using these conditions we can calculate an expression for the local part of the interaction

1) $\sigma \neq \sigma'$:

$$\frac{1}{2} \sum_{i,\alpha\beta,\sigma\neq\sigma'} U_{\alpha\beta\alpha\beta} c^\dagger_{i\alpha\sigma} c^\dagger_{i\beta\sigma'} c_{i\beta\sigma'} c_{i\alpha\sigma} = \frac{1}{2} \sum_{i,\alpha\beta,\sigma\neq\sigma'} U_{\alpha\beta\alpha\beta} n_{i\alpha\sigma} n_{i\beta\sigma'}$$

2) $\sigma = \sigma'$:

$$\begin{aligned} &\frac{1}{2} \sum_{i,\alpha\beta,\sigma=\sigma'} U_{\alpha\beta\alpha\beta} c^\dagger_{i\alpha\sigma} c^\dagger_{i\beta\sigma'} c_{i\beta\sigma'} c_{i\alpha\sigma} \\ &+\frac{1}{2} \sum_{i,\alpha\beta,\sigma=\sigma'} U_{\alpha\beta\beta\alpha} c^\dagger_{i\alpha\sigma} c^\dagger_{i\beta\sigma'} c_{i\alpha\sigma'} c_{i\beta\sigma} \\ &= \frac{1}{2} \sum_{i,\alpha\beta,\sigma=\sigma'} \left(U_{\alpha\beta\alpha\beta} - U_{\alpha\beta\beta\alpha}\right) n_{i\alpha\sigma} n_{i\beta\sigma'} \end{aligned}$$

So we can now write the whole local interaction Hamiltonian as

$$\begin{aligned} H_{loc.int.} &= \frac{1}{2} \sum_{i,\alpha\beta,\sigma\neq\sigma'} U_{\alpha\beta\alpha\beta} n_{i\alpha\sigma} n_{i\beta\sigma'} \\ &+ \frac{1}{2} \sum_{i,\alpha\beta,\sigma=\sigma'} \left(U_{\alpha\beta\alpha\beta} - U_{\alpha\beta\beta\alpha}\right) n_{i\alpha\sigma} n_{i\beta\sigma'}. \end{aligned} \tag{3.118}$$

The parameters which are feeded into this Hamiltonian are the Hubbard U and the Hund's coupling J. The Hubbard U corresponds to the Coulomb interaction between two electrons on the same site. The meaning of the Hund's coupling in this context is not clear yet. Therefore some explanations are necessary.

In cases where only partially filled single bands are crossing the Fermi level, the ratio between the Hubbard U and bandwidth W are sufficient parameters for the description of many body effects. On the other side if many bands are crossing the Fermi level more parameters are necessary. Inter-orbital and intra-orbital interactions are differing, because of the distribution of the electrons between different orbitals. This distribution is not randomly but by Hund's rules, whose main statement is that electron distribution among different orbitals is done by minimizing the energy. That means that high spin states play a role[66]. The interaction strength of electrons changes, if the electrons occupy the same or different orbitals and it also depends on the electrons mutual spin alignment. A measure for this influence is the Hund's coupling J.

3.7.6 Sketch of the DFT+VCA scheme

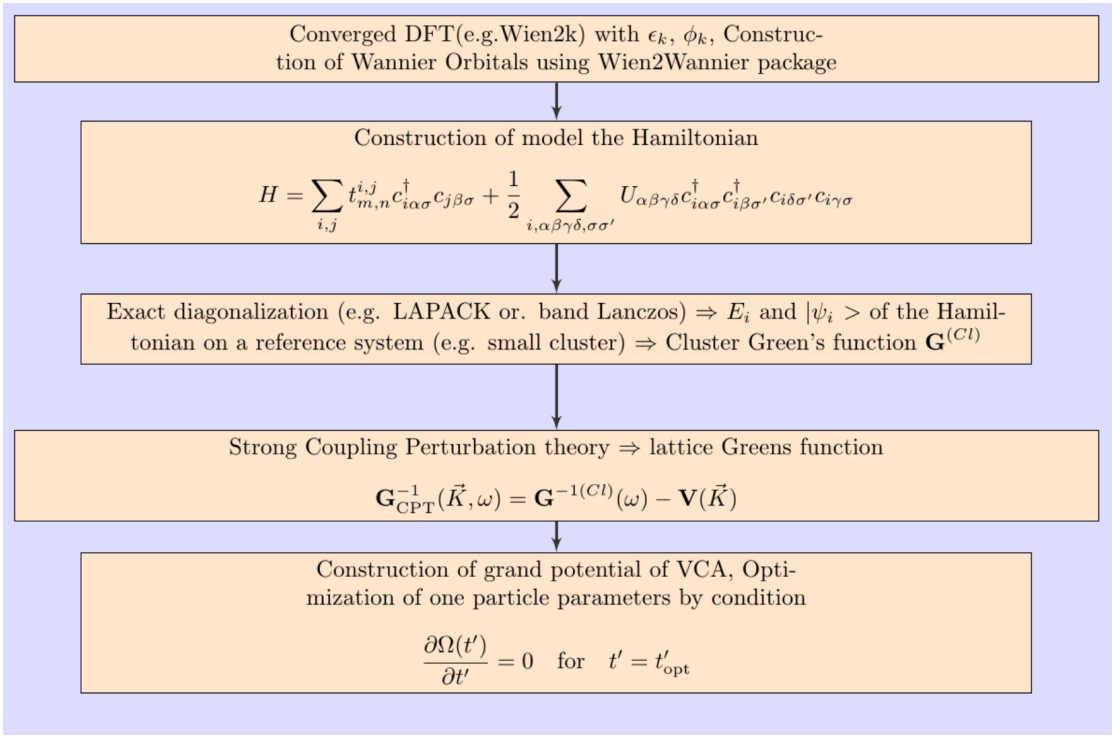

3.7.7 Parameters in the Model-Hamiltonian and Constrained RPA

In many applications the values of screened Coulomb interaction is taken as a parameter named Hubbard U. It can be viewed as the energy cost for moving an electron between two orbitals, e.g. in the following reaction

$$2(d^n) \rightarrow d^{n-1} + d^{n-1}, \tag{3.119}$$

U corresponds to the energy cost for moving a $3d$ electrons between two atoms, where both possess n $3d$ electrons. The parameter U should also contain the effect of screening by other orbitals, which in the case of $3d$ electrons are s or p electrons. There are some attempts to calculate the value of it from first principle calculations. One of this attempts is the so-called constrained local density approximation (cLDA) [67, 68], where the Hubbard U is obtained by the variation of the total energy with respect to the occupation number of localized orbitals. An alternative approach is the constrained random phase approximation (cRPA)[69]. It delivers the energy dependence of the interaction and all components of the interaction matrix simultaneously. Let us start

with the definition of the screened Coulomb interaction

$$W(\mathbf{r},\mathbf{r}',\omega) = \int V(\mathbf{r}-\mathbf{r}'')\epsilon^{-1}(\mathbf{r}'',\mathbf{r}',\omega)d\mathbf{r}'', \tag{3.120}$$

where $v(\mathbf{r}-\mathbf{r}'')$ is the bare Coulomb interaction and $\epsilon^{-1}(\mathbf{r}'',\mathbf{r}',\omega)$ is the inverse dielectric function, which gives the change of total Coulomb potential V, if an external perturbing field is applied. It can be written as the ratio of bare and screened Coulomb potential

$$\epsilon(\mathbf{r},\mathbf{r}',\omega) = \frac{V(\mathbf{r}-\mathbf{r}')}{W(\mathbf{r},\mathbf{r}',\omega)}. \tag{3.121}$$

The effective Coulomb interaction can be calculated by using the RPA, i.e., Feynman diagrams of the form shown in figure 3.8.

$$\begin{aligned} W &= V + W\cdot P\cdot V \\ &= (1-V\cdot P)^{-1}\,V. \end{aligned} \tag{3.122}$$

The term in the denominator is the famous dielectric function of the electron gas

$$\epsilon = 1 - V\cdot P. \tag{3.123}$$

The polarization function in the RPA is given by

$$\begin{aligned} P(\mathbf{r},\mathbf{r}',\omega) = \sum_{spin}\sum_{n,\mathbf{k}}^{occu}\sum_{n',\mathbf{k}'}^{unoccu} & \psi^*_{n\mathbf{k}}(\mathbf{r})\psi_{n'\mathbf{k}'}(\mathbf{r})\psi^*_{n'\mathbf{k}'}(\mathbf{r}')\psi_{n\mathbf{k}}(\mathbf{r}')\times \\ & \left(\frac{1}{\omega-\epsilon_{n\mathbf{k}'}+\epsilon_{n\mathbf{k}}+i\delta} - \frac{1}{\omega+\epsilon_{n'\mathbf{k}'}-\epsilon_{n\mathbf{k}}-i\delta}\right), \end{aligned} \tag{3.124}$$

where $\psi_{n\mathbf{k}}(\mathbf{r})$ are the Bloch eigenstates and the $\epsilon_{n\mathbf{k}}$ corresponding eigenvalues. Here all transitions between all bands are included. Within the constrained random phase approximation the polarization is divided into two terms, the so-called P_w, which accounts for polarization in a chosen energy window (e.g. $3d$ to $3d$ orbital transitions) and P_r for the rest of the polarization. The total polarization is the sum of both terms $P = P_\mathrm{w}+P_r$. Inserting this in the definition of the effective interaction we obtain

$$\begin{aligned} W &= (1-V\cdot P)^{-1}\,V \\ &= (1-V\cdot(P_\mathrm{w}+P_r))^{-1}\,V \\ &= (1-W_r\cdot P_\mathrm{w})^{-1}\,W_r, \end{aligned} \tag{3.125}$$

where $W_r = (1-V\cdot P_r)^{-1}\,V$ is the screened interaction which does not include the polarization of the selected energy window. The orbitals in the selected energy window screen the screened Coulomb interaction W_r further, which are represented by the polarization P_w between the orbitals in this window. The Wannier function on the position R_i $\{|\phi_{nR_i}\rangle\}$ can be exploited for the calculation of the matrix elements of the dynamical Coulomb interaction matrix

$$U_{nR_1n'R_2,mR_3m'R_4}(t-t') = \int d\mathbf{r}d\mathbf{r}'\phi^*_{nR_1}(\mathbf{r})\phi_{n'R_2}(\mathbf{r})W_r(\mathbf{r},\mathbf{r}',t-t')\phi^*_{mR_3}(\mathbf{r})\phi_{m'R_4}(\mathbf{r}).$$

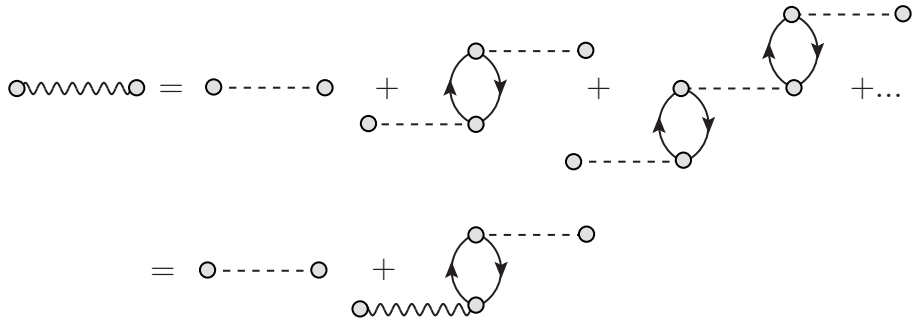

Figure 3.8: Calculation of the effective interaction within the random phase approximation (RPA). The loop which represents particle hole creation and annihilation process also called the polarization insertion is responsible for polarization effects of electron gas which comes from Coulomb interaction.

For the local case, i.e., Wannier orbitals at the position $R = 0$, this expression can be simplified to

$$U_{nn',mm'}(t-t') = \int d\mathbf{r}d\mathbf{r}'\phi_n^*(\mathbf{r})\phi_{n'}(\mathbf{r})W_r(\mathbf{r},\mathbf{r}',t-t')\phi_m^*(\mathbf{r})\phi_{m'}(\mathbf{r}).$$

From this the static interaction matrix $U_{nn';mm'}$ is obtained by performing the zero-frequency limit $U = W_r(\omega = 0)$.

4 A MEASURE OF THE NON-LOCALITY OF CORRELATIONS FOR THE HUBBARD MODEL

4.1 Introduction

In quantum cluster methods correlations are taken into within small clusters while long range correlations are either approximated in a perturbative or in a mean-field manner[70]. This kind of approximation is reflected in the momentum dependence of the self-energy, i.e., self-energy retains momentum dependence which differs from the limits where only local correlations survive and momentum dependence cancels out. Here we are going to postulate some kind of measure, which illustrates on the one hand the spatial evolution of the non-locality of the self-energy and on the other hand reflects the level of the approximation, when non-local terms of the self-energy are neglected. For this purpose we can define the following expression as a measure of the non-locality

$$\tilde{g}(\Delta) = \frac{1}{n}\sum_{i,j}\int_{-\infty}^{\infty} Im\Sigma_{ij}(\omega)d\omega\Big|_{|i-j|=\Delta}, \tag{4.1}$$

and then normalize it

$$g(\Delta) = \frac{\tilde{g}(\Delta)}{\tilde{g}(\Delta=0.0)}. \tag{4.2}$$

Now we can go straight forward and apply this expression to the Hubbard model. One of the milestones of DMFT is the prove of the locality of the self-energy in the infinite dimensional case[6]. Because of this fact dimensionality analysis in this area is an important issue, which should be considered. The main difference in the dimensionality of the Hubbard model in a cluster based approach, e.g., in the cluster perturbation theory (CPT), can be easily observed in the non-interacting limit, which is shown for the spectral function $A(\mathbf{k},\omega)$ and the corresponding density of states $\rho(\omega)$ in figure 4.1.

In the one-, two-, and three-dimensional Hubbard model the physics is completely different which is obviously apparent. There are Van-Hove singularities[71] at the edges of the Brillouin zone in the one-dimensional Hubbard model and a logarithmic singularity at the origin[72] in the two-dimensional case. There are some open questions at this point which we are interested in. How close is the three-dimensional case to the infinite dimensional case in the respect of the correlations? Is the two-dimensional case more

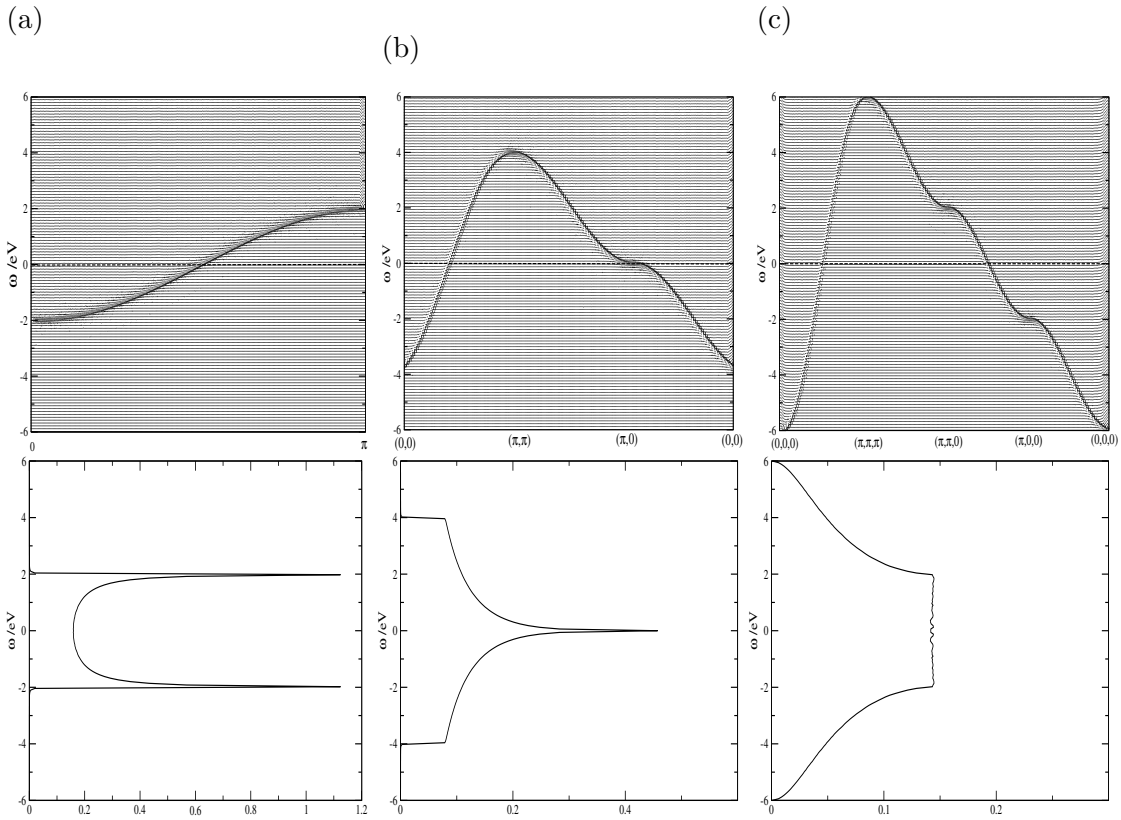

Figure 4.1: Comparison of the spectral function $A(\mathbf{k}, \omega)$ and density of states $\rho(\omega)$ of the Hubbard model for the non-interacting ($U = 0$) case: (a) one-dimensional Hubbard model; (b) two-dimensional Hubbard model; (c) three-dimensional Hubbard model. In the 1D case there are Van-Hove singularities[71] at the edges of the Brillouin zone. In the 2D case there is a logarithmic singularity at the origin[72].

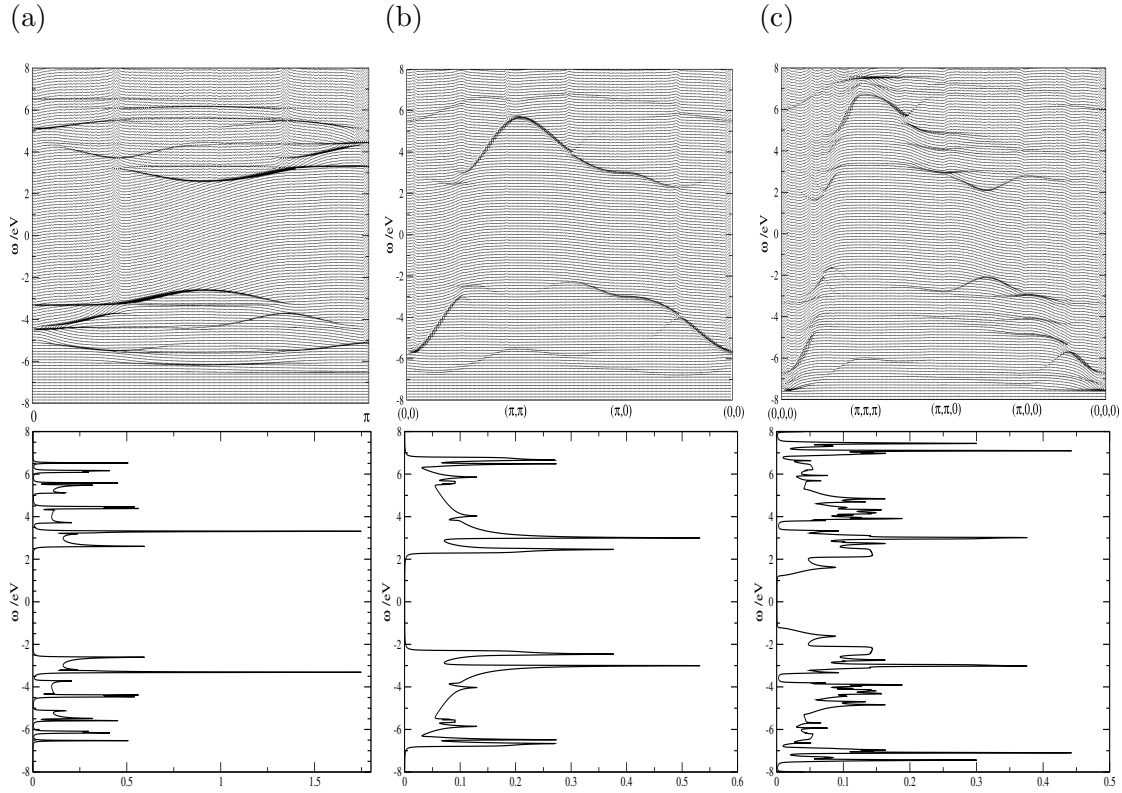

Figure 4.2: Comparison of the spectral function $A(\mathbf{k}, \omega)$ and density of states $\rho(\omega)$ of the Hubbard model for the interacting ($U = 8t$, $t = -1$) case at the half filling ($\mu = U/2$, $n = 1$): (a) one-dimensional Hubbard model; (b) two-dimensional Hubbard model; (c) three dimensional Hubbard model.

close to the one-dimensional case or to the three-dimensional case? Can one give some quantitative estimate for the spatial extend of correlations in this these cases? If one switches on the interaction a gap appears for a not so large interaction strength ($U = 8t$) in the cluster perturbation theory which is shown in figure 4.2. The gap size within this approach differs strongly within the dimensionality of the lattice, which can be potentially explained by the different spatial correlations. Using this we are going to apply the introduced measure 4.1 to investigate different cluster sizes regarding their non-local correlations and dimensionality.

4.2 One-dimensional Hubbard Model

The physics of the one-dimensional Hubbard model is very special and non-local correlations are in this case very important. For cluster perturbation theory implementation one has to chose a cluster tiling. The shape of the clusters in this case are unique as it is illustrated in figure 4.3. For these cluster tilings the spectral function $A(\mathbf{k}, \omega)$ and

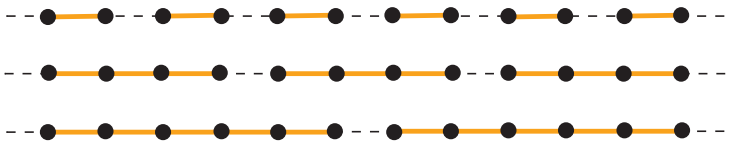

Figure 4.3: Possible one-dimensional cluster tilings with differing cluster sizes: 2×1 clusters, 4×1 clusters, 6×1 clusters.

the corresponding density of states $\rho(\omega)$ can be calculated and this is demonstrated in figure 4.4.

The increase in the cluster size gives a broadening in the spectral function and a small decrease in the gap which comes from long range non-local correlations. We can use our measure defined above to consider the behaviour and the range of these spatial correlations.

First to check the validity of this measure we have to reproduce the atomic limit where only local correlations survive i.e. our measure should vanish in this limit. This criterion is fulfilled and is shown in figure 4.5, where for decreasing values of the hopping parameter t, our self-energy non-locality measure is vanishing faster.

After this verification we can consider the behaviour of this non-locality measure with increasing cluster sites. Within the limit of the exact diagonalization we can see in figure 4.6 (a) that a saturation or vanishing behaviour of our measure is not observed. But one can also use in the construction of this non-locality measure instead of imaginary part of self-energy, the real part of the self-energy which gives a saturating but not vanishing behaviour that can be observed in figure 4.6 (b).

A parameter study for the interaction strength values in the interval $[U = 0.0625t,\ U = 80t]$ of this non-locality measure gives very interesting results as shown in figure 4.7. Such an analysis is useful because we can on the one side study the evolution of the non-locality behaviour of the self-energy for the different parameters and on the other side it gives us a clue in which parameter regime our method works best. This is because of the fact that in these cluster methods only short range spatial correlations are respected.

Here we can summarize our results for the one-dimensional case. Our method is useful for small one particle parameter values t or small interaction parameter values. This is also very intuitive because of the exact limites of the cluster perturbation theory. In the medium parameter regime it shows a decreasing behaviour within the cluster spatial extension up to a point where the finite size perturbing effects coming from cluster border are changing this dramatically. For larger clusters this effects are pushed further away.

4.3 Two-dimensional Hubbard Model

Now we want to consider the evolution of the non-locality self-energy measure for the two dimensional Hubbard model. Therefore we will apply the same procedure as for the one dimensional case. Here the cluster shape is not unique and therefore one is forced to select

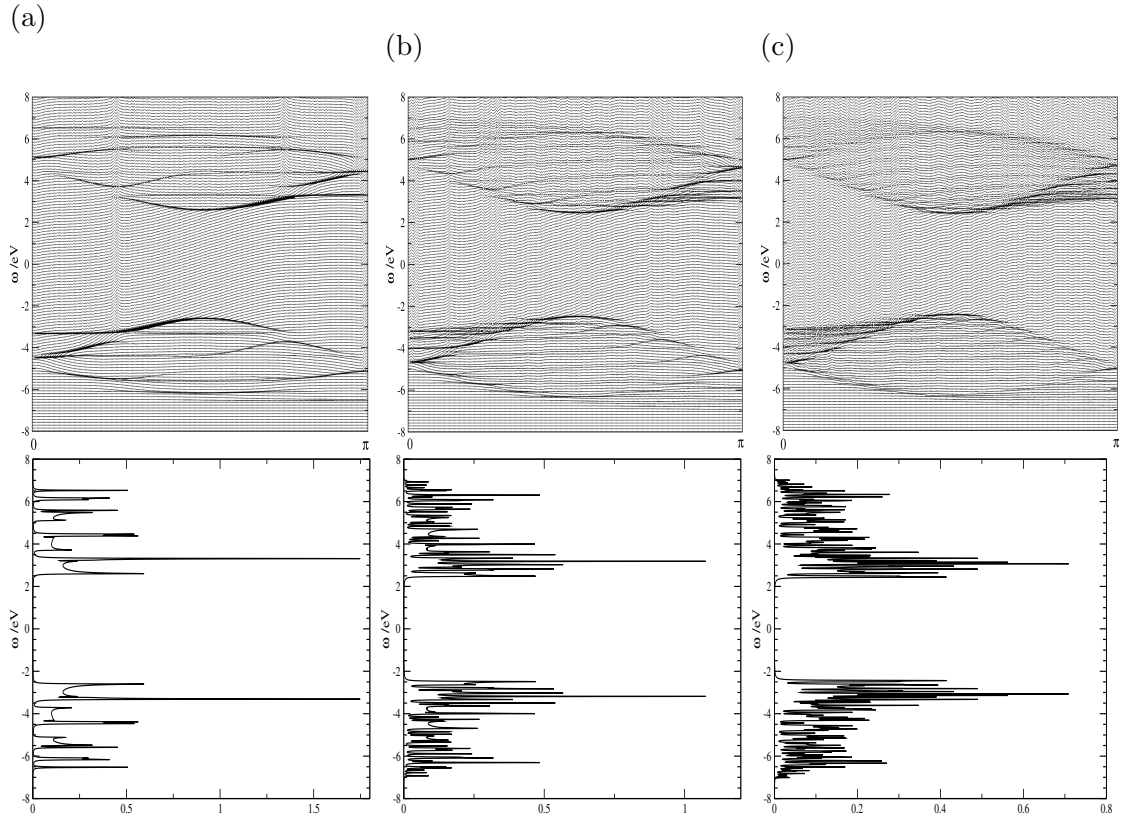

Figure 4.4: The evolution direction or the trend of the spectral function $A(\mathbf{k}, \omega)$ and the corresponding density of states $\rho(\omega)$ for the one-dimensional Hubbard model in the interacting ($U = 8t$, $t = -1$) case at the half filling ($\mu = U/2$, $n = 1$); used cluster tilings are: (a) 4×1; (b) 8×1; (c) 12×1.

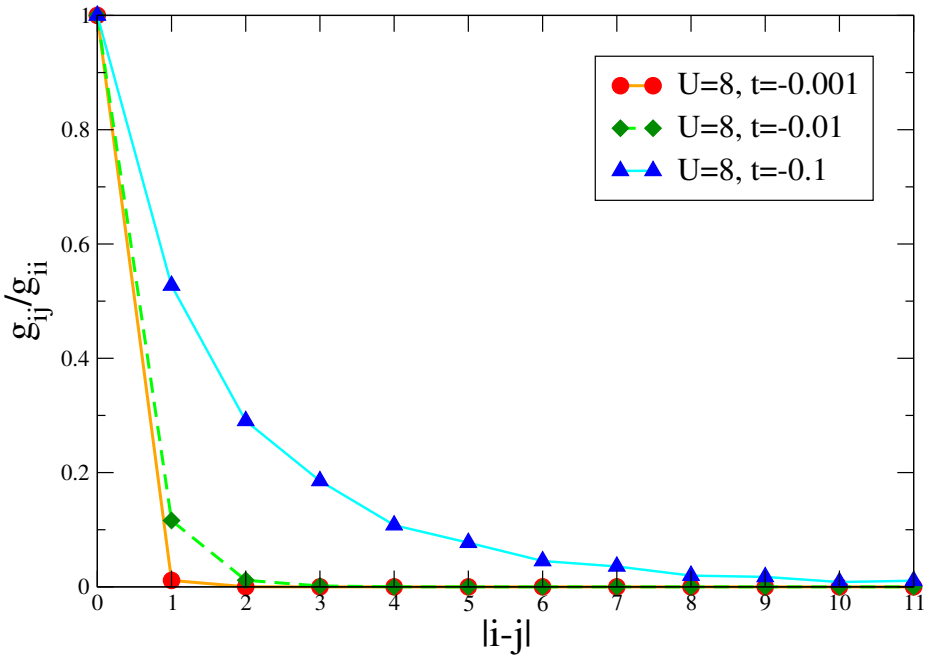

Figure 4.5: Normalized self-energy non-locality measure for the one-dimensional clusters with 12 sites for different values of the one particle parameter values t at the half filling ($\mu = U/2$, $n = 1$).

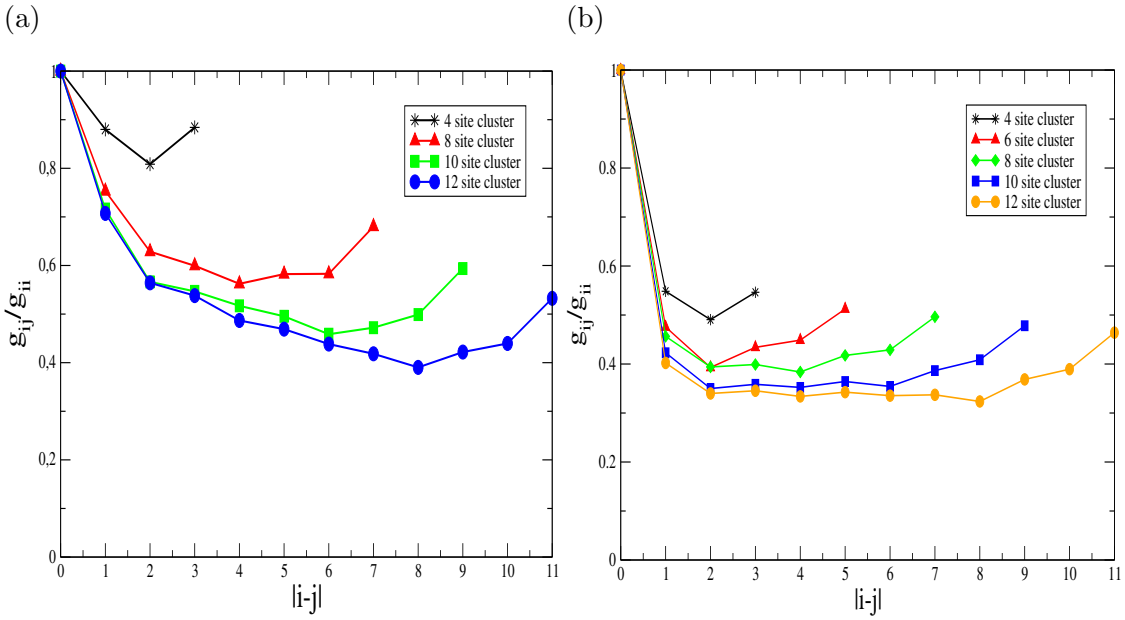

Figure 4.6: Normalized self-energy non-locality measure for different one-dimensional clusters and at the following parameter values: ($U = 8t$, $t = -1$) case at the half filling ($\mu = U/2$, $n = 1$); (a) imaginary part of self-energy used, (b) real part of self-energy used

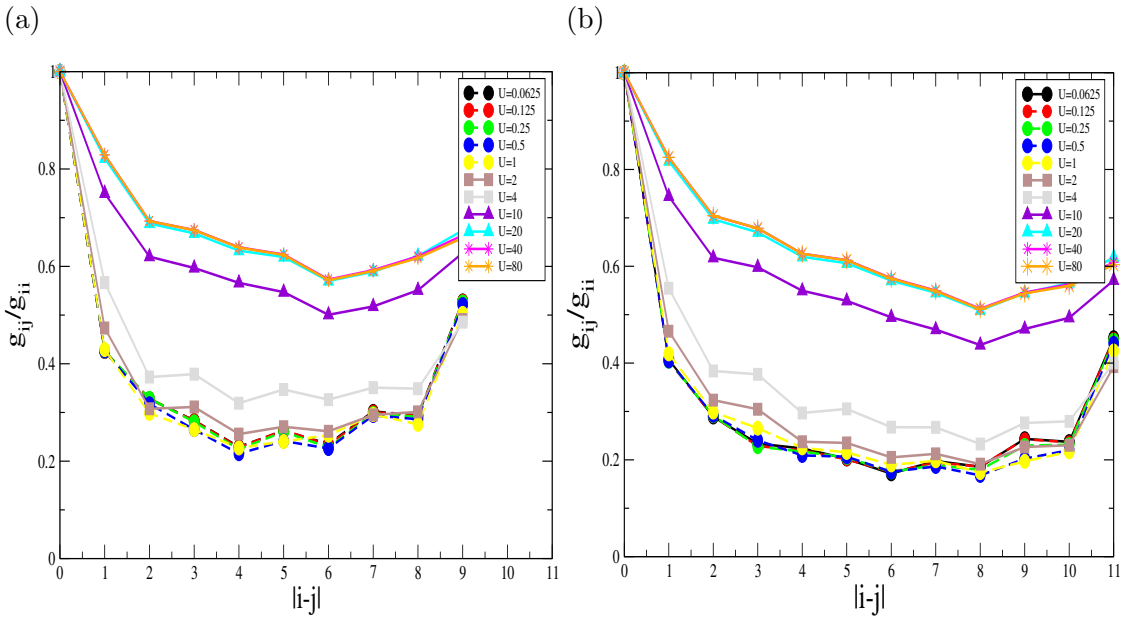

Figure 4.7: Normalized self-energy non-locality measure for different clusters and different values of interaction strength U, at the half filling ($\mu = U/2$, $n = 1$) : (a) 10 sites clusters, (b) 12 sites clusters.

some class of cluster tilings of the original lattice. Because of the exact diagonalization limitations we are constricted to small clusters. We choose for our analysis the following class of cluster tilings which are sketched in figure 4.8.

For these cluster tilings we can again calculate the spectral function $A(\mathbf{k}, \omega)$ and the corresponding density of states $\rho(\omega)$ of the two dimensional Hubbard model system. The obtained results are shown in the figure 4.9. For larger clusters again the spectral function is more spread out and the gap is reduced. Another development is that for the cluster tilings where the cluster shape extension in x and y axis direction are not equal we find is a larger reduce in the gap which is observed in the figures 4.9 (b), (d) and (h). This can be denoted as the cluster shape effect.

Again we can apply our non-locality self-energy measure to this problem. For the two-dimensional Hubbard model the spatial cluster extension is more restricted than for the one-dimensional case. Therefore there are strong fluctuations in our measure as it is demonstrated in Figure 4.10, but the trend is obviously in the direction of the more suppressed spatial correlations. These fluctuations in the measure come from the cluster shape geometry and from finite-size effects. Their effect is also visible in the spectral function and density of states calculations.

To minimize these strong fluctuations, we are going to do an averaging of the calculated values within the clusters with equal lattice sites. This procedure reduces the spatial fluctuations dramatically and gives us the results which is demonstrated in figure 4.11. In these results the cluster geometry, or rather the cluster shape effects, are reduced but still the finite size effects remain.

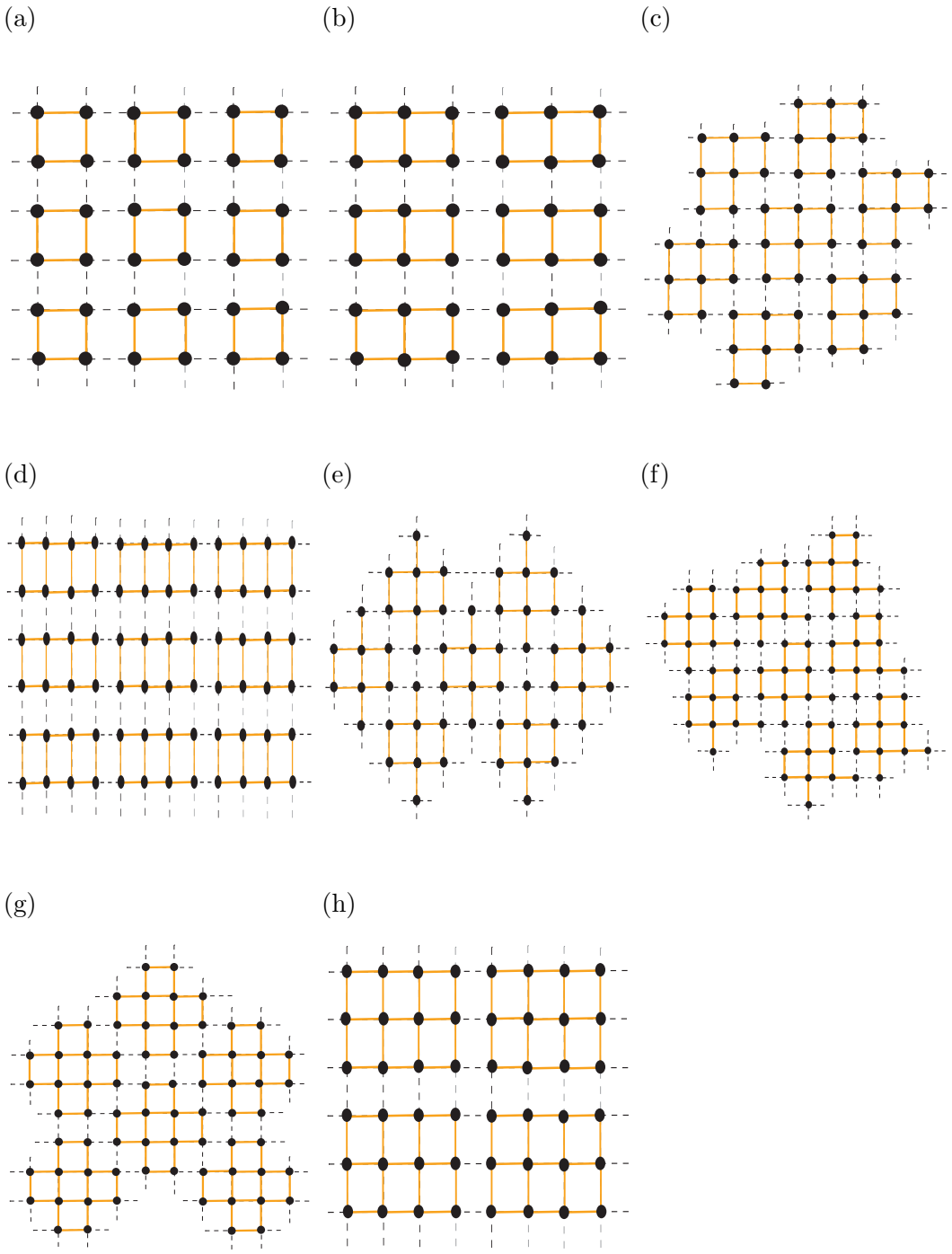

Figure 4.8: Two-dimensional clusters with differing cluster sites and cluster geometries: (a) 2×2 clusters, (b) 2×3 clusters, (c)-(e) different 8 site clusters with different shapes (f) 10 site clusters, (g)-(h) 12 site clusters with different shapes.

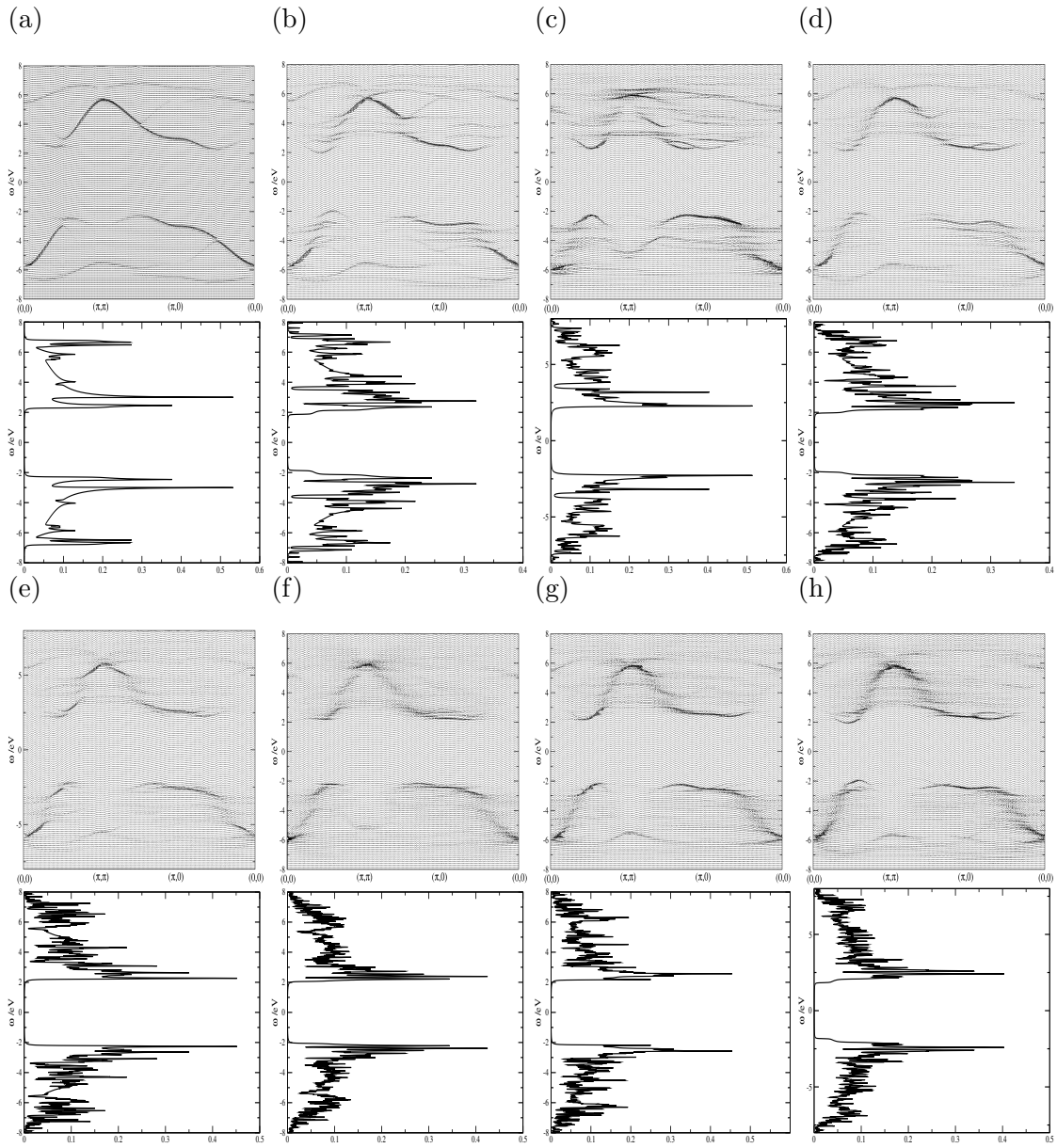

Figure 4.9: Comparison of the spectral function $A(\mathbf{k},\omega)$ and density of states $\rho(\omega)$ of the two-dimensional Hubbard model for the parameters ($U = 8t$, $t = -1$), at the half filling ($\mu = U/2$, $n = 1$) for different cluster tilings : (a) 2×2 clusters, (b) 2×3 clusters, (c)-(e) different 8 site clusters with different shape (f), 10 site clusters, (g)-(h) 12 site clusters with different shapes.

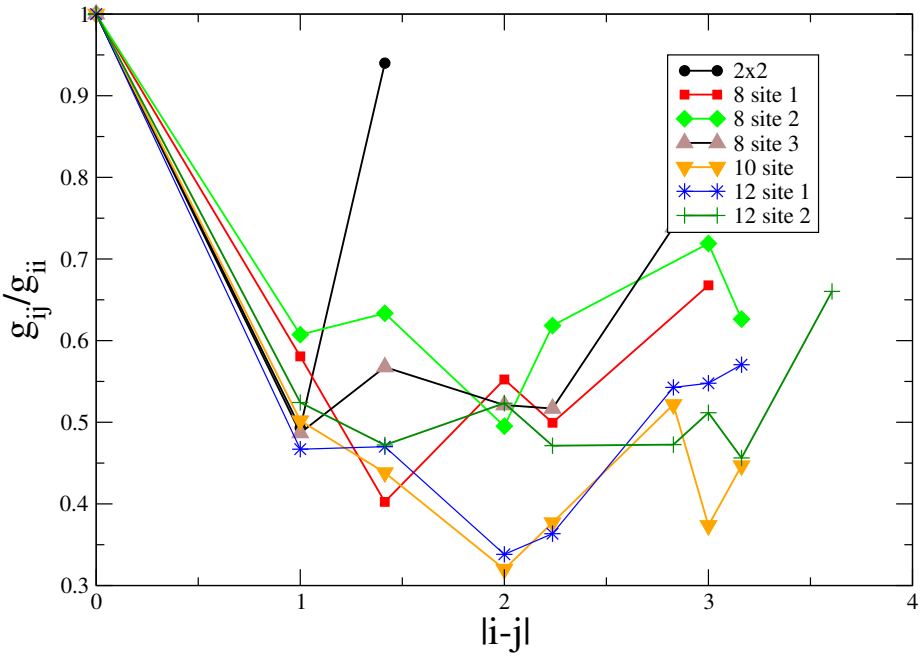

Figure 4.10: Spatial evolution of the normalized self-energy non-locality measure for different two dimensional clusters and at the following parameter values: ($U = 8t$, $t = -1$), Half filling ($\mu = U/2$, $n = 1$)

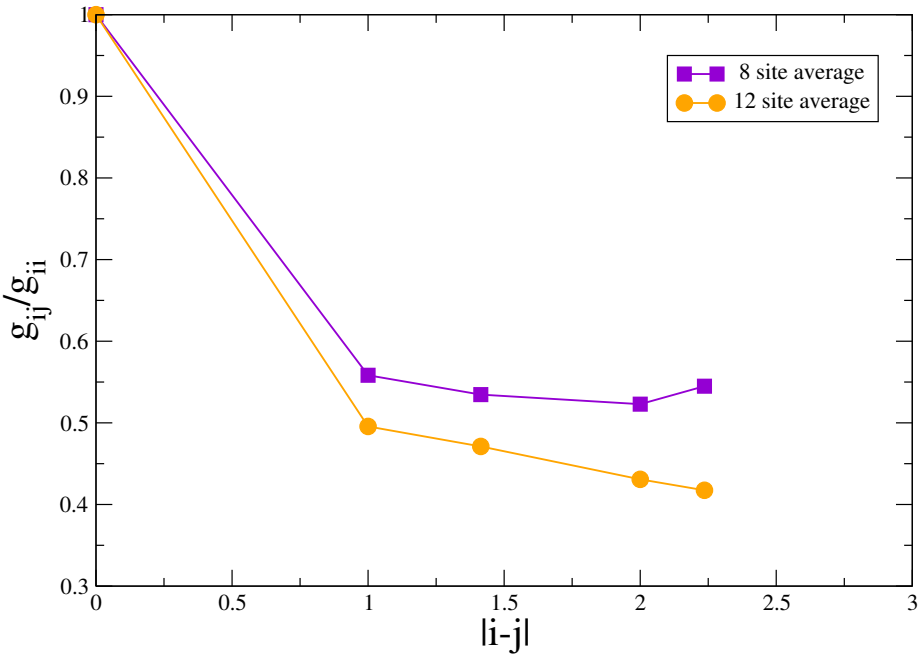

Figure 4.11: Averaged spatial evolution of the normalized self-energy non-locality measure for different two dimensional clusters and at the following parameter values: ($U = 8t$, $t = -1$), Half filling ($\mu = U/2$, $n = 1$). The average is done within clusters with the same lattice sites but different shapes

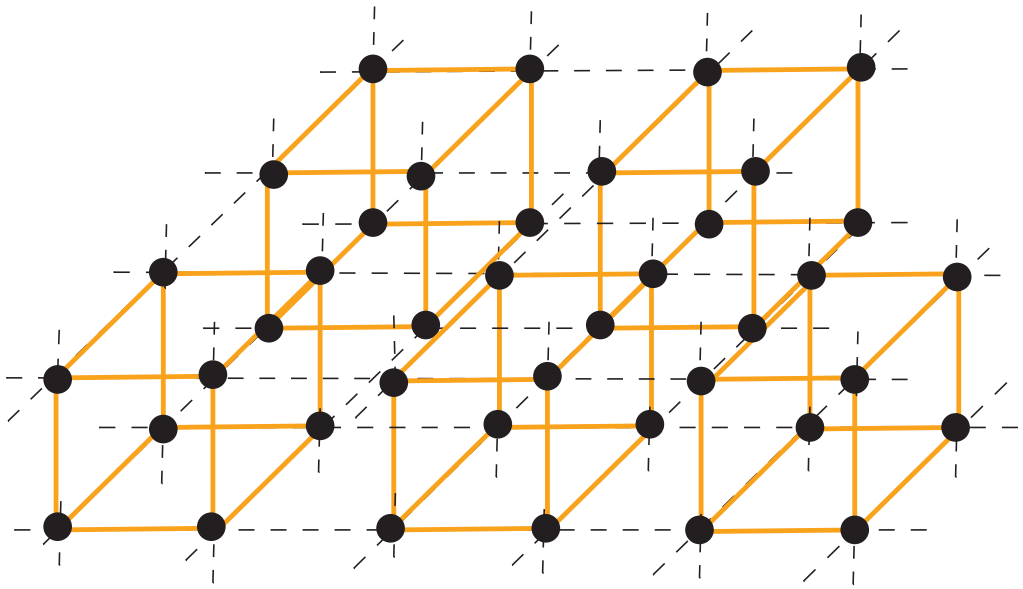

Figure 4.12: Three-dimensional 2×2×2 clusters.

4.4 Three-dimensional Hubbard Model

After the consideration of the one- and two-dimensional case it would be of great benefit to view evolution of our non-locality self-energy measure for the three-dimensional Hubbard model. For the three-dimensional case the possible cluster tilings are much more restricted. We can choose $2 \times 2 \times 2$ or $3 \times 2 \times 2$ cluster tilings as it is shown for the first case in figure 4.12.

After the consideration of the non interacting limit we have seen that there are major differences in all this cases. The differences also remain in the interacting case. Here the gap size is changing with the dimensionality which is observed in figure 4.13.

We can again consider the evolution of our non-locality self-energy measure and observe the fluctuative behaviour again which comes from the finite size effects and from cluster geometry. Here we can again say that the level of strongly suppressed correlations within the cluster extension is obtained but cluster geometry effects and finite size effects disturb the smoothness of the curves which can be seen in figure 4.14.

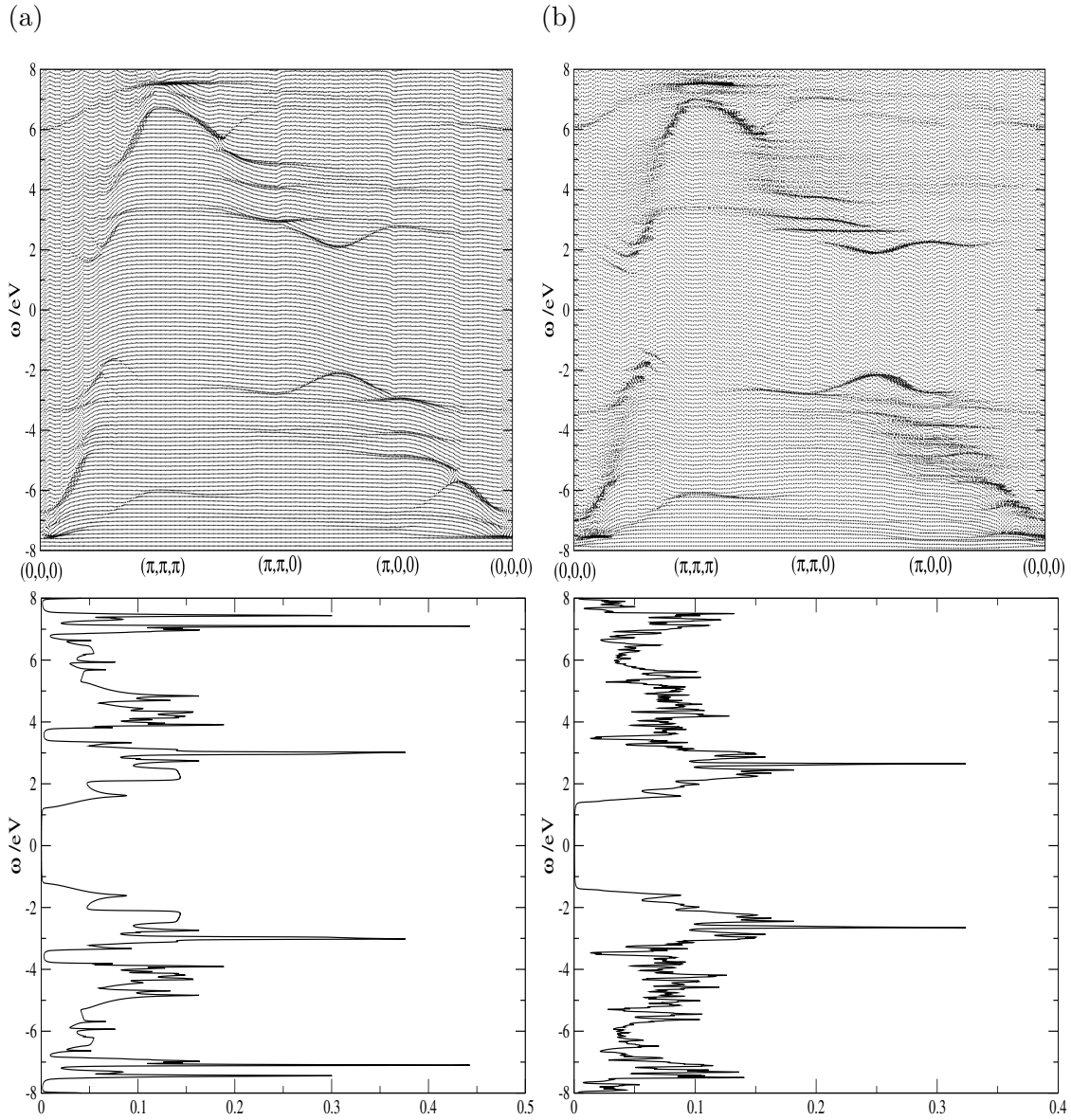

Figure 4.13: Comparison of the spectral function $A(\mathbf{k}, \omega)$ and density of states $\rho(\omega)$ in the three-dimensional Hubbard model for the interacting ($U = 8t$, $t = -1$) case at the half filling ($\mu = U/2$, $n = 1$): (a) cubic $2 \times 2 \times 2$ cluster tiling ; (b) $3 \times 2 \times 2$ cluster tiling.

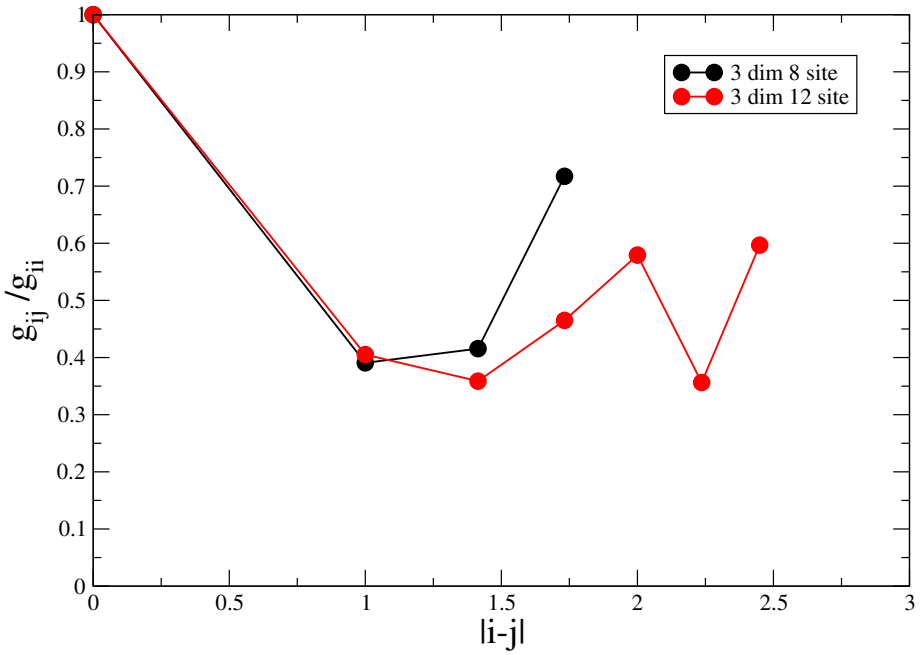

Figure 4.14: Spatial evolution of the normalized non-locality self-energy measure for different three dimensional clusters and at the following parameter values: ($U = 8t$, $t = -1$), at the half filling ($n = 1$, $\mu = U/2$); black curve: $2 \times 2 \times 2$ clusters, red curve; $3 \times 2 \times 2$ clusters.

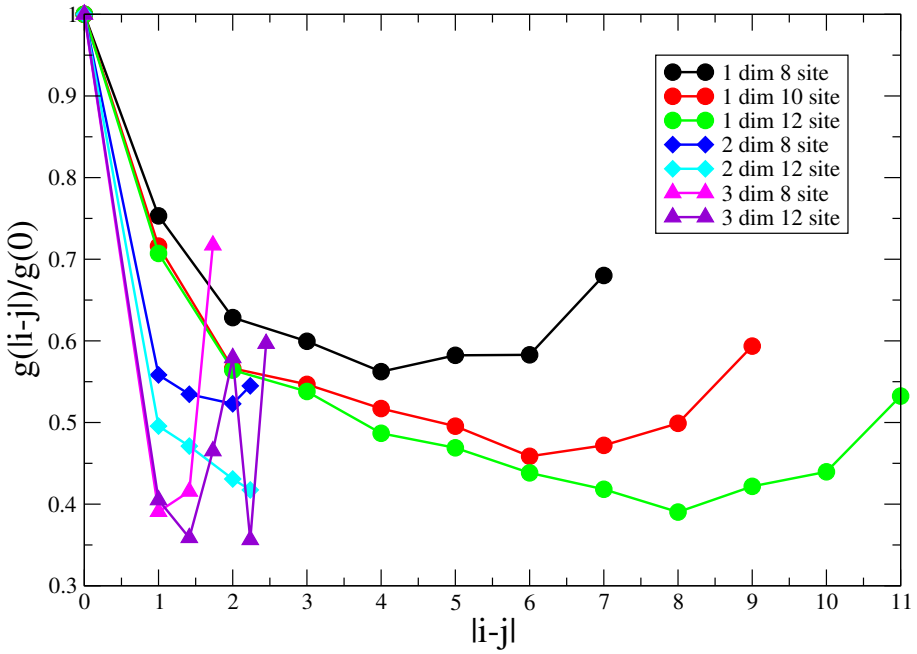

Figure 4.15: Spatial evolution of the normalized non-locality self-energy measure. Comparision of the one-, two-, three-dimensional clusters for the parameters: $U = 8t$, $\mu = U/2$, $t = -1$, $n = 1$.

4.5 Comparison of the dimensionality in the Hubbard Model

In the separate consideration of the cases for the Hubbard model we have tried to understand the output which we obtained. All of the spectral functions and the corresponding density of states clarify the major differences in one-, two- and three-dimensional Hubbard model or rather within the approximation. It is quite intuitive that this difference will propagate in the evolution of our spatially evaluated self-energy localization measure. Now we can summarize all of this cases in figure 4.15.

From this it is apparent that the dimensionality suppresses more and more the non local correlations and the weight of the local correlations increases. For instance, at distance 1 the measure drops to around 0.75 in $1D$, to 0.55 in $2D$, and to 0.4 in 3D. Even in $3D$, non-local correlations cannot be neglected completely. But compared to $1D$, short-length scales obviously capture the relevant physics much better in higher dimensions.

5 MOTT-HUBBARD TRANSITION IN THE TWO-DIMENSIONAL HUBBARD MODEL

5.1 Introduction

The main results obtained in this Chapter are calculated in collaboration and are published in Ref. [20]. Therefore the necessary VCA results for this analysis were calculated within this thesis and DΓA calculations were done by our collaborators Thomas Schäfer, Alessandro Toschi, Karsten Held, Georg Rohringer and the BSS-QMC calculations were done by Nils Blümer.

The main idea of this work is the study of the the effect of the non-local electronic correlations at all length scales on the Mott-Hubbard metal-insulator transition (MIT)[73] in the unfrustrated two-dimensional Hubbard model. In the regime where the short range correlations are taken into account, frustration and their impact on the metal-insulator transition can be easily considered. This gives an important clue to the physical mechanisms which are playing a role.

The Mott-Hubbard metal-insulator transition (MIT) belongs to the important areas of electronic correlation physics. It concerns the competition between kinetic energy and correlation energy which manifests itself in the particle-like and wave-like character of the electrons. This particle-like and wave-like character of the electrons is related to quasi-particles and Hubbard bands[74]. In an experimental setup the Mott transition can be observed in form of spectral weight transfer from wave-like quasi-particles to the atomic-like Hubbard bands[60]. This spectral weight transfer can be generated by several mechanisms, such as temperature, pressure or doping. Nevertheless, there are still many open issues, even for the simplest model, the single-band Hubbard Hamiltonian. Analytical and numerical exact solutions for this model are only available in the limiting cases of one and infinite dimensions.

Let us consider these two special cases in respect of MIT. In the one-dimensional case, the Bethe Ansatz shows that for the vanishingly small Hubbard interaction parameter U there is no Mott-Hubbard MIT, i.e., the system remains in the insulating phase with a gapped spectral function. More exactly, at any $U > 0$ the one-dimensional Hubbard model at half filling is insulating[37, 75, 76]. The physics of the one-dimensional case is differing from other cases in many aspects. There are strong, long-ranged antiferromagnetic spin fluctuations which are decaying slowly. These fluctuations prevent antiferromagnetic ordering even at the zero temperature ($T = 0$). Also the metallic phase for this case is not a Fermi liquid but a Luttinger liquid, which is reached by

doping.

In the other limiting case of infinite dimensions ($D = \infty$) dynamical mean field theory (DMFT) is exact and delivers an idealized description of a pure Mott-Hubbard MIT. In this limit non-local correlations vanish and only local correlations survive, which was obtained from diagrammatic techniques[6]. Here, after the transition, one obtains a collection of localized (but not long-range ordered) magnetic moments. This way, if antiferromagnetic order is neglected or sufficiently suppressed, DMFT describes a paramagnetic first-order MIT, ending a critical end point[7, 77].

After the consideration of the MIT for the extreme limiting cases, we can look at the realistic cases of the two- and three-dimensional Hubbard model. For this purpose we shall consider the DMFT description of the MIT. Because of the mean-field character of this method antiferromagnetic fluctuations above the antiferromagnetic ordering temperature T_N (Néel temperature) have no influence on the DMFT spectral function and self-energy.

In the three dimensional case these antiferromagnetic fluctuations reduce T_N which can be seen in figure 5.2. DMFT gives appropriate results for this case except close to the antiferromagnetic transition, whereas deviations from the DMFT entropy and susceptibilities can be significant also at higher T[78]. Nevertheless DMFT yields a good description of the MIT of realistic materials such as V_2O_3[79, 80].

The two-dimensional case is of great interest because a lot of interesting physical phenomena occur in layered systems. For instance, in the class of cuprate high-T_C superconductors[4] there are relevant CuO_2 planes and in the class of prictinide high-T_C superconductors[5] there are relevant iron and a prictinide layers which are conducting. This layered structure is shared by these materials. There is also a rapidly emerging field of oxide thin films and heterostructures which is of great interest from a the technological point of view. Because of these reasons the study of two dimensional Hubbard model is important. In this area there are still many open questions. Numerical and analytical studies indicate a metallic phase with a MIT in the weak coupling regime with a critical finite value U_C[81, 82, 83]. On the other hand two particle self-consistent approach gives a pseudo-gap in the weak coupling perturbative regime[84].

New emerging advanced numerical methods such as cluster DMFT (CDMFT)[85], dynamical cluster approximation (DCA)[70], second order dual-fermion approach[36] where non-local correlations are systematically included, show a reduced critical interaction U_C. This comes from short-range spin fluctuations as it is seen in figure 5.2.

In this chapter we are going to consider MIT in two dimensions on a square lattice. We will compare different methods such as the variational cluster approximation (VCA), which includes short-range correlations, the dynamical vertex approximation (DΓA), which includes short-and long-range correlations beyond DMFT on the same footing, and extrapolating lattice quantum Monte Carlo (BSS-QMC) simulations of higher accuracy. These more accurate methods take into account physical mechanisms and interactions such as spin-fluctuations.

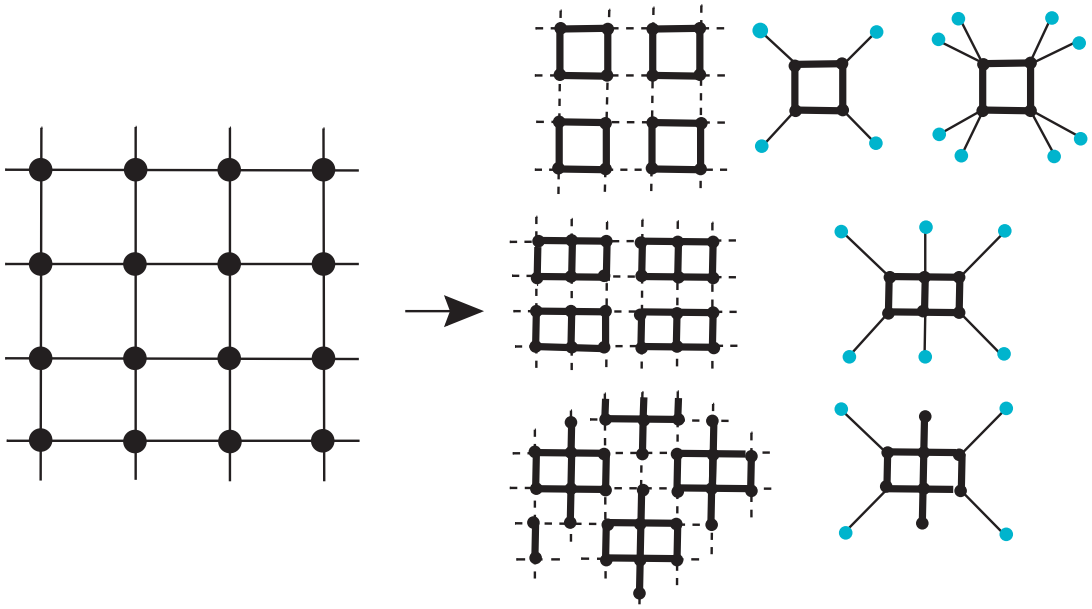

Figure 5.1: Schematic representation of the generation of reference systems out of the original system. Left column: the original two-dimensional lattice system; middle column: the original system is tiled into finite clusters (2×2, 2×2, 2×3, $\sqrt{8} \times \sqrt{8}$) which are connected perturbatively. Right column: addition of bath sites, represented by blue dots for the generation of reference systems ($2 \times 2 + 4B$, $2 \times 2 + 8B$, $2 \times 3 + 6B$, $\sqrt{8} \times \sqrt{8} + 4B$), where finite size effects are minimized.

5.2 System and methods

First let us give some general information concerning our system of interest. Here we are going to study the half-filled two-dimensional Hubbard model on a square lattice with nearest neighbor hopping. For the VCA calculations we consider the reference systems in figure 5.1, where the original system of interest is replaced by cluster tilings which are in the CPT approximation perturbatively connected. In the VCA calculations one-particle variational parameters are added to enhance the calculations. This can be done by adding bath degrees of freedom in order to minimize the finite-size effects and to reach a metal insulator transition. The hybridizations $(t_b)_i$ and the on-site energies $(\epsilon_b)_i$ of the bath sites are variationally determined. The VCA calculations are performed at the zero temperature $T = 0$ and are compared with CDMFT.

On the other side for the DΓA data which is a diagrammatic extension of DMFT[36, 86] we will use the two-particle vertex[87] in its ladder version[88]. The results from this approach are directly at the thermodynamic limit and can be compared with lattice Blankenbecler-Scalapino-Sugar (BSS)-QMC calculations[21]. In these kind of Monte

Carlo calculations there is still a bias due to a Trotter discretization of the imaginary time. It is applicable to the Hubbard model with fixed number of lattice sites L, where the numerical affort scales as L^3/T at temperature T . But one can perform a reliable extrapolation to the thermodynamic limit[22].

5.3 Phase diagram

After some motivation concerning the system of interest and the corresponding methods for the analysis, let us collect the results in figure 5.2, which gives us a summarized picture for the metal-insulator transition for the half-filled Hubbard model. In this figure the temperature T and the Coulomb interaction U are plotted for different methods with different level of approximation.

In the DMFT approach Hubbard model at half filling delivers for the control parameters T and U four different phases. These are the paramagnetic metallic phase, the paramagnetic insulating phase, insulating antiferromagnetic phase, antiferromagnetic metallic phase (in presence of magnetic frustration)[89, 90]. The blue region in figure 5.2 shows the DMFT data where only local correlations are respected and indicates a coexisting critical region of paramagnetic metallic and insulating solutions bounded by the dotted lines at the energies $U_{C1}(T)$ and $U_{C2}(T)$. The dark blue line $U_C(T)$ gives the separation line where the metallic phase disappears, but with a wrong slope, i.e., an increasing critical U_C with decreasing temperature $T \to 0$.

In contrast with this our VCA calculations at $T = 0$ marked by orange cross in figure 5.2, where short range antiferromagnetic correlations are included, are consistent with the CDMFT[85], DCA, previous VCA[91] and dual-fermion[36] calculations. Again a critical region which is bounded by dotted violet lines at the energies $U_{C1}(T)$ and $U_{C2}(T)$ is obtained, but the violet solid line gives the critical $U_C(T)$ with an opposite slope. Other important aspects compared to the standard DMFT results are that the width of the coexistence region, which is obtained from CDMFT, and the critical interaction strength U_C are strongly suppressed.

In order to consider this evolution further we have to include the important long-range correlations. This can be done within the DΓA approach. The corresponding data in figure 5.2 represented by the red dashed line shows the opening of a spectral gap which is due to the strong antiferromagnetic spin fluctuations and the strong enhancement of the electronic scattering rate in the very low frequency regime . This spectral gap exists even at arbitrarily small interaction values U. Consequently one can say that there is no MIT for the two-dimensional Hubbard model for $T \to 0, U_C \to 0$, which is similar to the one-dimensional case. This result can be compared with the extrapolated BSS-QMC data with their corresponding error bars. Indeed they show a strong confirmation of the DΓA results.

Let us summarize our statements or rather the implications from the results in figure 5.2. These results indicate that there is a strong effect of the spatial extended antiferromagnetic correlations on the Mott-Hubbard metal-insulator transition in the two-dimensional Hubbard model which is in the paramagnetic phase. In the next sections

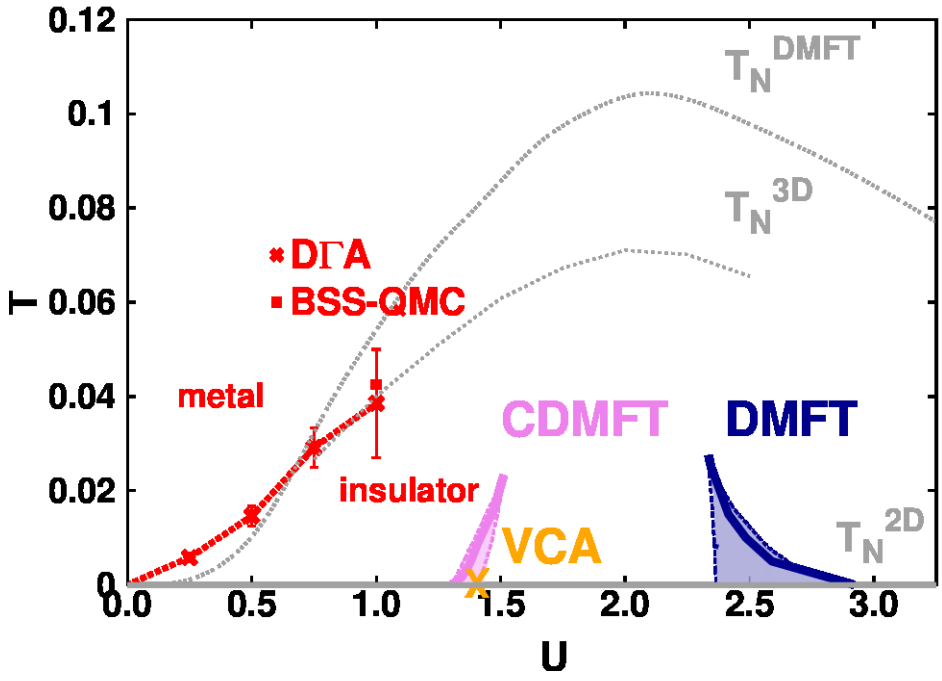

Figure 5.2: Metal-insulator transition of the two dimensional Hubbard model on a square lattice[20] calculated by different non-perturbative many body techniques: DMFT, CDMFT, VCA, DΓA, BSS-QMC. The dotted lines give the Néel temperature T_N. Blue region: In DMFT only local correlations are respected and it gives a coexistence regime with a finite critical U_C but with a wrong slope. Orange and violet region: CDMFT and VCA where short ranged correlations are respected give a shrinked regime with a right slope and a suppressed critical U_C in comparision to the DMFT results. Red line: DΓA and BSS-QMC results, where long range correlations are included indicate a vanishing critical U_C. This plotted data are in units of the half bandwidth $W = 4t$.

we are going to differentiate between these spatial non-local correlations over different length scales and their physics concerning the MIT. We will also consider the influence of the frustration for the short length scales.

5.4 Unfrustrated short range correlations

In the last chapter we have realized that CPT and VCA calculations without bath sites deliver for a finite U always an insulating solution because of the finite size effects and the strong localizations tendency of the electrons. Also the influence of the infinite spatially extended lattice sites on the finite clusters is not incorporated in an appropriate manner, at least not for the metallic solutions. This impact can be simulated by a reservoir of electrons or, for a finite system, by a finite number of non-interacting lattice sites, i.e., bath sites. For a 8 site cluster tiling with four bath sites (the configuration sketched in figure 5.1) we can consider the physical solutions, i.e., the stationary points of the VCA grand potential $\partial\Omega(t')/\partial t' \stackrel{!}{=} 0$ which is demonstrated in figure 5.3. Because of the particle hole symmetry, we get a symmetric grand potential function $\Omega(t')$ and with regard to this fact there is only one non-trivial, i.e., $t' \neq 0$ insulating solution for every fixed U value, which can be identified by the consideration of the density of states and imaginary part of the self-enery .

This statement concerning the insulating behaviour can also be confirmed by the consideration of the corresponding density of states in figure 5.4 for the non-trivial solutions. It is obvious that the system remains in the insulating phase even for a very small value of U. From these results we can conclude that for the observation of a metal-insulator transition in this case there are still not enough bath degrees of freedom which would allow the system to get into the metallic regime. Because of these results and the consideration of other reference systems with different bath configurations we can conclude that the number of bath sites has to be at least equal to the number of cluster sites. Now we can switch to another reference system, i.e., 2×2 cluster tilings with four bath site configurations. In this system the number of bath sites is equal to the cluster sites. For this reference system there is indeed a coexistence region for a metallic and an insulating solution which is shown in figure 5.5. For the corresponding solutions at the metal-insulator transition the study of the density of states $\rho(\omega)$ and of the self energy in figure 5.6 show indeed the coexistence of the metallic and insulating solution.

Now we have reached a point where a metal insulator transition occurs because in our VCA approach we are taking into account short-range correlations up to the cluster sizes exact, and the effect of the infinite system is taken into account in a mean-field manner. These variationally optimized bath site hybridization improve the description of the local quantum fluctuations. Our VCA calculations describe the physics of short range correlations in the paramagnetic phase very well because the critical interaction value $U = 1.4\ W$ for $T = 0$ is within the CDMFT coexistence region of the metallic and insulating phase as it is shown in figure 5.2. In the critical region we can consider the density of states $\rho(\omega)$ and the self-energy $\Sigma(i\omega_n)$ which is demonstrated in figure 5.6.

Here we get an insulating and a metallic solution. The insulating solution is charac-

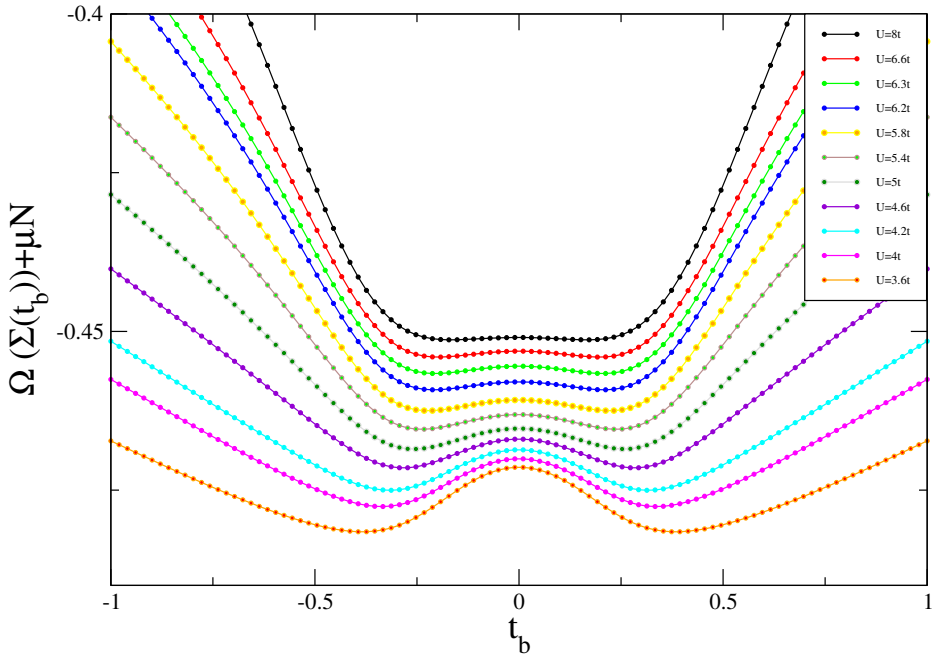

Figure 5.3: VCA: Grand potential $\Omega(t_b)$ as a function of the bath hybridization t_b for the reference system $\sqrt{8} \times \sqrt{8} + 4B$. Physical solutions correspond to the condition $\partial\Omega(t')/\partial t' \stackrel{!}{=} 0$, where t' represends arbitrary one-particle parameters ($t' = \{t,\ tb,\ \epsilon_B,\ \mu, ...\}$). There is only one non-trivial insulating solution because the function is symmetric with respect to the y axis. The interaction strength U is given in the units of the hopping parameter $t = 1$. For this reference system the metallic solution is reached only at $U = 0$.

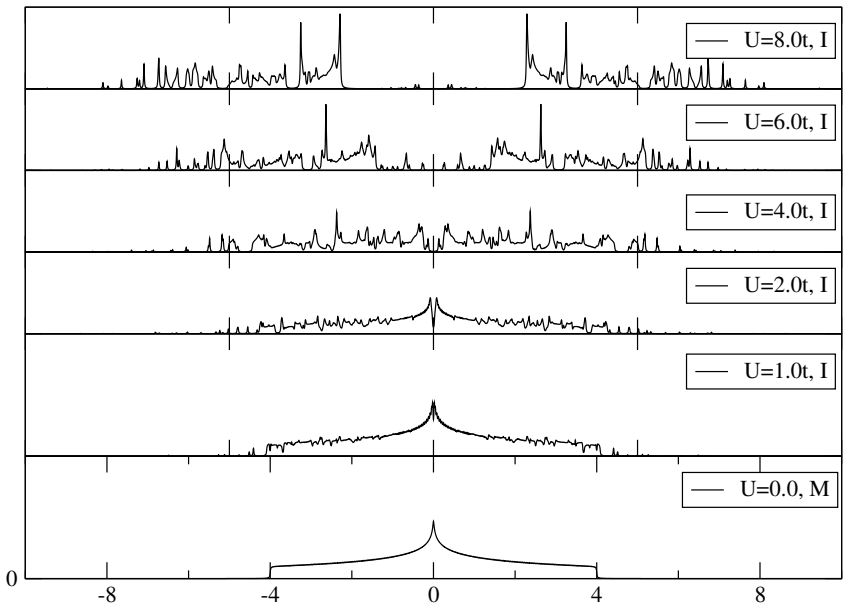

Figure 5.4: Density of states $\rho(\omega)$ for the reference system $\sqrt{8}\times\sqrt{8}+4B$. Optimal value of the one particle parameters ($t^{*'} = \{t^*, t_b^*, \epsilon_b^* ...\}$) is found by the condition of the stationarity of the grand potential $\partial\Omega(t')/\partial t' \stackrel{!}{=} 0$. The system is insulating for large interaction ($U = 8t$) in the units of $t = 1$. For decreasing values of interaction U, there is no metal-insulator transition, even for very small values until the point $U = 0$, where the spectral gap is continuously closed and the metallic state is reached.

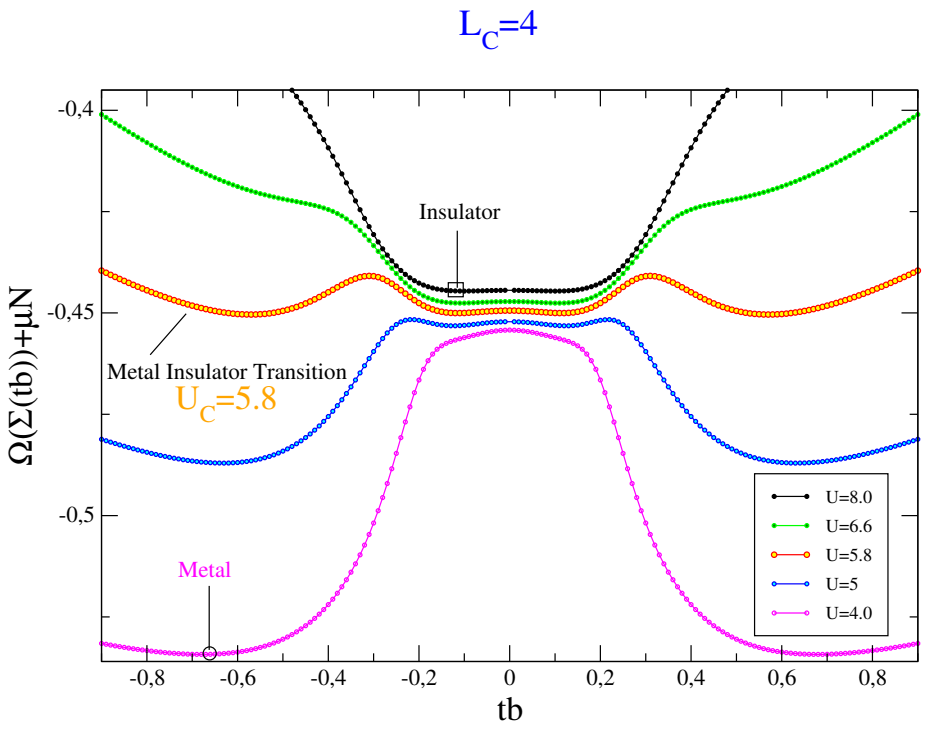

Figure 5.5: VCA: Grand potential Ω versus bath hybridization t_b for the reference system: 2×2 clusters with 4 additional bath sites . Physical solutions corresponds to the condition $\partial\Omega(t')/\partial t' \stackrel{!}{=} 0$. For large U values there is only one non-trivial insulating solution. In the critical region there are two competing solutions: metal (large t_b) and insulator (small t_b). There is a MIT at $U = 5.8t$.

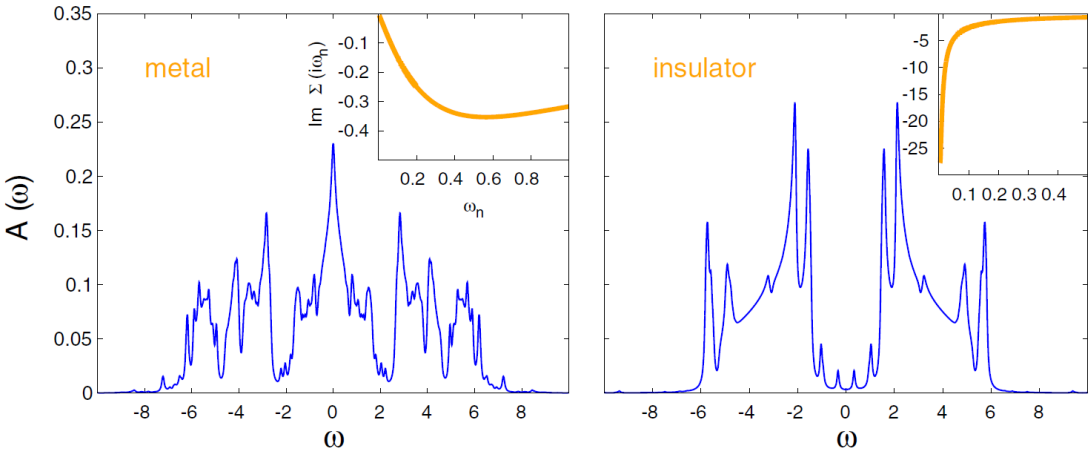

Figure 5.6: Density of states $\rho(\omega)$ for the reference system $2 \times 2 + 4B$[20]. Optimal value of the one particle parameters (t, t_b, ϵ_b) is found by the condition of the stationarity of the grand potential $\partial\Omega(t')/\partial t' \stackrel{!}{=} 0$. The system is insulating for large interaction strength ($U = 8t$). For decreasing values of interaction strength ($U \approx 5.8t$) metal-insulator transition. Two competing solutions: metal (large t_b) and insulator (small t_b) at transition. In the panel above the self-energies for the corresponding density of state at the $\mathbf{k} = (\pi, 0)$ is displayed.

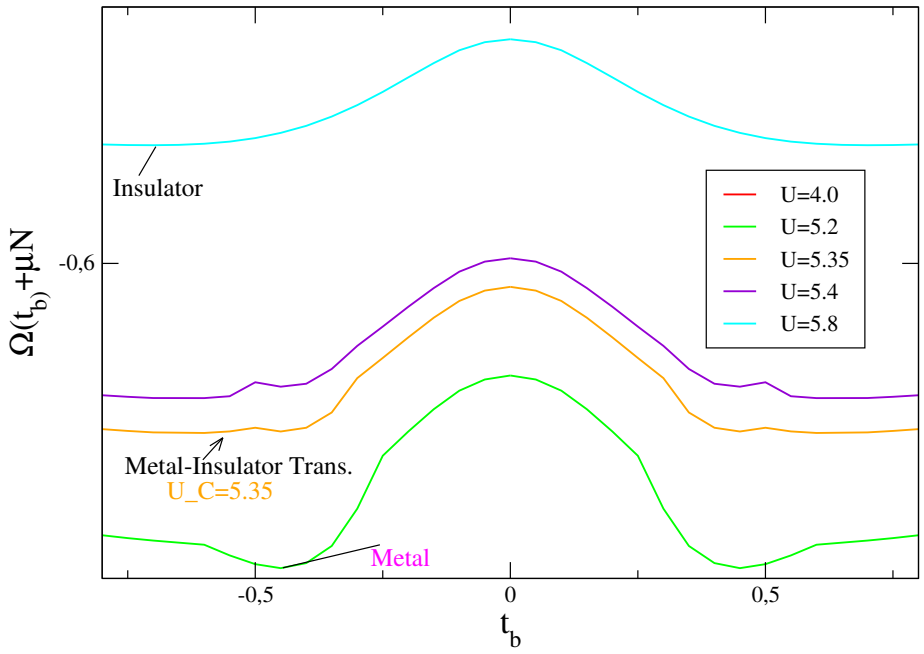

Figure 5.7: VCA: determination of the grand potential Ω versus bath hybridization t_b for the reference system: 2×2 clusters with 8 additional bath sites . Physical solutions correspond to the condition $\partial\Omega(t')/\partial t' \stackrel{!}{=} 0$. Variational parameters for this reference system are: t (intra cluster hopping), t_b (bath hybridization), ϵ_b (bath energy levels) For large U values there is only one non-trivial insulating solution. In the critical region there are two competing solutions: metal (large t_b) and insulator (small t_b) at the transition.

terized by a vanishing spectral weight at the Fermi energy and by a diverging self-energy. The metallic one has a large spectral weight at the Fermi energy and one can extract from the self-energy the value of the quasi-particle weight as $Z_{VCA} = 0.37$ at $\mathbf{k} = (\pi, 0)$.

The VCA grand potential gives for $U < U_C = 1.4W$ the thermodynamically stable metallic solution and for $U > 1.4W$ the insulating solution. There is a level crossing at $U = U_C$ which is in fairly good agreement with CDMFT[85]. This value is slightly reduced for other difference reference systems, i.e., for $N_C = 4 = 2 \times 2$ with 8 additional bath sites a critical value of $U_C = 1.3375W$ as indicated in figure 5.7. and for the reference system $N_C = 6 = 2 \times 3$ with 6 additional bath sites as indicated in figure 5.7 a critical value of $U_C = 1.325W$ is obtained.

From these results we can conclude that the short-range correlations are strong enough to destroy the low-temperature metallic phase at intermediate coupling but these are less effective for lower values of the interaction strength U. Therefore, for a correct description of the weak-coupling regime, one has to include correlations on all length scales. This will be done in the next sections but before that let us consider the effect

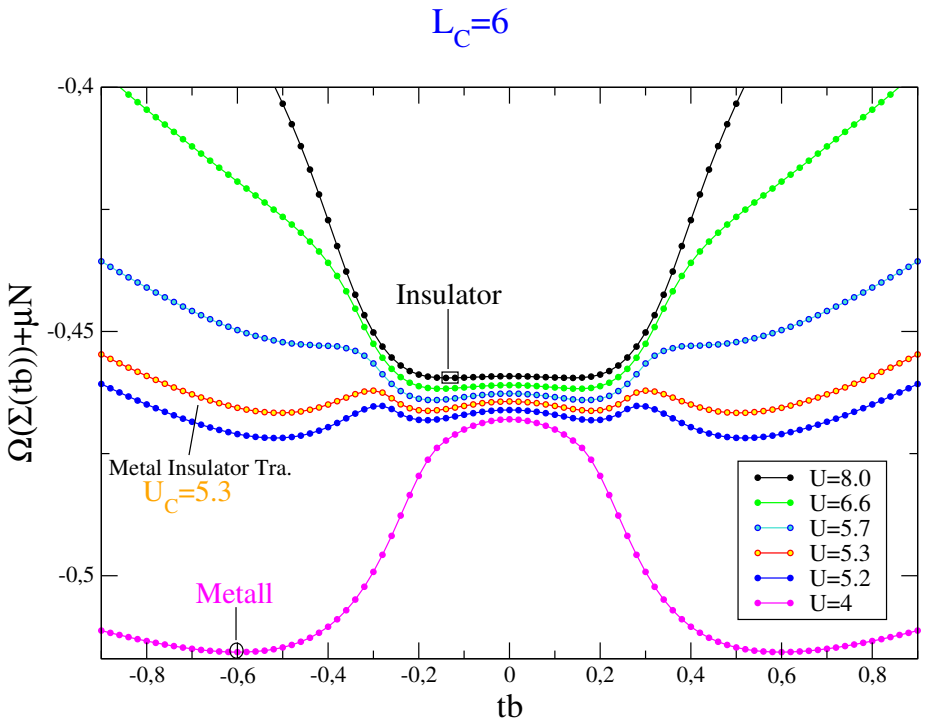

Figure 5.8: VCA: determination of the grand potential Ω versus bath hybridization t_b for the reference system: 2×3 clusters with 6 additional bath sites . Physical solutions correspond to the condition $\partial\Omega(t')/\partial t' \stackrel{!}{=} 0$. Variational parameters for this reference system are: t (intra cluster hopping), t_b (bath hybridization). For large U values there is only one non-trivial insulating solution. In the critical region there are two competing solutions: metal (large t_b) and insulator (small t_b) at the transition.

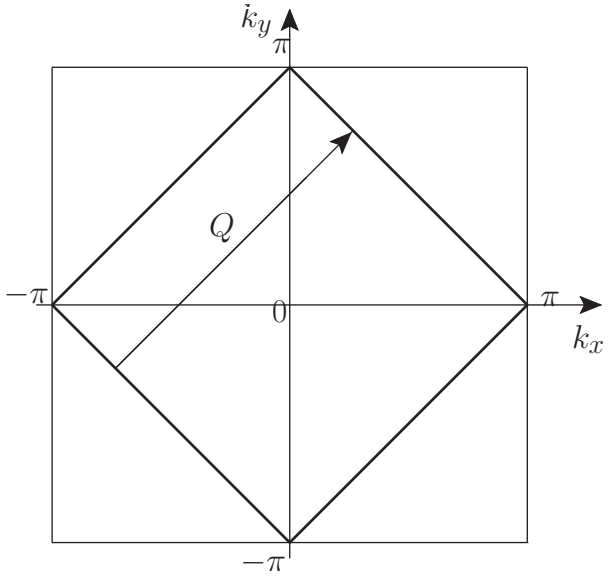

Figure 5.9: Sketch of the Brillouin zone for a square lattice where the thick black line shows the Fermi surface at half-filling for non interacting fermions. Fermi surface has essential parallel segments connected by a vector $\mathbf{Q}$. This is called nesting property.

of the frustration on the MIT.

5.5 Frustrated short range correlations

Now let us consider the effect of the frustration on the MIT. We are going to motivate this from the perspective of perfect nesting of Fermi surfaces, which is sketched for non-interacting fermions on a square lattice in figure 5.9.

In the $2D$ Hubbard model for $U = 0$ the Fermi surface is a perfect square with a nesting vector $\mathbf{Q} = (\pi, \pi)$ which connects sides of the Fermi surface. For example, if you consider a scattering process which takes an electron and adds a momentum $\mathbf{Q}$, then it is obvious that there is a single vector $\mathbf{Q} = (\pi, \pi)$ which connects a lot of $\mathbf{k}$ states in the Brillouin zone. These $\mathbf{k}$ states have the same energy. The $\mathbf{k}$ states around the Fermi surface are the only important states for the low temperature regime. The static structure factor is peaked around that $\mathbf{Q}$. Here it is obvious that Fermi surface nesting gives rise to different orders. Spin preserving scattering would lead to a charge density waves but for the magnetic scattering which flips the spin of the electron, one would get a spin density waves state.

We will see in the next section that the long-ranged antiferremagnetic fluctuations suppress the critical U_C to vanishing values. But on the other side, if we suppress this antiferromagntic fluctuations on the cluster level by frustration we would obtain exacly

the other case, i.e., the critical interaction U_C will be shifted to higher values. This can be verified in our VCA clusters by the addition of frustration, which lead to the disturbtion of the ordering caused by nesting of the Fermi surface. The results for this calculations are shown in figure 5.10 for the reference systems $2\times 2+4B$ and $2\times 3+6B$, where the grand potential at the optimal value is plotted for various external chemical potential values. At the metal insulator transition the energetic level of the metallic and insulating state should be equal. This is observed in figure 5.10, where the critical interaction at a low value of frustration $t' = 0.15$ is shifted to the following values: For the reference system $2 \times 2 + 4B$ we get a shift of $U_C = 5.8 \rightarrow 5.9$ and for the other reference system $2 \times 3 + 6B$ a similar shift of $U_C = 5.3 \rightarrow 5.5$ is obtained.

5.6 Unfrustrated long range correlations

Long range correlations at all length scales can be included in many ways. Here we will compare the results obtained within the DΓA approach and the extrapolating BSS-QMC. Each of these methods has an approximative character. In the case of DΓA, which is a diagrammatic method, the approximation is due to the selection of a class of more relevant diagrams out of many other classes. For the BSS-QMC the results which are obtained for finite systems the approximation comes from the extrapolation to the infinite system $N_C \rightarrow \infty$.

For this comparision we consider the imaginary part of the self-energy $\Sigma(\mathbf{k}, i\omega_n)$ as a function of the momentum $\mathbf{k}$ and Matsubara frequency $i\omega_n$ obtained by these methods. The momentum vector $\mathbf{k}$ is calculated at the nodal $k = (\pi/2, \pi/2)$ and the antinodal $\mathbf{k} = (\pi, 0)$ points, which are special points at the Fermi surface. For completeness we include also the DMFT and VCA results to this comparison. All the data are summarized in figure 5.11. The subplots in this picture give us the results for two different temperatures ($T = 0.025$ and $T = 0.010$) and for the interaction value $U = 0.5W$. There is a quite good agreement between the DΓA and extrapolated lattice BSS-QMC results. At the temperature $T = 0.025$ all methods deliver a self-energy with a metallic, Fermi-liquid type behaviour. Therefore for this case one can calculate an important quantity called quasiparticle renormalization which was defined in Chapter 2, and obtain the following value

$$Z = \left(1 - \frac{Im\Sigma(\mathbf{k}, i\omega_n)}{\partial\omega_n}|_{\omega_n\rightarrow 0}\right)^{-1} \simeq 0.9 \tag{5.1}$$

Here we can also evaluate the scattering rate γ at the Fermi surface for the DMFT and DΓA

$$\begin{aligned} \gamma_{DMFT} &= -Im\Sigma_{DMFT}(\mathbf{k}, i0^+) = 0.002 \\ \bar{\gamma}_{D\Gamma A} &\simeq 0.014 \end{aligned} \tag{5.2}$$

where for the DΓA the γ value is averaged over the nodal and antinodal $\mathbf{k}$ values (there is a small difference between the two values). By reducing the temperature from $T = 0.025$

(a)

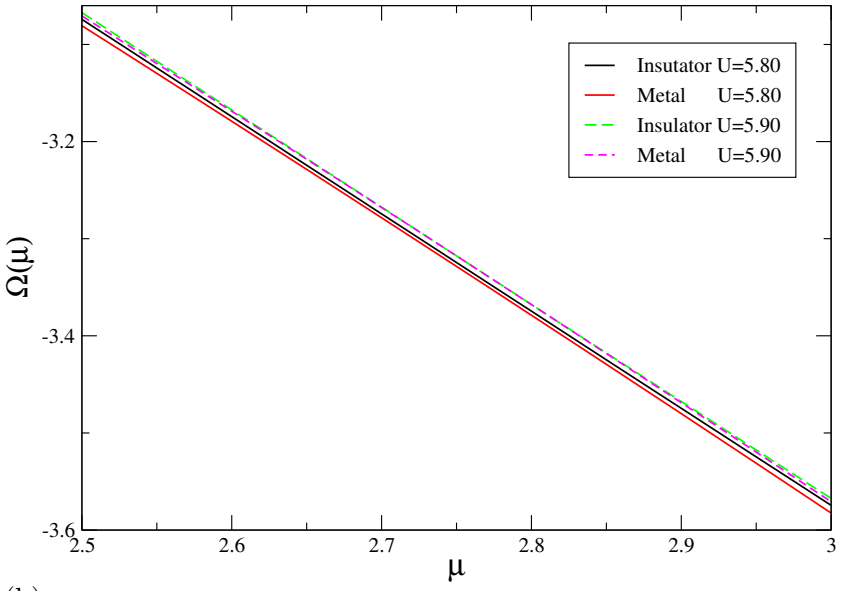

(b)

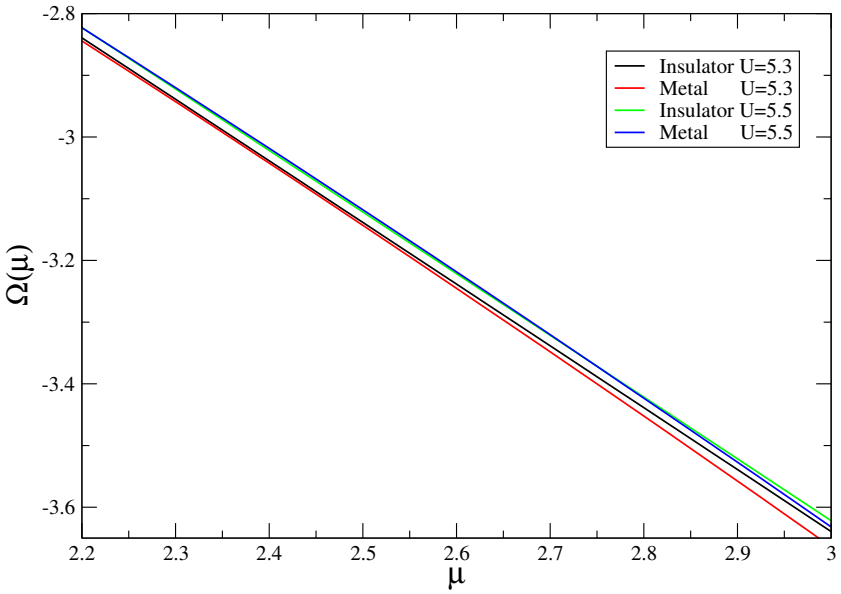

Figure 5.10: Grand potential on the stationary point $\partial\Omega(t')/\partial t' \stackrel{!}{=} 0$ for the different external chemical potential μ. Frustration shifts the finite critical interaction value $U_C > 0$ to higher values, i.e.: ad a) reference system $2 \times 2 + 4B$ with frustration, diagonal hopping $t' = 0.15$, $U_C = 5.8 \rightarrow 5.9$, ad b) reference system $2 \times 3 + 6B$ with frustration, diagonal hopping $t' = 0.15$, $U_C = 5.3 \rightarrow 5.5$

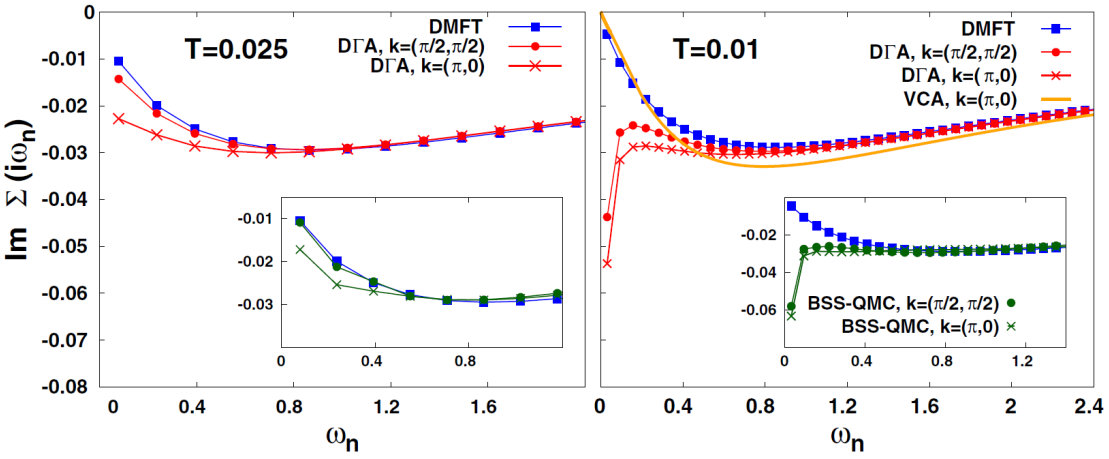

Figure 5.11: Self-energy as a function of Matsubara frequency $i\omega_n$ and momentum $\mathbf{k}$ at the nodal $k = (\pi/2, \pi/2)$ and the antinodal $\mathbf{k} = (\pi, 0)$ points as special points of the Fermi surface[20]. At the temperature $T = 0.025$ all methods indicate metallic solutions, but on the other hand for lower temperature $T = 0.010$ methods (DΓA, BSS-QMC), where long range correlations are included, give insulating solutions. Both plots are calculated for the same interaction: $U = 0.5W$.

to $T = 0.010$ the Fermi-liquid behaviour of the imaginary part of the self-energy changes dramatically for the the DΓA and extrapolating lattice BSS-QMC. The self-energies diverge at all k-points, indicating an insulating solution.

5.7 Physical interpretation

For the unfrustrated two-dimensional Hubbard model we have seen that there is no MIT for a finite interaction U. For this effect, i.e., shift of the MIT towards $U = 0$, long range spatial fluctuations are essential. These fluctuations emerge close to the $T = 0$ long-range antiferromagnetic order. For the verification of these statements we can study the DΓA spin-correlation function

$$\chi_s(\mathbf{r}, i\Omega_n = 0) = \int_0^\beta d\tau < S_z(\mathbf{r}, \tau) S_z(0, 0) >, \tag{5.3}$$

in real space and in the low-T weak coupling regime, which is demonstrated in figure 5.12. There one can observe that the spin-correlation function χ_S is decaying along the x direction with a fluctuating sign, which is a evidence for antiferromagnetic fluctuations. One can fit χ_S by its asymptotic limit[92]:

$$|\chi_S(r \to \infty)| \propto \sqrt{\frac{\xi}{r}} e^{-r/\xi}. \tag{5.4}$$

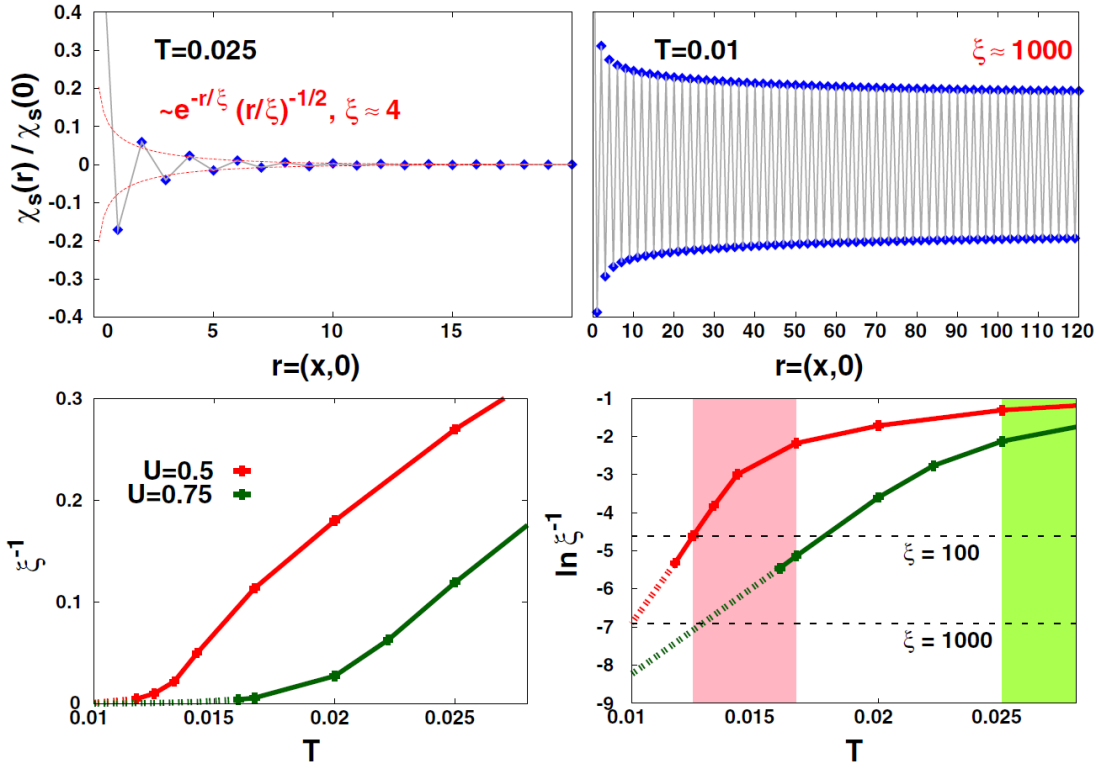

Figure 5.12: First row: Spin correlation function $\chi_S(\mathbf{r})/\chi_S(\mathbf{0})$ in the real space[20]. The x-axis gives the cut $\mathbf{r} = (x, 0)$, where x has the units of lattice spacing $a = 1$. Gray line gives the interpolation between different lattice vectors. One can fit these data with a function and by this procedure following values for the correlation length ξ are obtained: At $T = 0.025 \Rightarrow \xi = 4$ and at $T = 0.010 \Rightarrow \xi = 1000$. Second line: Inverse correlation length ξ^{-1} as a function of temperature T for different interaction values U.

From this fit one can extract the correlation length ξ. For the metallic case of $T = 0.025$ one obtains $\xi \approx 4$ and for the insulating low-T case of $T = 0.010$ the value $\xi \approx 1000$ is obtained. From here we can go a step further and analyze the temperature T dependence of the ξ in DΓA approach in figure 5.12. The low-T regime reveals a ξ of exponential behaviour because spin fluctuations in this regime have large spatial extensions. These spin fluctuations destroy the Fermi surface. Because of these reasons this regime can not be resolved within the VCA calculations.

For the extended spin correlation ($\xi \gg 100$) one can observe a small reduction in potential energy $U_{n\uparrow n\downarrow}$ by about 1%, which is a clear evidence for the Slater like nature of the antiferromagnetic fluctuations. Therefore prelocalization of the magnetic moments in destroying the Fermi-liquid state, as well as the possibility of mapping the whole low-T physics onto the 2D Heisenberg model, as proposed by Anderson cannot be used to explain effect.

These antiferromagnetic fluctuations can be interpreted as "Slater paramagnons." This is because for a finite interaction strength $U > 0$, a gap is opened at low enough T which comes from enhanced electronic scattering with extended antiferromagnetic paramagnons. These spin fluctuations are reflecting the $T = 0$ ordered phase from which they originate. They smoothly evolves from Slater-like (weak to intermediate coupling) to Heisenberg-like (strong coupling) spin fluctuations[93].

5.8 Conclusions

We have considered the effects of the spatial short and long range correlations on the MIT in the 2D half-filled unfrustrated Hubbard model. The results indicate that for all finite $U > 0$ at low temperature T the model is a paramagnetic insulator because of the strong extended antiferromagnetic fluctuations (paramagnons). These fluctuations gradually show an evolution from a Slater-like behaviour to a Heisenberg-like behaviour, which is similar to the evolution for the $T = 0$ antiferromagnet.

The methods like DMFT, CDMFT or VCA where local or rather short range correlations are included deliver a finite critical interaction U_C for the (metastable) paramagnetic phase. On the other side an effective low-T 2D Heisenberg model at strong coupling assumes preformed spins even at low U.

The methods like DΓA or BSS-QMC where long range correlations are included, give for the 2D Hubbard model a vanishing critical interaction value $U_C = 0$ and indicate that the nature of the most relevant spin fluctuations is Slater-like in the whole weak- to intermediate-coupling regime.

For this system the vanishing critical interaction $U_C = 0$ can be shifted towards finite values by frustration, because it suppresses the antiferromagnetic fluctuations. Such a frustration induces a perturbation of the perfect nesting case. It can be either induced by adding a nearest-neighbor hopping or the application of an antiferromagnetic field. For the VCA case we introduce frustration by adding nearest neighbor diagonal hoppings. Consequently the finite critical U_C is rised into higher values. On the other side MIT, which has been observed due to the long-ranged correlations at the vanishing critical

interaction value $U_C = 0$ is expected to shift to a finite $U_C > 0$ in the frustrated case. It will result into a quantum critical point.

6 COMBINATION WITH AB-INITIO METHOD FOR REALISTIC COMPOUNDS: THE APPLICATION TO $SrVO_3$ AND $SrRuO_3$

6.1 Introduction

Ab initio calculations, i.e, tackling the many body Schrödinger equation within a set of approximations without fitting the model to experimental data gives in many cases good results for the electronic properties of materials. This is the case in the DFT approach within its local approximation LDA. LDA works good for weakly correlated materials because it relies on electronic correlations in jellium. However on the other side for materials with strongly correlated electrons, e.g, for $3d$ or $4f$ states this approach is insufficient for the description of the ground state and excited state properties[94, 95, 96], because the electron density in these systems is strongly varying and the assumption of a constant density for the exchange correlation term is no more suitable. Consequently the properties of these materials change dramatically upon a small change of external parameters like the magnetic field, pressure or temperature[97]. Many transition metal oxides belong to this class of materials.

In the correlated systems electrons hesitate between localization and delocalization because of the strong Coulomb interaction[98]. This property can be observed in the study of the evolution of the spectral weight of transition metal oxides with open d-shells. There one can identify the appearance of atomic-like incoherent peaks[60] and a wave like coherent peak. These incoherent peaks can be referred as the lower and upper Hubbard band, and it is not possible to describe them within the conventional band theory. They are related to the narrow bands with a width of a few eV, e.g., $W \approx 3-5\ eV$ formed by $3d$ states. The existence of the well separated narrow bands around the Fermi level is a common feature shared by the transition metal oxides[99]. Because of this narrow bands there is a strong Coulomb interaction between the electrons and in some case this can be the reason for a material to an insulator. Electronic correlations in the narrow bands of transition metal compounds can be studied within models like the Hubbard model. DMFT is a powerful tool for dealing with such models for correlation physics.

Here comes the idea to treat the correlated bands within the DMFT and the rest of the system by DFT and such a combination of methods is referred to as DFT+DMFT[16, 17, 18, 19]. This approach helps to deal with the correlations in a proper way and was applied for the calculation of the spectral, transport, and thermodynamic properties of some

transition metal oxides and rare earth metals[18, 19]. Although this application delivers very good results in many cases, it is not adequate for the description of phenomena like the d-wave superconductivity or spin density wave phases because spatial correlations in this approach are neglected[100]. Another powerful tool for the study of the correlation physics is the variational cluster approximation(VCA). In VCA short range correlations up to the cluster size are taken into account. It can be used for the study of broken phases like the antiferromagnetic phase of the two dimensional Hubbard model at half-filling[13], for the calculation of the single particle spectral function and thermodynamic quantities of transition metal oxides like MnO, CoO, NiO, $LaCoO_3$[101, 102]. In an analogous manner one can introduce a combination of this method with the DFT for the realistic material calculations.

In Chapter 3 we have introduced separately the DFT and VCA method. Therefore here we want to go through the application of the DFT+VCA combination in a brief manner, which is very similiar to the DFT+DMFT method. It can be used on the one side for the verification of the DFT+DMFT calculations and on the other side it can open new possibilities for the research of correlation physics in low dimensions. The starting point for such a DFT+VCA calculation is a DFT calculation, where the band structure is determined as shown for the compound $SrVO_3$ in figure 6.1.

The next step is the identification of the bands with strong electronic correlations. Usually such bands are coming from strongly interacting, more localized open d and f-shells. In the compound $SrVO_3$ these bands are formed by $3d$ electrons. Because of the electric field of neighboring atoms the 5-fold (10 fold with spin) degeneracy of the d-orbitals in the atom is lifted in the solid. Consequently one obtains 3-fold degenerate $t2g(d_{xy}, d_{yz}, d_{xz})$ states and 2-fold $e_g(d_{x^2-y^2}, d_{3z^2-r^2})$ states. Due to the fact that $SrVO_3$ is a d^1 oxide, the energetically higher lying e_g orbitals are empty and we can restrict the calculation to the degenerate $t2g$ states[98].

Here one can use for the calculation of the Wannier functions out of the Bloch functions of a DFT calculation the Nth order muffin-tin orbitals (NMTO)[104] downfolding or the program packages Wien2Wannier[105] and Wannier90[106]. Using this we can obtain an effective Hamiltonian in the real space, which is restricted to the $t2g$ orbitals, i.e., it consists of 3×3 matrices. The diagonalization of these matrices gives the DFT band structure $\epsilon_{\mathbf{k}lm}$ of $t2g$ bands, which is shown for the material $SrVO_3$ in figure 6.2.

So we have generated the kinetic part of the Hamiltonian using the downfolding method. It enables us to describe the band structure close to the Fermi energy in terms of finite number of Wannier functions and consequently eliminate the rest of basis states. This effective Hamiltonian can be supplemented by a Coulomb interaction term, which is responsible for the electronic correlations. The Coulomb interaction term can be written in terms of Slater integrals[107]. In a practical calculation one has to determine the screened values of the Coulomb interaction U, and Hund's exchange J, which can be done for a parameter free, i.e., ab-initio calculation within the cLDA or cRPA approach, as explained in the chapter 3. Here we are taking $U = 4\ eV$ and $J = 0.6\ eV$ from the literature[100].

After setting up the many body Hamiltonian for a realistic material calculation, we are going to apply the VCA for the solution of this Hamiltonian which was constructed

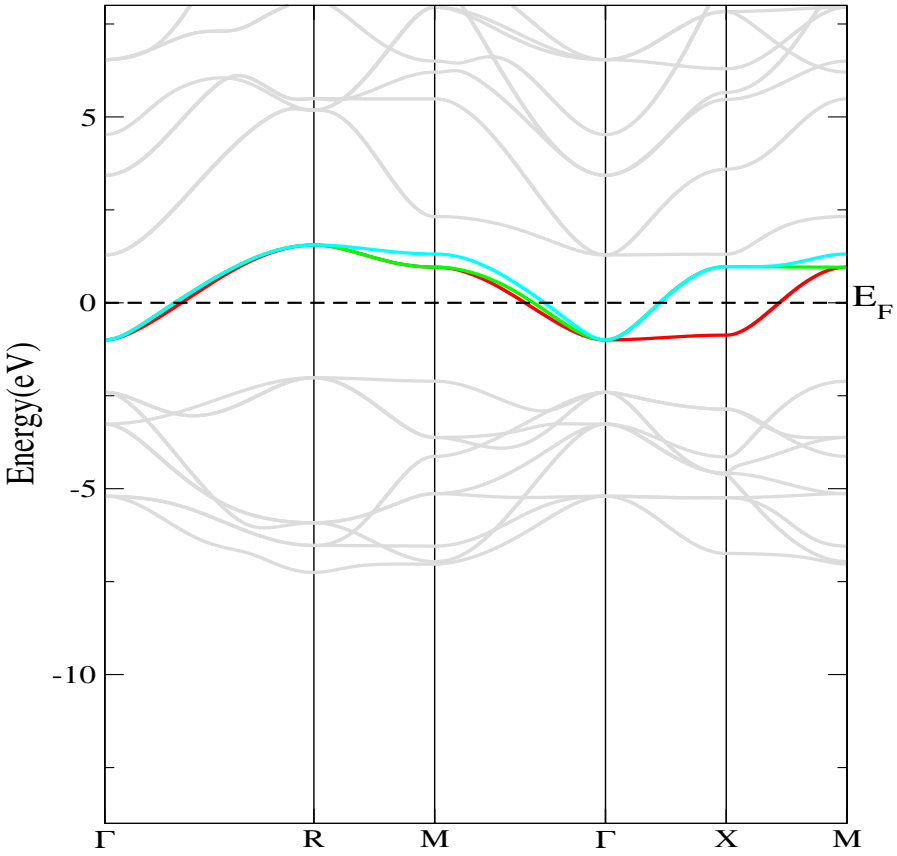

Figure 6.1: Band structure of $SrVO_3$ compound obtained from DFT package Wien2k based on linearized augmented plane waves[103]. The colorful thick solid lines around the Fermi level are $t2g$ bands.

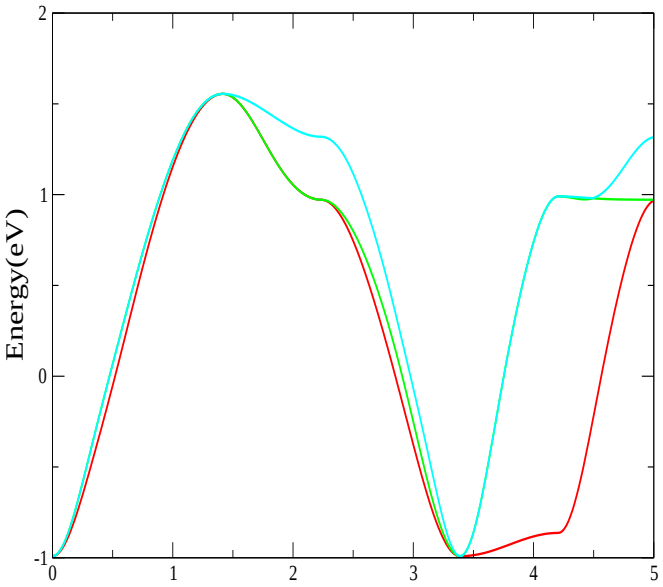

Figure 6.2: Parametrization of the kinetic part of $t2g$ orbitals obtained from the Wannier construction. These values are used for the generation of the one-particle effective Hamiltonian. These bands are obtained by the Fourier transformation of this Hamiltonian.

for specific compounds like $SrVO_3$ or $SrRuO_3$. This method can be easily transferred to other compounds, too.

Here we are going to study first the compound $SrVO_3$ because it can be considered as a prototype, i.e., simple example for transition metal oxide with a cubic perovskite crystal structure. This compound has a simple crystal structure, and there is plenty of experimental and theoretical data[108, 109, 110, 63], which would help to check the validity of our theoretical study. It would also give important clues in the study of the electronic properties of more complex systems. Then we will go on to another compound $SrRuO_3$, where spin-orbit coupling is an important quantity. This would lead to the splitting of the electronic bands, which have to be considered and this brings new physics. But before let us consider the optimal selection of the cluster configurations for such kind of VCA calculations.

6.2 Reference systems for $SrVO_3$

In the last section we have reduced the system of interest into some bands of interest, where electronic correlations are considered to be strong. For the VCA calculation we have to select an accessible reference system. This has to represent the original system as good as possible, i.e., finite size and reference system specific errors have to be minimized. Some of the possible configurations of clusters are demonstrated in figure 6.3, where the original system of interest is a lattice with 3 orbitals per lattice site.

The next step is the selection of a numerical accessible cluster tiling. Here one can perform 1 site, 2 site and 2×2 site cluster tilings. An improvement of these reference systems can be achieved in most cases by adding additional bath sites, which simulate the environment. These bath sites are important in the regimes where the overlap between the neighboring atoms is large, i.e., the value of bath hybridization $(t_b)_i$ is in a non-vanishing range. The value of these parameters are determined variationally by the VCA condition.

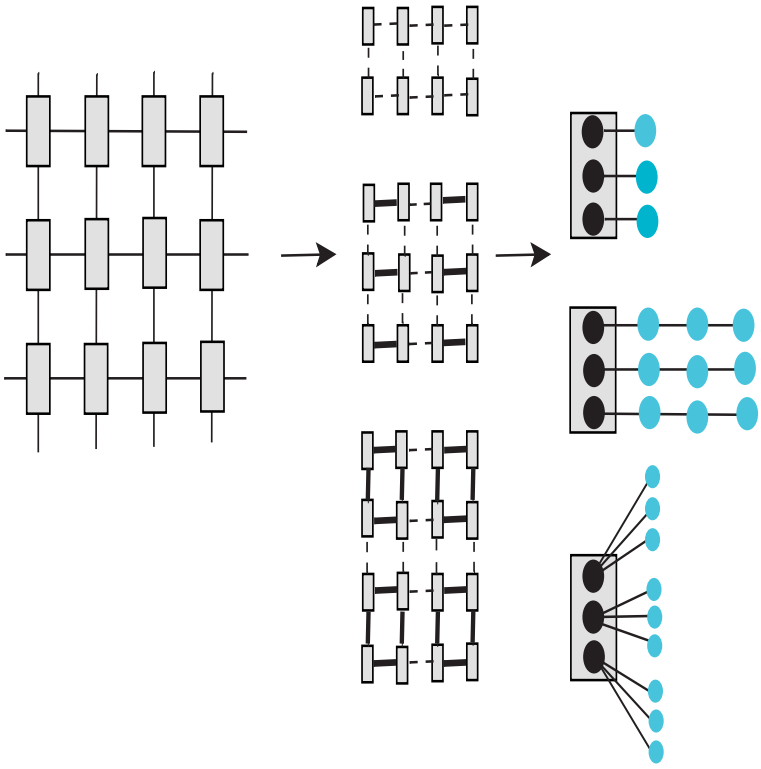

Figure 6.3: Schematic representation of the generation of reference systems out of the original system. Left column: the original multi-orbital lattice system with 3 orbitals per site; middle column: the original system is tiled into finite clusters (1 site, 2 sites, 2×2 sites) which are connected perturbatively. Right column: addition of bath sites, represented by blue dots for the generation of reference systems (3 Orbital $+ 3B$, 3 Orbital $+ 9B_1$, 3 Orbital $+ 9B_2$), where finite size effects are minimized.

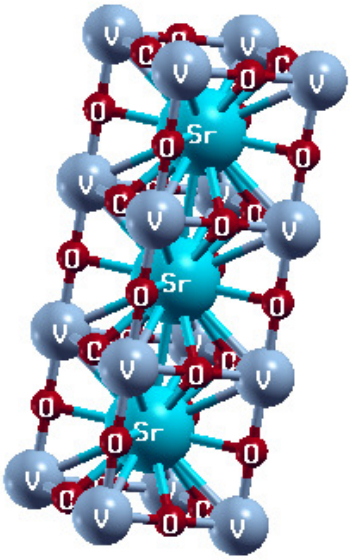

Figure 6.4: Cubic perovskite crystal structure of $SrVO_3$

6.3 Results for $SrVO_3$

Let us now apply the DFT+VCA approach to the compound $SrVO_3$, which is a cubic perovskite with a paramagnetic metallic ground state, where Sr is an alkaline earth metal and V is a transition metal as demonstrated in figure 6.4. The unit cell contains 5 constituent atoms with a lattice parameter of $a = 7.2605$ Å.

There has been some early studies which argued that the material $SrVO_3$ exhibits weak electronic correlations[111]. In their justification for this assumption they argued that if the d-band electrons of vanadium were completely localized due to the strong electronic correlation then the resultant spin of vanadium should be $1/2$ and which would result in spin ordering but there is no experimental evidence of such an ordering. Furthermore it was argued that band theory based LDA result for the effective mass of $m^* = 2.98m_0$ is a good estimate.

Through the enhancement of the ab-initio and band body methods this statement about weak correlations of $SrVO_3$ has been corrected towards modest correlations[100].

The electronic states near the Fermi level are mainly contributed from the d-orbitals of the vanadium atom because the s- and p-bands of oxygen are completely occupied

and d-bands of vanadium are partially occupied as demonstrated in figure 6.5. The $t2g$ bands with a bandwidth of $W = 2.8\ eV$ are crossing the Fermi level which has been shown in LDA calculations as shown in figure 6.1.

Now we are going to construct an effective Hamiltonian for these $t2g$ bands, therefore we have to fix an energy window around these bands. Through the consideration of the band structure in figure 6.1 one can choose such a window from $-1\ eV$ to $2\ eV$. In next step we use for the downfolding the program packages Wien2Wannier[105] and Wannier90[106]. The program package Wien2Wannier is used as an interface for the generation of the input files for the Wannier90 program package out of the ab-initio electronic structure package Wien2k. This input files are used for the generation of the maximally localized Wannier functions. By this procedure we obtain parametrization of the kinetic part of t2g orbitals which is used for the construction of the hopping part of the Hamiltonian. The Fourier transformation of this Hamiltonian delivers exactly the $t2g$ LDA bands as shown in figure 6.2. In the next step this effective spin-diagonal one-particle Hamiltonian

$$H_{eff} = \sum_{ij\alpha\beta\sigma} t_{i\alpha,j\beta} c^{\dagger}_{i\alpha\sigma} c_{j\beta\sigma} \tag{6.1}$$

with the lattice site indices i and j orbital indices α and β and spin index σ is supplemented by a two-particle Coulomb interaction term.

$$H_{int} = \frac{1}{2} \sum_{i,\alpha\beta\gamma\delta,\sigma\sigma'} U_{\alpha\beta\gamma\delta} c^{\dagger}_{i\alpha\sigma} c^{\dagger}_{i\beta\sigma'} c_{i\delta\sigma'} c_{i\gamma\sigma} \tag{6.2}$$

For a three band model one can write this term in the following way

$$\begin{aligned} H_{int} &= \frac{1}{2}[\sum_{i,\alpha\beta,\sigma\neq\sigma'} U_{\alpha\beta\alpha\beta} n_{i\alpha\sigma} n_{i\beta\sigma'} \sum_{i,\alpha\beta,\sigma=\sigma'} (U_{\alpha\beta\alpha\beta} - U_{\alpha\beta\beta\alpha})\, n_{i\alpha\sigma} n_{i\beta\sigma'} \\ &+ \sum_{i,\alpha\beta,\sigma\neq\sigma'} U_{\alpha\alpha\beta\beta} c^{\dagger}_{i\alpha\sigma} c^{\dagger}_{i\alpha\sigma'} c_{i\beta\sigma'} c_{i\beta\sigma} - U_{\alpha\beta\alpha\beta} c^{\dagger}_{i\alpha\sigma} c_{i\alpha\sigma'} c^{\dagger}_{i\beta\sigma'} c_{i\beta\sigma}] \end{aligned} \tag{6.3}$$

where the first two terms corresponds to the density-density interactions and the third term to pair hopping and the last term to spin flip terms. We have to fix the input parameters Hubbard interaction U and Hund's coupling J. We set them according to the literature to the values $U = 4\ eV$ and $J = 0.6\ eV$[100]. The interaction term can be approximated further by constricting it to the density-density terms because the pair hopping and spin flip contributions are small.

After these preparations of our setup, we can apply the VCA method on the generated Hamiltonian. For the VCA approach we have to fix the reference system. First we start with reference systems without bath sites as shown in the second column of figure 6.3, where the original three orbital per site lattice system is replaced by 1 site, 2 sites and 2×2 sites cluster systems. For these reference systems one can consider the evolution of the density of states $\rho(\omega)$, as shown in figure 6.6. There the figure 6.6 shows the non-interacting case, more precisely the LDA result, which is equal for every reference

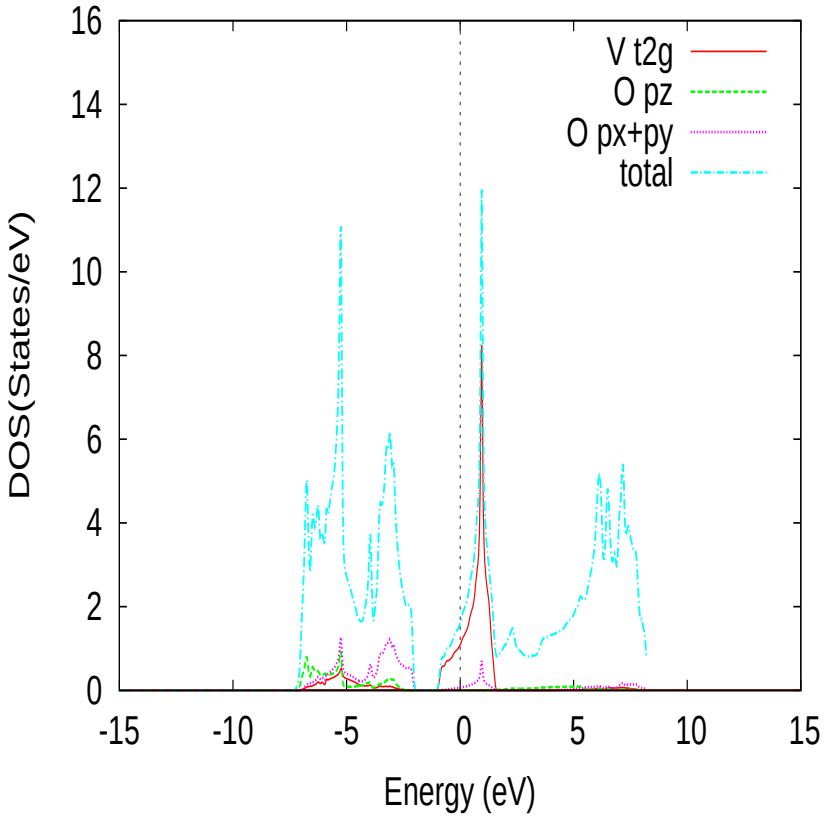

Figure 6.5: Total and partial contributions of the orbitals to the density of states close to the Fermi energy level. The blue dotted line gives the total density of states. The red solid line shows that the spectral weight around the Fermi energy comes almost from the vanadium $t2g$ bands.

system. In figures 6.6 (b), (c), (d) are the results for the reference systems 1 site, 2 site and 2×2 reference systems for the interacting case with the parameters $U = 4\ eV$, $J = 0.6\ eV$ and with a filling of $n = 1/3$, i.e., one electron in 3 orbitals. These results show an evolution into the right direction but they are far away from LDA+DMFT results because of large finite size effects and it is no metal.

Consequently in order to reduce these problems we need additional degrees of freedom, i.e., more variational parameters. These demands can be fulfilled by a reservoir of non-interacting electrons, which can be simulated by non-interacting lattice sites, i.e., bath sites. Examples for accessible cluster configurations with bath sites are shown in the third column of figure 6.3.

The results for the simplest possible cluster configuration with 3 orbitals + 3 bath sites brings a large enhancement of the previous results. Figure 6.7 shows the results for this configuration in comparision with the DFT+DMFT calculation with a continuous-time quantum Monte Carlo (CT-QMC)[112, 113] impurity solver. The peak structure of DFT+VCA result comes from the finite bath discretization. In the DFT+VCA result we see that the coherent peak of the DFT+DMFT calculation around 0.5 eV is reproduced up to a good approximation. On the other side for the incoherent atomic like Hubbard satellite we obtain a peak around $-1.5\ eV$. These results are in good agreement with the APRES measurements [110]. The appearance of an extra peaked structure in the IPES region is due to the finite number of bath sites.

The same calculation is repeated in figure 6.8 for another configuration with 3 orbitals + 9 bath sites, which gives similiar results with a small enhancement of the results.

Another important quantity is the self-energy which reveals many important features of this system of interest. Figure 6.9 shows the comparison between the imaginary part of self-energies $Im\Sigma(i\omega)$ on the Matsubara axis for this system, where the orange line corresponds to the VCA result and the blue line corresponds to the DMFT result. Both cases deliver for the imaginary part of the self-energy non-diverging finite values, i.e., a system with a metallic behaviour. One can also use this quantity for the calculation of the quasiparticle renormalization and the effective mass, which describe the residual Fermi liquid character of this system. We obtain for the quasiparticle renormalization Z and for the effective mass m^* the following values

$$Z = \left(1 - \frac{Im\Sigma(\mathbf{k}, i\omega_n)}{\partial\omega_n}|_{\omega_n \to 0}\right)^{-1} \simeq 0.48 \tag{6.4}$$

$$m^* = 1/Z \approx 2.08m, \tag{6.5}$$

which are in good agreement with the experimental value from the ARPES measurements $m^* \approx (1.8 \pm 0.2)m$[109]. In the next section we are going to apply this method to another compound $SrRuO_3$, where the spin-orbit coupling is an important quantity, which has to be included into the consideration.

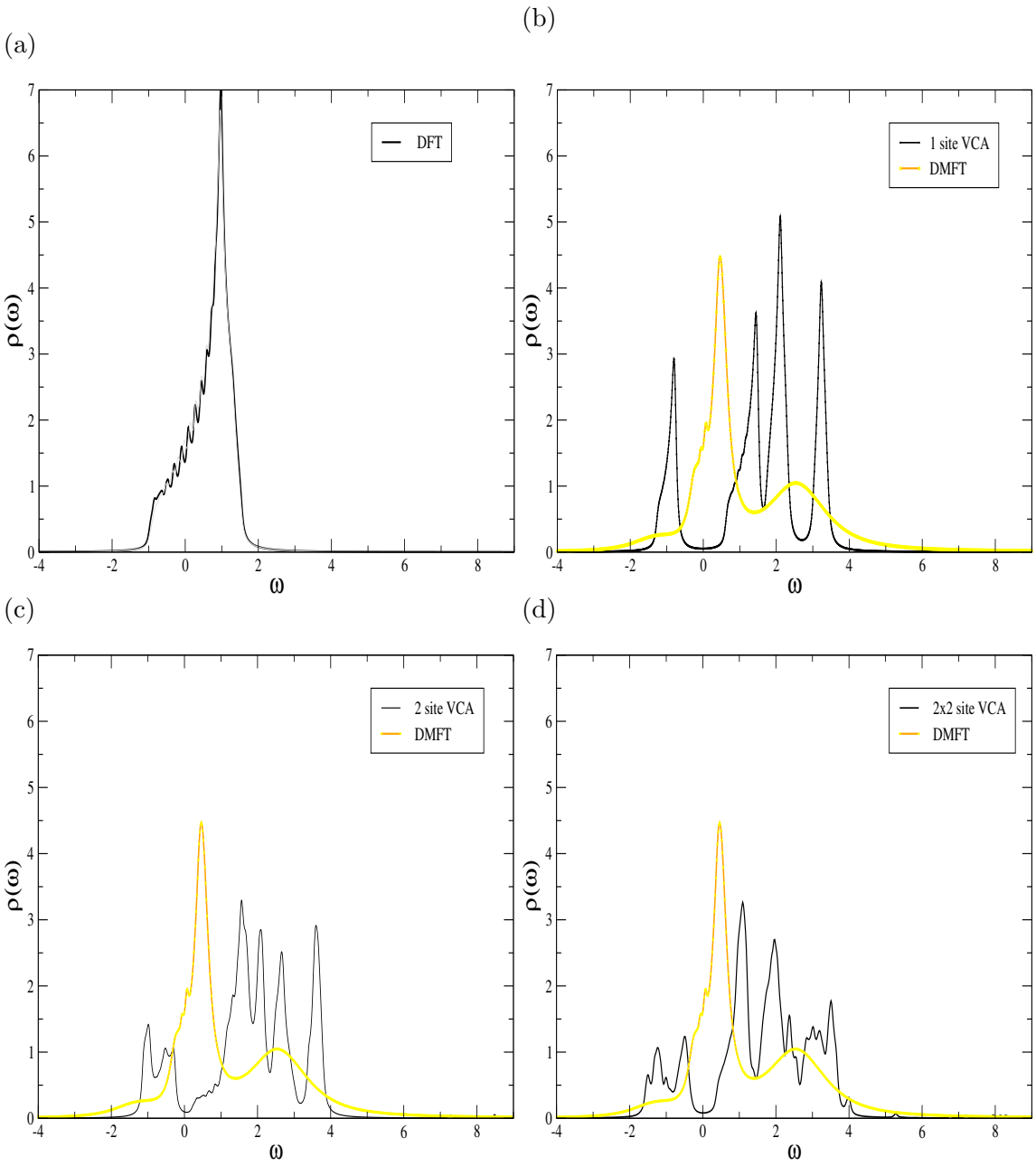

Figure 6.6: Density of states for t2g orbitals for different clusters without bath sites. The values of parameters Hubbard U and Hund's coupling: (a) $U = 0.0$, $J = 0.0$, it is exact for all clusters. (b)-(d) $U = 4.0\ eV$, $J = 0.6\ eV$. Used reference systems: (b) 1 site(3 orbitals) clusters, (c) 2 site clusters with 3 orbitals per site, (d) 4 site cluster with 3 orbitals per site. These results are compared with DFT+DMFT results.

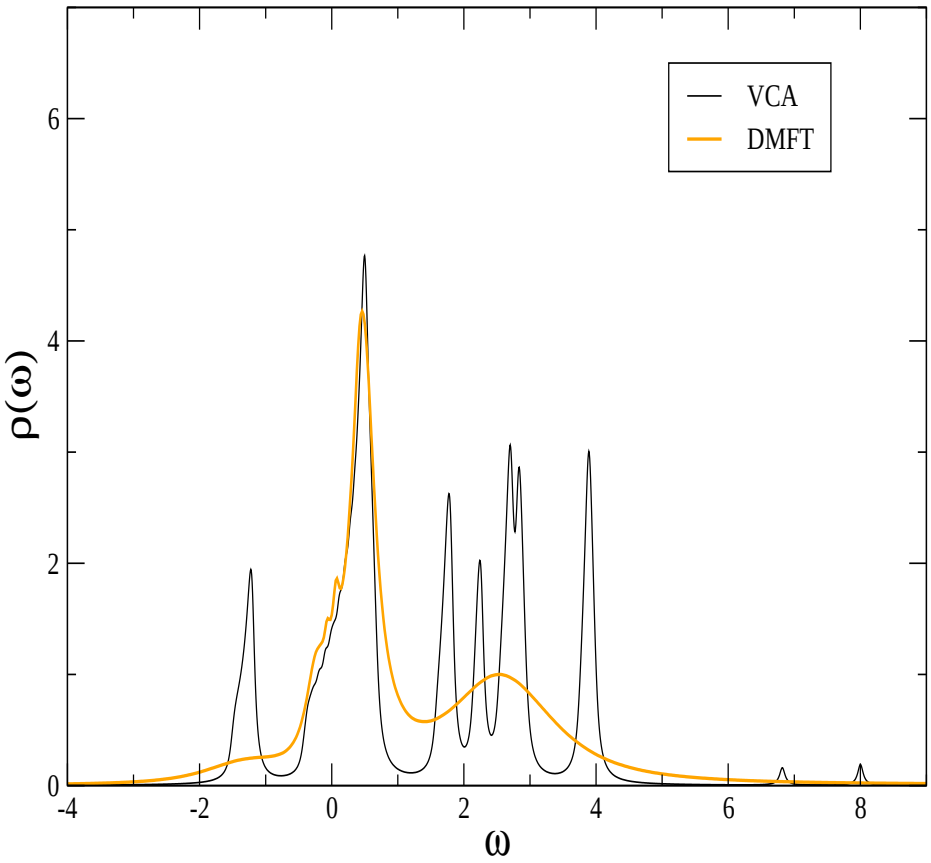

Figure 6.7: Comparison of density of states obtained from VCA and DMFT. The parameters used are $U = 4.0\ eV$, $J = 0.6\ eV$. For the VCA calculations 3 orbitals + 3 bath sites are used. The three $t2g$-orbitals are degenerate and the effect of the surrounding is simulated by bath sites, where the bath hybridization t_b and the on-site energies ϵ_b are variationally determined. The result shows a coherent quasi-particle peak and two incoherent peaks referred as the lower and the upper Hubbard satellites.

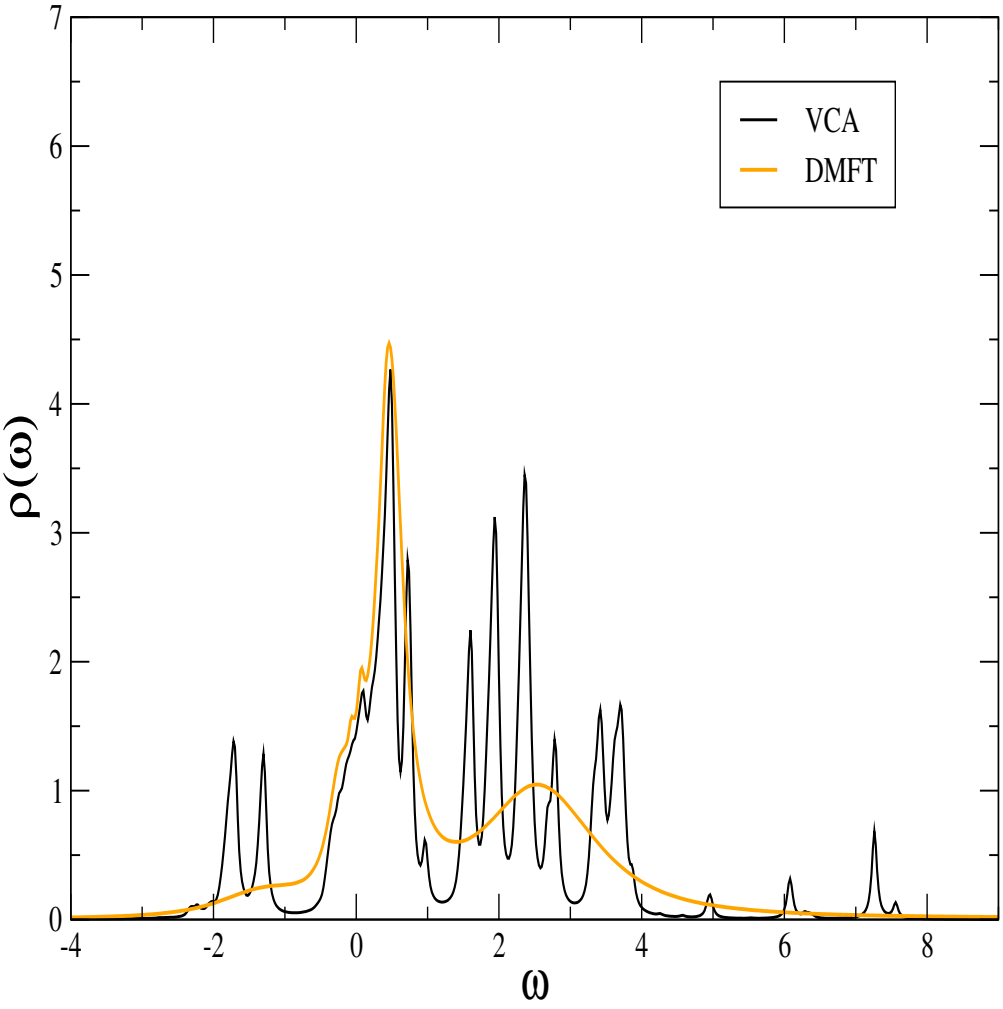

Figure 6.8: Comparison of density of states obtained from VCA and DMFT. The parameters used are $U = 4.0\ eV$, $J = 0.6\ eV$. For the VCA calculations the configuration 3 orbitals + 9 bath sites is used. The three $t2g$-orbitals are degenerate and the effect of the surrounding is simulated by bath sites, where the bath hybridization parameters $(t_b)_i$ and the on-site energies $(\epsilon_b)_i$ are variationally determined. The result shows a coherent quasi-particle peak with a substructure and two incoherent peak regions referred as the lower and the upper Hubbard satellites.

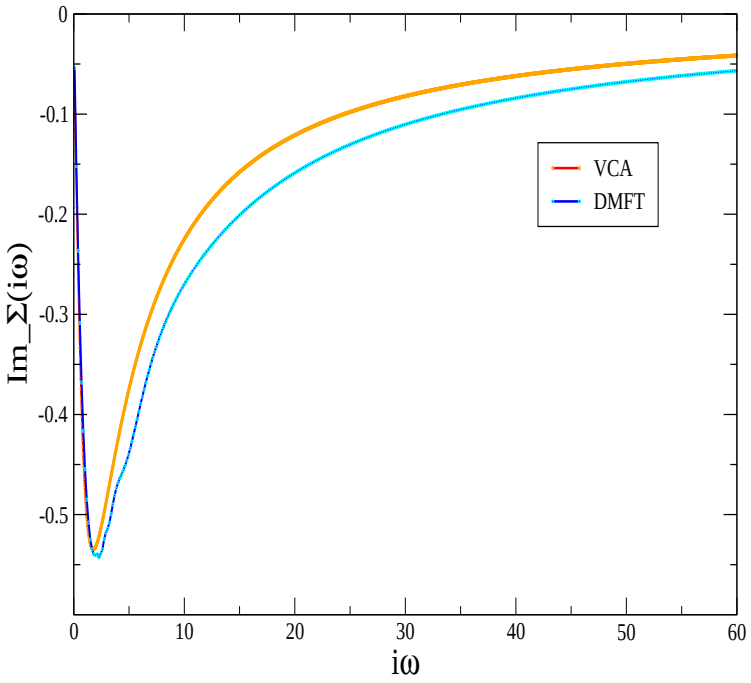

Figure 6.9: The comparison of imaginary part of self-energy on the Matsubara axis $Im\Sigma(i\omega)$ obtained from VCA and DMFT calculations for the $t2g$ bands. The parameters necessary for this analysis are fixed to the following values: $U = 4.0\ eV$, $J = 0.6\ eV$. For the VCA calculation the reference system with 3 orbitals + 3 bath sites is used.

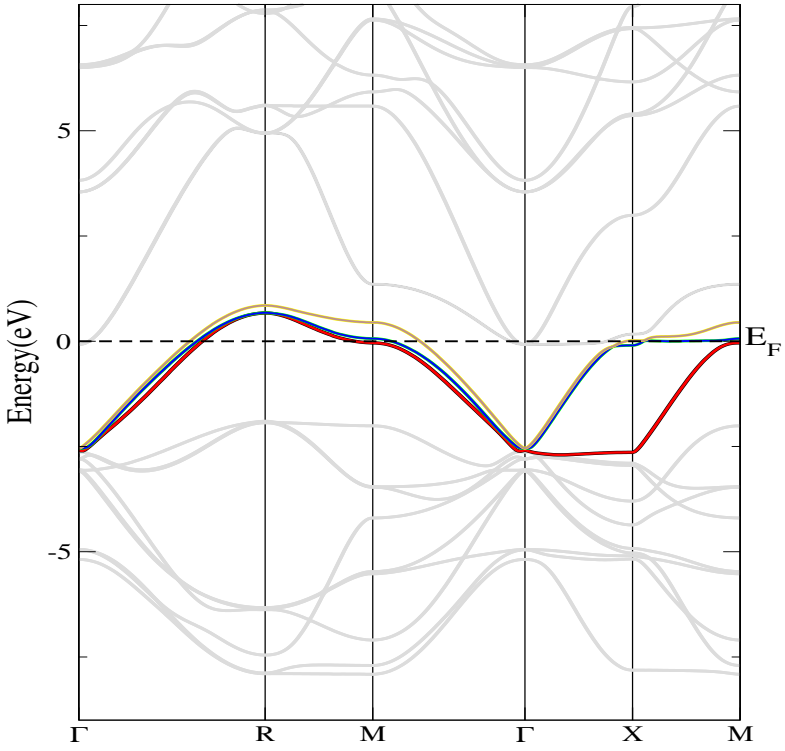

Figure 6.10: Band structure of $SrRuO_3$ compound obtained from DFT package Wien2k based on linearized augmented plane waves[103]. The colorful thick solid lines around and on the Fermi level are $t2g$ bands.

6.4 Results for $SrRuO_3$

$SrRuO_3$ is the next compound we want to study within the method LDA+VCA. It has a large spin orbit coupling which is defined as the interaction of the spin-magnetic moment with the magnetic field induced by its own orbital motion. But first, let us consider some general properties of this compound. $SrRuO_3$ belongs to the class of ruthenates. It exhibits a orthorhombic perovskite structure with a bad metal behaviour at high temperatures and a Fermi liquid like behaviour at low temperatures[114].

Photoemission studies show that the physical properties of the ruthenates or ruthenium oxide series are effected by the electronic correlations. Here we can again construct an effective model from $t2g$ orbitals. There is a large spin-orbit coupling of the ruthenium ion therefore one has to take into account this effect. Therefore we have to do a spin polarized calculation where the spin-up and spin-down states are calculated separately and spin-orbit coupling mixes the spin up and spin down states. This leads to splitting of the electronic bands in the band structure picture as shown in figure 6.10. The next

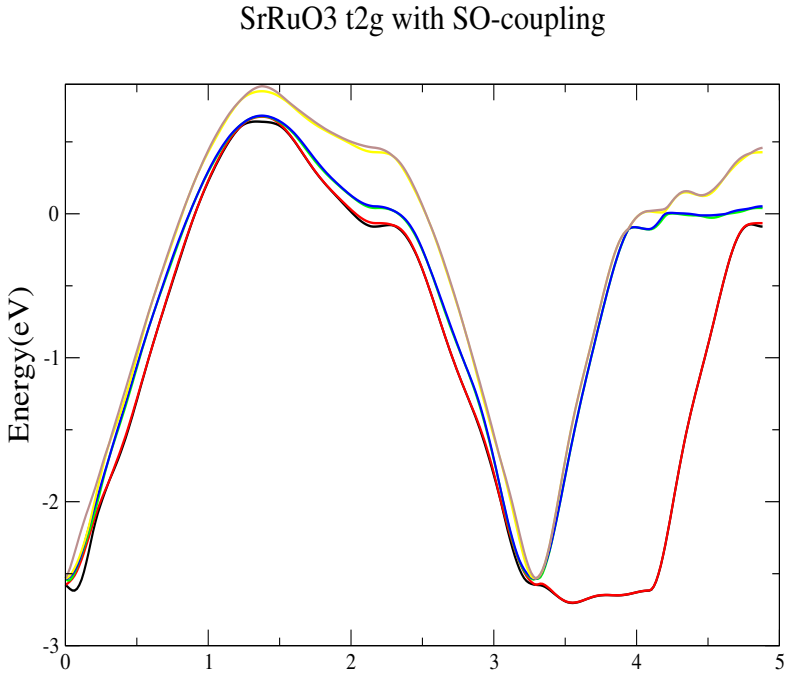

Figure 6.11: Kinetic part parametrization of t2g orbitals obtained from the Wannier construction. These values are used for the generation of the one-particle effective Hamiltonian. These bands are obtained by the Fourier transformation of this Hamiltonian.

step is the construction of the effective one-particle Hamiltonian

$$H_{eff} = \sum_{ij\alpha\beta\sigma\sigma'} t^{\sigma\sigma'}_{i\alpha,j\beta} c^{\dagger}_{i\alpha\sigma} c_{j\beta\sigma'}, \tag{6.6}$$

which is not spin diagonal because spin-orbit coupling mixes the spin-up and spin-down states. The diagonalization of this effective Hamiltonian results in the LDA band structure as shown in figure 6.11, where the small deviations (fluctuations) from the LDA results come due to the small k-mesh and due to the non-optimized selection of the energy window.

In the next step this effective Hamiltonian is supplemented by the Coulomb interaction term and the corresponding results are shown in figure 6.12.

As like the $SrVO_3$ we start again with the check of the LDA result in figure 6.12 (a) for the non-interacting limit, where the emergence of the peaked structure comes from the non-optimization of the Wannier calculation, which can be removed by variation of the energy window and by an increase of the k-mesh. But beside these small deviations the result agrees with the LDA result. For the interacting case without bath sites the 1 site (3 orbitals with orbital splitting) reference system as shown in figure 6.12 (b) deliver metallic solutions due to the spin-orbit coupling which was not the case for the

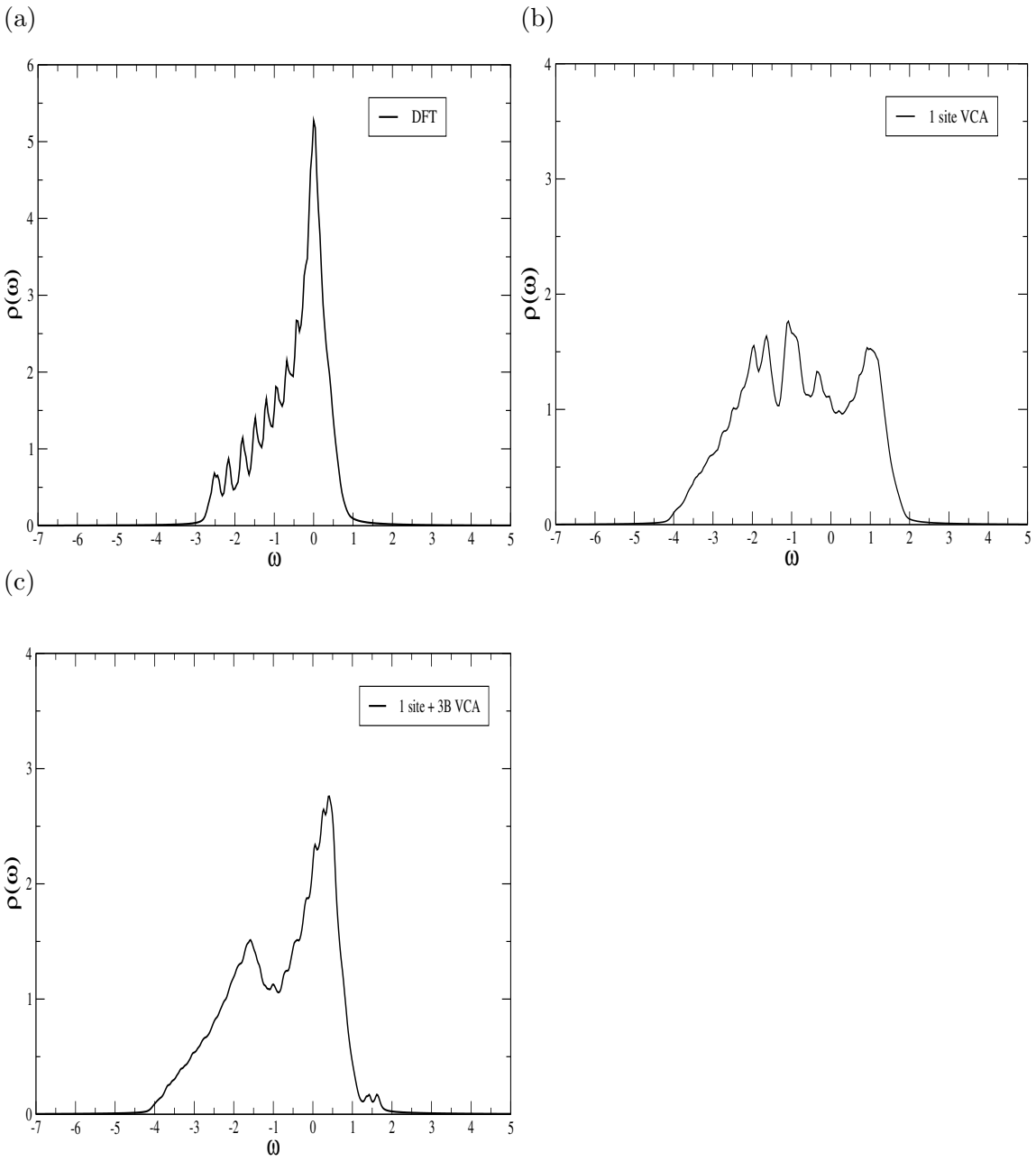

Figure 6.12: Density of states for t2g orbitals of $SrRuO_3$ for different clusters without bath sites. The values of parameters Hubbard U and Hund's coupling: (a) $U = 0.0$, $J = 0.0$, it is exact for all clusters. (b)-(c) $U = 2.8\,eV$, $J = 0.4\,eV$. Used reference systems: (b) 1 site (3 orbitals with orbital splitting) clusters, (c) 1 site clusters with 3 additional bath sites.

$SrVO_3$. But still the finite size effects are supposed to be strong. Again we can improve the results by bath sites which induce a noticeable improvement of finite size effects as shown in figure 6.12 (c), where a three peak structure is obtained. Also the consideration of effective mass ($m^* \approx 1.15$) for this compound $SrRuO_3$ gives decreased values compared to the layered structure Sr_2RuO_4, which coincides with the experimental measurements.

6.5 Summary

Here we have considered a possible combination of VCA and LDA for the application on the multi-orbital correlated materials in analogy to the LDA+DMFT method. For the downfolding we used Wien2Wannier90 and Wannier90, which is inducing the maximally localized Wannier functions by exploiting the gauge freedom in the definition of the Wannier functions. Using this one can generate an effective Hamiltonian which is supplemented by a Coulomb term for the electronic correlations. Through this way a minimal model for the correlated bands can be generated. As a benchmark we used the material $SrVO_3$ where a three band Hubbard Hamiltonian like system can be generated. This model is solved within VCA method. The results for this material show a good agreement with the LDA+DFMT method and experimental results.

This method can be applied to the material like $SrRuO_3$, where spin orbit coupling is an important quantity and brings a spitting of the orbitals. Therefore one has to perform a spin polarized LDA calculation which brings a doubling of the electronic bands. The results show us that the spin-orbit coupling gives us more smooth results and helps us to reach for the smaller systems, e.g., 1 site cluster to get into the metallic phase.

7 CONCLUSIONS AND OUTLOOK

Correlations at different length scales are important for a proper description of many materials, therefore their study is important from the aspect fundamental research and from the view of the of the technological applications.

We analyzed the spatial correlation dependency of the Hubbard model, which is the simplest model for the standard correlation physics as a function of dimensionality and cluster shape geometry. In the Hubbard model the dimensionality suppresses more and more the non-local correlations and the weight of the local correlations increases. This is obvious for instance, at distance 1 lattice site the measure drops to around 0.75 in $1D$, to 0.55 in $2D$, and to 0.4 in 3D. Even in $3D$, non-local correlations cannot be neglected completely. But compared to $1D$, short-length scales obviously capture the relevant physics much better in higher dimensions.

Also the study of Mott-Hubbard metal-insulator transition of two dimensional Hubbard model with regard to non-local correlations display the importance of the correlations. The results which include short range correlations deliver a finite critical interaction U_C for the (metastable) paramagnetic phase. On the other hand the results where long range correlations are included, indicate that for all finite $U > 0$ at low temperature T the model is a paramagnetic insulator because of the strong extended antiferromagnetic fluctuations (paramagnons). These fluctuations gradually show an evolution from a Slater-like behaviour to a Heisenberg-like behaviour, which is similar to the evolution for the $T = 0$ antiferromagnet. The critical interaction U_C is shifted to the value $U_C = 0$. The inclusion of the frustration turns down this scenario. It shifts the vanishing critical interaction $U_C = 0$ towards finite values which ends into a quantum critical point.

After the study of the correlation within the Hubbard model we go over to the real material calculations. Therefore we have considered a possible combination of VCA and LDA for the application on the multi-orbital correlated materials in analogy to the LDA+DMFT method. For the downfolding we used Wien2Wannier90 and Wannier90, which is inducing the maximally localized Wannier functions by exploiting the gauge freedom in the definition of the Wannier functions. Using this one can generate an effective Hamiltonian, which is supplemented by a Coulomb term for the electronic correlations. Through this way a minimal model for the correlated bands can be generated. As a benchmark we used the material $SrVO_3$ where a three band Hubbard Hamiltonian like system can be generated. This model is solved within VCA method. The results for this material for the effective mass m^* is in good agreement with the LDA+DFMT method and experimental results.

This method can be applied to the material like $SrRuO_3$, where spin orbit coupling is an important quantity. Therefore one has to perform a spin polarized LDA calculation

which brings a doubling of the electronic bands.

Finally we comment that the analytical and numerical efforts for the study of strongly correlated electronic systems lead to a significant progress in this area. But still there is still a lot to be done. The research in this area is significant for many reasons. Beside the technological applications it helps to get a more clear understanding progress in the fundamental research and in the understanding of collective aspects.

8 Appendix

8.1 AppendixA:

8.1.1 Atomic units

In atomic units the central atomic constants

elementary charge: e
mass of electron : m_e
Planck Constant: $\hbar$
Dielectric constant ϵ_0

have the following value

$$e = m_e = \hbar = \frac{1}{4\pi\epsilon_0} = 1 \tag{8.1}$$

8.1.2 Theta function

The so-called theta function or step function is defined by

$$\Theta(t) = \left\{ \begin{array}{lll} 1 & \text{for} & t > 0 \\ 0 & \text{for} & t < 0 \end{array} \right\} \tag{8.2}$$

8.1.3 Time ordering operator

Time ordering operator for real time is defined by

$$\mathcal{T}\left[A(t_1)B(t_2)\right] = \left\{ \begin{array}{lll} A(t_1)B(t_2) & \text{if} & t_1 > t_2 \\ B(t_2)A(t_1) & \text{if} & t_1 < t_2 \end{array} \right\} \tag{8.3}$$

and for the imaginary time $i\tau$ is defined in the analogous manner

$$\mathcal{T}_\tau\left[A(\tau_1)B(\tau_2)\right] = \left\{ \begin{array}{lll} A(\tau_1)B(\tau_2) & \text{if} & \tau_1 > \tau_2 \\ B(\tau_2)A(\tau_1) & \text{if} & \tau_1 < \tau_2 \end{array} \right\} \tag{8.4}$$

8.1.4 time evolution operator

Definition:

$$|\psi(t)\rangle = U(t, t_0)|\psi(t_0)\rangle \tag{8.5}$$

It evolutes a state from time t_0 to the time t. $U(t,t_0)$ is an unitarian operator and fulfills the boundary condition $U(t,t_0)=1$. Now we are interested in a compact form for U therefore the following differential equation which defines the time evolution operator has to be solved

$$\frac{\partial}{\partial t}U(t,t_0) = -\frac{i}{\hbar}V(t)U(t,t_0) \tag{8.6}$$

By integration we obtain

$$U(t,t_0) = 1 + \frac{1}{i}\int_{t_0}^{t} V(t')U(t',t_0)dt' \tag{8.7}$$

This integral equation can be solved iteratively

$$U(t,t_0) = 1 + \frac{1}{i}\int_{t_0}^{t} V(t_1)dt_1 + \frac{1}{i^2}\int_{t_0}^{t} V(t_1)dt_1\int_{t_0}^{t_1} V(t_2)dt_2 + \cdots \tag{8.8}$$

From this result we can obtain a compact expression by using the time ordering operator $\mathcal{T}$. Let us show how the third term can be rewritten

$$\begin{aligned}
\int_{t_0}^{t} V(t_1)dt_1\int_{t_0}^{t_1} V(t_2)dt_2 &= \frac{1}{2}\int_{t_0}^{t} V(t_1)dt_1\int_{t_0}^{t_1} V(t_2)dt_2 + \frac{1}{2}\int_{t_0}^{t} V(t_2)dt_2\int_{t_0}^{t_2} V(t_1)dt_1 \\
&= \frac{1}{2}\int_{t_0}^{t} dt_1\int_{t_0}^{t_1} dt_2 V(t_1)V(t_2)\theta(t_1-t_2) \\
&+ \frac{1}{2}\int_{t_0}^{t} dt_2\int_{t_0}^{t_2} dt_2 V(t_2)V(t_1)\theta(t_2-t_1) \\
&= \frac{1}{2}\int_{t_0}^{t} dt_1\int_{t_0}^{t} dt_2 \left[V(t_1)V(t_2)\theta(t_1-t_2) + V(t_2)V(t_1)\theta(t_2-t_1)\right] \\
&= \frac{1}{2}\int_{t_0}^{t} dt_1\int_{t_0}^{t} dt\mathcal{T}\left[V(t_1)V(t_2)\right]
\end{aligned}$$

This expression can be easily generalized to higher order terms and finally the following compact form

$$\begin{aligned}
U(t,t_0) &= \sum_{n=0}^{\infty}\frac{1}{n!}\left(\frac{1}{i}\right)^n\int_{t_0}^{t} dt_1\cdots\int_{t_0}^{t} dt_n\mathcal{T}\left[V(t_1)\cdots V(t_n)\right] \\
&= \mathcal{T}\left[e^{-i\int_{t_0}^{t} dt' V(t')}\right]
\end{aligned} \tag{8.9}$$

8.2 AppendixB: Spread or delocalization functional

From the Bloch functions $\psi_{n\mathbf{k}}$ i.e. LAPW(linear augmented plane wave) Bloch functions general Wannier functions of a band n at site $\vec{R}_0$ can be constructed

$$w_n(\mathbf{r}-\mathbf{R}_0) = \frac{1}{N}\sum_{\mathbf{k}} e^{i\mathbf{k}.\mathbf{R_0}}e^{i\phi_n(\mathbf{k})}\psi_{n\mathbf{k}}, \tag{8.10}$$

where the arbitrary phase $\phi_n(\mathbf{k})$ have to be determined to reach some level of localization around the point R_0. The first choice in such a case is to take the average square radius

$$\langle r^2 \rangle_{ave} = \int r^2 |w_n(\mathbf{r})|^2 d\mathbf{r}. \tag{8.11}$$

The average square radius is not invariant under the transformation of the phase $\phi_n(\mathbf{k})$, therefore the phases can be used to derive a differential equation[115] to reach the minimal value of the average square radius, which has to be fulfilled at every $\mathbf{k}$ vector

$$\nabla_{\mathbf{k}} \int u^*_{n\mathbf{k}}(\mathbf{r}) i \nabla_{\mathbf{k}} u_{n\mathbf{k}}(\mathbf{r}) d\mathbf{r} = 0. \tag{8.12}$$

This procedure can be optimized and rewritten for a set of orbitals which are described by general Wannier functions

$$w_n(\mathbf{r} - \mathbf{R}) = \frac{V}{(2\pi)^3} \int_{BZ} \left(\sum_m U^{(\mathbf{k})}_{mn} u_{n\mathbf{k}}(\mathbf{r}) \right) exp(i\mathbf{k}.\mathbf{r}) d\mathbf{k}, \tag{8.13}$$

where $U^{(\mathbf{k})}_{mn}$ are unitary matrices which mix the bands at wave vector $\mathbf{k}$. These unitary matrix have to be determined For this purpose equivalently a similar expression like the average square radius can be written. This expression is to the second moment of the corresponding Wannier functions and is defined delocalization functional

$$\Omega_{deloc} = \langle r^2 \rangle - \langle \vec{r} \rangle^2. \tag{8.14}$$

Here for clearness we introduce the following notation for the Wannier functions at the position $\mathbf{R}$

$$w_n(\mathbf{r} - \mathbf{R}) = |\mathbf{R}n\rangle. \tag{8.15}$$

The delocalization functional in these notation looks like

$$\Omega_{deloc} = \sum_n \left(\langle \mathbf{0}n | r^2 | \mathbf{0}n \rangle - \langle \mathbf{0}n | \mathbf{r} | \mathbf{0}n \rangle^2 \right). \tag{8.16}$$

This functional can be rewritten by adding and subtracting off-diagonal term

$$\tilde{\Omega} = \sum_n \sum_{\vec{R}n \neq \vec{0}n} |\langle \mathbf{R}m | r | \mathbf{0}n \rangle|^2. \tag{8.17}$$

Hence using this term the delocalization functional can be decomposed in the following terms

$$\begin{aligned} \Omega_{deloc} &= \Omega_I + \tilde{\Omega} \\ &= \Omega_I + \Omega_D + \Omega_{OD}, \end{aligned} \tag{8.18}$$

where

$$\tilde{\Omega} = \sum_n \left[\langle \mathbf{0}n|r^2|\mathbf{0}n\rangle - \sum_{\mathbf{R}m} |\langle \mathbf{R}m|r|\mathbf{0}n\rangle|^2 \right],$$

$$\Omega_D = \sum_n \sum_{\vec{R}\neq\mathbf{0}} |\langle \mathbf{R}n|r|\mathbf{0}n\rangle|^2,$$

$$\Omega_{OD} = \sum_{m\neq n} \sum_{\mathbf{R}} |\langle \mathbf{R}m|r|\mathbf{0}n\rangle|^2.$$

We can use (7.3) to write these matrix elements in the Fourier space as

$$\langle \mathbf{R}n|\mathbf{r}|\mathbf{0}n\rangle = i\frac{V}{(2\pi)^3}\int d\mathbf{k} e^{i\mathbf{k}\mathbf{R}} \langle u_{n\mathbf{k}}|\nabla_{\mathbf{k}}|u_{n\mathbf{k}}\rangle \tag{8.19}$$

$$\langle \mathbf{R}n|r^2|\mathbf{0}n\rangle = -\frac{V}{(2\pi)^3}\int d\mathbf{k} e^{i\mathbf{k}\mathbf{R}} \langle u_{n\mathbf{k}}|\nabla^2_{\mathbf{k}}|u_{n\mathbf{k}}\rangle. \tag{8.20}$$

These expressions have two major advantages. They allow us to calculate the affects of any unitary transformation on the localization behaviour of the delocalization functional because we have a direct relation to Bloch functions and we do not have to recalculate expensive scalar products. For the calculation of some numerical values for these terms we need Bloch functions defined on a mesh of $\mathbf{k}$ vectors. Now one can calculate the gradient on this $\mathbf{k}$ mesh using the following discretization schemes for any smooth function $f(\mathbf{x})$

$$\nabla f(\mathbf{x}) = \sum_{\mathbf{b}} w_b \mathbf{b} \left[f(\mathbf{x}+\mathbf{b}) - f(\mathbf{x}) \right] \tag{8.21}$$

$$|\nabla f(\mathbf{x})|^2 = \sum_{\mathbf{b}} w_b \mathbf{b} \left[f(\mathbf{x}+\mathbf{b}) - f(\mathbf{x}) \right]^2 \tag{8.22}$$

to solve the expressions $(7.10) - (7.11)$. The quantity $\mathbf{b}$ corresponds to a vector which is connecting to neighboring $\mathbf{k}$ vectors and w_b is the weight which depends on number of neighbors in the unit cell. After some calculation and some algebra we obtain following expressions for the delocalization functional

$$\langle \mathbf{r} \rangle_n = \frac{1}{N} \sum_{\mathbf{k},\mathbf{b}} w_b . \mathbf{b} . ln M^{(\mathbf{k},\mathbf{b})}_{n,n}, \tag{8.23}$$

$$\langle r^2 \rangle_n = \frac{1}{N} \sum_{\mathbf{k},\mathbf{b}} w_b \left(\left[1 - |M^{(\mathbf{k},\mathbf{b})}_{n,n}|^2 \right] + \left[Im ln M^{(\mathbf{k},\mathbf{b})}_{n,n} \right] \right), \tag{8.24}$$

$$\Omega_I = \frac{1}{N}\sum_{\mathbf{k},\mathbf{b}} w_b \left(N_{bands} - \sum_{m,n} |M_{n,n}^{(\mathbf{k},\mathbf{b})}|^2 \right), \tag{8.25}$$

$$\Omega_{OD} = \frac{1}{N}\sum_{\mathbf{k},\mathbf{b}} w_b \sum_{m\neq n} |M_{n,n}^{(\mathbf{k},\mathbf{b})}|^2, \tag{8.26}$$

$$\Omega_D = \frac{1}{N}\sum_{\mathbf{k},\mathbf{b}} w_b \sum_{n} \left[-Im ln M_{n,n}^{(\mathbf{k},\mathbf{b})} - \mathbf{b}.\langle r \rangle_n \right]^2. \tag{8.27}$$

Obviously for the terms which are necessary to obtain the delocalization functional the only quantities of interest are the matrix elements between the lattice periodic part of Bloch orbitals at neighboring $\mathbf{k}$ vectors[116]:

$$M_{n,n}^{(\mathbf{k},\mathbf{b})} = \langle u_{m\mathbf{k}} | u_{n,\mathbf{k}+\mathbf{b}} \rangle. \tag{8.28}$$

Bibliography

[1] P. Hohenberg and W. Kohn, "Inhomogeneous electron gas," *Phys. Rev.* **136** (1964) B864–B871.

[2] W. Kohn and L. J. Sham, "Self-consistent equations including exchange and correlation effects," *Phys. Rev.* **140** (1965) A1133–A1138.

[3] J. P. Perdew, K. Burke, and Y. Wang, "Generalized gradient approximation for the exchange-correlation hole of a many-electron system," *Phys. Rev. B* **54** (1996) 16533–16539.

[4] J. Bednorz and K. Müller, "Possible hightc superconductivity in the Ba−La−Cu−O system," *Zeitschrift für Physik B Condensed Matter* **64** (1986) 189–193.

[5] Y. Kamihara, T. Watanabe, M. Hirano, and H. Hosono, "Iron-based layered superconductor La[O1−xFx]FeAs (x = 0.05−0.12) with tc = 26 k," *Journal of the American Chemical Society* **130** (2008) 3296–3297.

[6] W. Metzner and D. Vollhardt, "Correlated lattice fermions in $d = \infty$ dimensions," *Phys. Rev. Lett.* **62** (1989) 324–327.

[7] A. Georges and G. Kotliar, "Hubbard model in infinite dimensions," *Phys. Rev. B* **45** (1992) 6479–6483.

[8] G. Kotliar, S. Y. Savrasov, G. Pálsson, and G. Biroli, "Cellular dynamical mean field approach to strongly correlated systems," *Phys. Rev. Lett.* **87** (2001) 186401.

[9] G. Biroli, O. Parcollet, and G. Kotliar, "Cluster dynamical mean-field theories: Causality and classical limit," *Phys. Rev. B* **69** (2004) 205108.

[10] M. H. Hettler, A. N. Tahvildar-Zadeh, M. Jarrell, T. Pruschke, and H. R. Krishnamurthy, "Nonlocal dynamical correlations of strongly interacting electron systems," *Phys. Rev. B* **58** (1998) R7475–R7479.

[11] C. Gros and R. Valentí, "Cluster expansion for the self-energy: A simple many-body method for interpreting the photoemission spectra of correlated fermi systems," *Phys. Rev. B* **48** (1993) 418–425.

[12] D. Sénéchal, D. Perez, and M. Pioro-Ladrière, "Spectral weight of the hubbard model through cluster perturbation theory," *Phys. Rev. Lett.* **84** (2000) 522–525.

[13] C. Dahnken, M. Aichhorn, W. Hanke, E. Arrigoni, and M. Potthoff, "Variational cluster approach to spontaneous symmetry breaking: The itinerant antiferromagnet in two dimensions," *Phys. Rev. B* **70** (2004) 245110.

[14] A. Toschi, A. A. Katanin, and K. Held, "Dynamical vertex approximation: A step beyond dynamical mean-field theory," *Phys. Rev. B* **75** (2007) 045118.

[15] Potthoff, M., "Self-energy-functional approach to systems of correlated electrons," *Eur. Phys. J. B* **32** (2003) 429–436.

[16] V. I. Anisimov, A. I. Poteryaev, M. A. Korotin, A. O. Anokhin, and G. Kotliar, "First-principles calculations of the electronic structure and spectra of strongly correlated systems: dynamical mean-field theory," *Journal of Physics: Condensed Matter* **9** (1997) 7359.

[17] A. I. Lichtenstein and M. I. Katsnelson, " ***Ab initio*** calculations of quasiparticle band structure in correlated systems: Lda++ approach," *Phys. Rev. B* **57** (1998) 6884–6895.

[18] G. Kotliar, S. Y. Savrasov, K. Haule, V. S. Oudovenko, O. Parcollet, and C. A. Marianetti, "Electronic structure calculations with dynamical mean-field theory," *Rev. Mod. Phys.* **78** (2006) 865–951.

[19] K. Held, I. A. Nekrasov, G. Keller, V. Eyert, N. Blümer, A. K. McMahan, R. T. Scalettar, T. Pruschke, V. I. Anisimov, and D. Vollhardt, "Realistic investigations of correlated electron systems with LDA + DMFT," *Physica Status Solidi (b)* **243** (2006) 2599–2631.

[20] T. Schäfer, F. Geles, D. Rost, G. Rohringer, E. Arrigoni, K. Held, N. Blümer, M. Aichhorn, and A. Toschi, "Fate of the false mott-hubbard transition in two dimensions," *Phys. Rev. B* **91** (2015) 125109.

[21] R. Blankenbecler, D. J. Scalapino, and R. L. Sugar, "Monte carlo calculations of coupled boson-fermion systems. i," *Phys. Rev. D* **24** (1981) 2278–2286.

[22] D. Rost, F. Assaad, and N. Blümer, "Quasi-continuous-time impurity solver for the dynamical mean-field theory with linear scaling in the inverse temperature," *Phys. Rev. E* **87** (2013) 053305.

[23] A. I. Liechtenstein, V. I. Anisimov, and J. Zaanen, "Density-functional theory and strong interactions: Orbital ordering in mott-hubbard insulators," *Phys. Rev. B* **52** (1995) R5467–R5470.

[24] J. Hubbard, "Electron correlations in narrow energy bands," *Proceedings of the Royal Society of London* **276** (1963) 238–257.

[25] M. C. Gutzwiller, "Effect of correlation on the ferromagnetism of transition metals," *Phys. Rev. Lett.* **10** (1963) 159–162.

[26] J. Kanamori, "Electron correlation and ferromagnetism of transition metals," *Prog. Theor. Phys.* **30** (1963) 275–289.

[27] N. W. Ashkroft and N. D. Mermin, *Solid state physics*. Holt Rinehart & Winston, 2002.

[28] O. Madelung, *Introduction to the solid state theory*. Springer Verlag Berlin Heidelberg New York, 1996.

[29] H. Bruus and K. Flensberg, *Many-body quantum theory in condensed matter physics*. Oxford Graduate Texts, 2002.

[30] A. Honecker, "Scriptum zur vorlesung, vielteilchentheorie des festkörpers." 2007.

[31] A. Georges, "Strongly correlated electron materials: Dynamical mean−field theory and electronic structure," *AIP Conference Proceedings* **715** (2004) 3–74.

[32] G. Kotliar and G. Vollhardt, "Strongly correlated materials: Insights from dynamical mean-field theory," *Phys. Today* **57** (2004) 53–59.

[33] T. Giamarchi, *Quantum Physics in One Dimension*. Oxford University Press, 2004.

[34] D. Scalapino, "The case for dx2 − y2 pairing in the cuprate superconductors," *Physics Reports* **250** (1995) 329–365.

[35] J. Schäfer, M. Hoinkis, E. Rotenberg, P. Blaha, and R. Claessen, "Fermi surface and electron correlation effects of ferromagnetic iron," *Phys. Rev. B* **72** (2005) 155115.

[36] A. N. Rubtsov, M. I. Katsnelson, and A. I. Lichtenstein, "Dual fermion approach to nonlocal correlations in the hubbard model," *Phys. Rev. B* **77** (2008) 033101.

[37] E. H. Lieb and F. Y. Wu, "Absence of mott transition in an exact solution of the short-range, one-band model in one dimension," *Phys. Rev. Lett.* **20** (1968) 1445–1448.

[38] S. R. White, "Density matrix formulation for quantum renormalization groups," *Phys. Rev. Lett.* **69** (1992) 2863–2866.

[39] U. Schollwöck, "The density-matrix renormalization group in the age of matrix product states," *Annals of Physics* **326** (2011) 96–192.

[40] G. Czycholl, *Theoretische Festkörperphysik*. Vieweg, 2000.

[41] C. Lanczos, "An iteration method for the solution of the eigenvalue problem of linear differential and integral operators," *Res. Nat. Bur. Standards* **45** (1950) 255–282.

[42] A. Ruhe, "Implementation aspects of band lanczos algorithms for computation of eigenvalues of large sparse symmetric matrices," *Math. Comp.* **33** (1979) 680–687.

[43] M. Aichhorn, E. Arrigoni, M. Potthoff, and W. Hanke, "Variational cluster approach to the hubbard model: Phase-separation tendency and finite-size effects," *Phys. Rev. B* **74** (2006) 235117.

[44] S. Pairault, D. Sénéchal, and A.-M. S. Tremblay, "Strong-coupling expansion for the hubbard model," *Phys. Rev. Lett.* **80** (1998) 5389–5392.

[45] S. Pairault, D. Sénéchal, and A.-M. Tremblay, "Strong-coupling perturbation theory of the hubbard model," *The European Physical Journal B - Condensed Matter and Complex Systems* **16** (2000) 85–105.

[46] M. Potthoff, "Self-energy-functional theory," in *Strongly Correlated Systems*, A. Avella and F. Mancini, eds., vol. 171 of *Springer Series in Solid-State Sciences*, pp. 303–339. Springer Berlin Heidelberg, 2012.

[47] J. M. Luttinger and J. C. Ward, "Ground-state energy of a many-fermion system. ii," *Phys. Rev.* **118** (1960) 1417–1427.

[48] R. Eder, "The variational cluster approximation," in *Emergent Phenomena in Correlated Matter*, A. Avella, E. Mancini, Ferdinando Pavarini, E. Koch, and U. Schollwöck, eds., vol. 3 of *Schriften des Forschungszentrums Jülich Reihe Modeling and Simulation*. Forschungszentrum Jülich GmbH Institute for Advanced Simulation, 2014.

[49] D. Sénéchal, "An introduction to quantum cluster methods," *Lectures given at the CIFAR - PITP International Summer School on Numerical Methods for Correlated Systems in Condensed Matter, Sherbrooke, Canada, May 26 - June 6* (2008) .

[50] K. Held, A. A. Katanin, and A. Toschi, "Dynamical vertex approximation – an introduction," *Prog. Theor. Phys. Suppl.* **176** (2008) 117.

[51] J. A. Bychkov, L. P. Gorkov, and I. E. Dzyaloshinskii, "Possibility of superconductivity type phenomena in a one-dimensional system," *J. Exptl. Theoret. Phys.* **50** (1966) 738–758.

[52] N. E. Bickers and S. R. White, "Conserving approximations for strongly fluctuating electron systems. ii. numerical results and parquet extension," *Phys. Rev. B* **43** (1991) 8044–8064.

[53] V. Janiš, "Stability of self-consistent solutions for the hubbard model at intermediate and strong coupling," *Phys. Rev. B* **60** (1999) 11345–11360.

[54] J. P. Perdew and A. Zunger, "Self-interaction correction to density-functional approximations for many-electron systems," *Phys. Rev. B* **23** (1981) 5048–5079.

[55] D. M. Ceperley and B. J. Alder, "Ground state of the electron gas by a stochastic method," *Phys. Rev. Lett.* **45** (1980) 566–569.

[56] V. I. Anisimov and O. Gunnarsson, "Density-functional calculation of effective coulomb interactions in metals," *Phys. Rev. B* **43** (1991) 7570–7574.

[57] J. F. Janak, "Proof that $\frac{\partial e}{\partial n_i} = \epsilon$ in density-functional theory," *Phys. Rev. B* **18** (1978) 7165–7168.

[58] N. Marzari and D. Vanderbilt, "Maximally localized generalized wannier functions for composite energy bands," *Phys. Rev. B* **56** (1997) 12847–12865.

[59] I. Souza, N. Marzari, and D. Vanderbilt, "Maximally localized wannier functions for entangled energy bands," *Phys. Rev. B* **65** (2001) 035109.

[60] A. Fujimori, I. Hase, H. Namatame, Y. Fujishima, Y. Tokura, H. Eisaki, S. Uchida, K. Takegahara, and F. M. F. de Groot, "Evolution of the spectral function in mott-hubbard systems with d^1 configuration," *Phys. Rev. Lett.* **69** (1992) 1796–1799.

[61] V. I. Anisimov, A. I. Poteryaev, M. A. Korotin, A. O. Anokhin, and G. Kotliar, "First-principles calculations of the electronic structure and spectra of strongly correlated systems: dynamical mean-field theory," *Journal of Physics: Condensed Matter* **9** (1997) 7359.

[62] E. Pavarini, S. Biermann, A. Poteryaev, A. I. Lichtenstein, A. Georges, and O. K. Andersen, "Mott transition and suppression of orbital fluctuations in orthorhombic $3d^1$ perovskites," *Phys. Rev. Lett.* **92** (2004) 176403.

[63] M. Aichhorn, L. Pourovskii, V. Vildosola, M. Ferrero, O. Parcollet, T. Miyake, A. Georges, and S. Biermann, "Dynamical mean-field theory within an augmented plane-wave framework: Assessing electronic correlations in the iron pnictide lafeaso," *Phys. Rev. B* **80** (2009) 085101.

[64] V. I. Anisimov, I. V. Solovyev, M. A. Korotin, M. T. Czyżyk, and G. A. Sawatzky, "Density-functional theory and nio photoemission spectra," *Phys. Rev. B* **48** (1993) 16929–16934.

[65] F. M. F. de Groot, J. C. Fuggle, B. T. Thole, and G. A. Sawatzky, "2 p x-ray absorption of 3 d transition-metal compounds: An atomic multiplet description including the crystal field," *Phys. Rev. B* **42** (1990) 5459–5468.

[66] L. de' Medici, "Hund's coupling and its key role in tuning multiorbital correlations," *Phys. Rev. B* **83** (2011) 205112.

[67] O. Gunnarsson, O. K. Andersen, O. Jepsen, and J. Zaanen, "Density-functional calculation of the parameters in the anderson model: Application to mn in cdte," *Phys. Rev. B* **39** (1989) 1708–1722.

[68] O. Gunnarsson, "Calculation of parameters in model hamiltonians," *Phys. Rev. B* **41** (1990) 514–518.

[69] F. Aryasetiawan, M. Imada, A. Georges, G. Kotliar, S. Biermann, and A. I. Lichtenstein, "Frequency-dependent local interactions and low-energy effective models from electronic structure calculations," *Phys. Rev. B* **70** (2004) 195104.

[70] T. Maier, M. Jarrell, T. Pruschke, and M. H. Hettler, "Quantum cluster theories," *Rev. Mod. Phys.* **77** (2005) 1027–1080.

[71] I. E. Dzyaloshinskii, "Extended van-hove singularity and related non-fermi liquids," *J. Phys. I* **6** (1996) 119–135.

[72] J. E. Hirsch, "Two-dimensional hubbard model: Numerical simulation study," *Phys. Rev. B* **31** (1985) 4403–4419.

[73] N. F. MOTT, "Metal-insulator transition," *Rev. Mod. Phys.* **40** (1968) 677–683.

[74] X. Y. Zhang, M. J. Rozenberg, and G. Kotliar, "Mott transition in the $d = \infty$ hubbard model at zero temperature," *Phys. Rev. Lett.* **70** (1993) 1666–1669.

[75] K. Kawakami, T. Usuki, and A. Okiji, "Thermodynamic properties of the one-dimensional hubbard model," *Phys. Lett. A* **137** (1989) 287–290.

[76] F. H. L. Essler, H. Frahm, F. Göhmann, A. Klümper, and V. E. Korepin, *The One-Dimensional Hubbard Model*. Cambridge University Press, Cambridge, 2005.

[77] A. Georges and W. Krauth, "Physical properties of the half-filled hubbard model in infinite dimensions," *Phys. Rev. B* **48** (1993) 7167–7182.

[78] S. Fuchs, E. Gull, L. Pollet, E. Burovski, E. Kozik, T. Pruschke, and M. Troyer, "Thermodynamics of the 3d hubbard model on approaching the néel transition," *Phys. Rev. Lett.* **106** (2011) 030401.

[79] D. B. McWhan, J. P. Remeika, T. M. Rice, W. F. Brinkman, J. P. Maita, and A. Menth, "Electronic specific heat of metallic ti-doped v_2o_3," *Phys. Rev. Lett.* **27** (1971) 941–943.

[80] P. Hansmann, A. Toschi, G. Sangiovanni, T. Saha-Dasgupta, S. Lupi, M. Marsi, and K. Held, "Mott-hubbard transition in v2o3 revisited," *Phys. Status Solidi B* **250** (2013) 1251–1264.

[81] C. Castellani, C. D. Castro, D. Feinberg, and J. Ranninger, "New model hamiltonian for the metal-insulator transition," *Phys. Rev. Lett.* **43** (1979) 1957–1960.

[82] M. Vekić and S. R. White, "Pseudogap formation in the half-filled hubbard model," *Phys. Rev. B* **47** (1993) 1160–1163.

[83] F. Mancini, "The mott-hubbard transition and the paramagnetic insulating state in the two-dimensional hubbard model," *Eur. Phys. Lett.* **50** (2000) 229–235.

[84] J. M. Vilk and A.-M. S. Tremblay, "Destruction of fermi-liquid quasiparticles in two dimensions by critical fluctuations," *Eur. Phys. Lett.* **33** (1997) 159–164.

[85] H. Park, K. Haule, and G. Kotliar, "Cluster dynamical mean field theory of the mott transition," *Phys. Rev. Lett.* **101** (2008) 186403.

[86] G. Rohringer, A. Toschi, H. Hafermann, K. Held, V. I. Anisimov, and A. A. Katanin, "One-particle irreducible functional approach: A route to diagrammatic extensions of the dynamical mean-field theory," *Phys. Rev. B* **88** (2013) 115112.

[87] G. Rohringer, A. Valli, and A. Toschi, "Local electronic correlation at the two-particle level," *Phys. Rev. B* **86** (2012) 125114.

[88] A. A. Katanin, A. Toschi, and K. Held, "Comparing pertinent effects of antiferromagnetic fluctuations in the two- and three-dimensional hubbard model," *Phys. Rev. B* **80** (2009) 075104.

[89] A. Georges, G. Kotliar, W. Krauth, and M. J. Rozenberg, "Dynamical mean-field theory of strongly correlated fermion systems and the limit of infinite dimensions," *Rev. Mod. Phys.* **68** (1996) 13–125.

[90] G. Kotliar and D. Vollhardt, "Strongly correlated materials: Insights from dynamical mean-field theory," *Phys. Today* **March** (2004) 53–59.

[91] M. Balzer, B. Kyung, D. Sénéchal, A.-M. S. Tremblay, and M. Potthoff, "First-order mott transition at zero temperature in two dimensions: Variational plaquette study," *Eur. Phys. Lett.* **85** (2009) 17002.

[92] A. Altland and B. Simons, *Condensed Matter Field Theory*. Cambridge University Press, Cambridge, 2006.

[93] K. Borejsza and N. Dupuis, "Antiferromagnetism and single-particle properties in the two-dimensional half-filled hubbard model: Slater vs. mott-heisenberg," *Eur. Phys. Lett.* **63** (2003) 722–728.

[94] V. I. Anisimov, J. Zaanen, and O. K. Andersen, "Band theory and mott insulators: Hubbard U instead of stoner I," *Phys. Rev. B* **44** (1991) 943–954.

[95] V. I. Anisimov, F. Aryasetiawan, and A. I. Lichtenstein, "First-principles calculations of the electronic structure and spectra of strongly correlated systems: the lda + u method," *Journal of Physics: Condensed Matter* **9** (1997) 767.

[96] M. Imada, A. Fujimori, and Y. Tokura, "Metal-insulator transitions," *Rev. Mod. Phys.* **70** (1998) 1039–1263.

[97] K. Held, O. K. Andersen, M. Feldbacher, A. Yamasaki, and Y.-F. Yang, "Bandstructure meets many-body theory: the LDA+DMFT method," *Journal of Physics: Condensed Matter* **20** (2008) 064202.

[98] A. Georges, "Strongly correlated electron materials: Dynamical mean-field theory and electronic structure," *AIP Conference Proceedings* **715** (2004) 3–74.

[99] I. V. Solovyev, "First-principles wannier functions and effective lattice fermion models for narrow-band compounds," *Phys. Rev. B* **73** (2006) 155117.

[100] H. Lee, K. Foyevtsova, J. Ferber, M. Aichhorn, H. O. Jeschke, and R. Valentí, "Dynamical cluster approximation within an augmented plane wave framework: Spectral properties of $srvo_3$," *Phys. Rev. B* **85** (2012) 165103.

[101] R. Eder, "Correlated band structure of NiO, CoO, and MnO by variational cluster approximation," *Phys. Rev. B* **78** (2008) 115111.

[102] R. Eder, "Spin-state transition in $LaCoO_3$ by variational cluster approximation," *Phys. Rev. B* **81** (2010) 035101.

[103] P. Blaha, K. Schwarz, P. Sorantin, and S. Trickey, "Full-potential, linearized augmented plane wave programs for crystalline systems," *Computer Physics Communications* **59** (1990) 399–415.

[104] O. K. Andersen and T. Saha-Dasgupta, "Muffin-tin orbitals of arbitrary order," *Phys. Rev. B* **62** (2000) R16219–R16222.

[105] J. Kunes, R. Arita, P. Wissgott, A. Toschi, H. Ikeda, and K. Held, "Wien2wannier: From linearized augmented plane waves to maximally localized wannier functions," *Computer Physics Communications* **181** (2010) 1888–1895.

[106] A. A. Mostofi, J. R. Yates, Y.-S. Lee, I. Souza, D. Vanderbilt, and N. Marzari, "wannier90: A tool for obtaining maximally-localised wannier functions," *Computer Physics Communications* **178** (2008) 685–699.

[107] J. C. Slater, "The theory of complex spectra," *Phys. Rev.* **34** (1929) 1293–1322.

[108] A. Liebsch, "Surface versus bulk coulomb correlations in photoemission spectra of $srvo_3$ and $cavo_3$," *Phys. Rev. Lett.* **90** (2003) 096401.

[109] T. Yoshida, K. Tanaka, H. Yagi, A. Ino, H. Eisaki, A. Fujimori, and Z.-X. Shen, "Direct observation of the mass renormalization in $srvo_3$ by angle resolved photoemission spectroscopy," *Phys. Rev. Lett.* **95** (2005) 146404.

[110] T. Yoshida, M. Hashimoto, T. Takizawa, A. Fujimori, M. Kubota, K. Ono, and H. Eisaki, "Mass renormalization in the bandwidth-controlled mott-hubbard systems $SrVO_3$ and $CaVO_3$ studied by angle-resolved photoemission spectroscopy," *Phys. Rev. B* **82** (2010) 085119.

[111] S. Itoh, "Electronic structure of SrVO3," *Solid State Communications* **88** (1993) 525–527.

[112] A. N. Rubtsov, V. V. Savkin, and A. I. Lichtenstein, "Continuous-time quantum monte carlo method for fermions," *Phys. Rev. B* **72** (2005) 035122.

[113] E. Gull, A. J. Millis, A. I. Lichtenstein, A. N. Rubtsov, M. Troyer, and P. Werner, "Continuous-time monte carlo methods for quantum impurity models," *Rev. Mod. Phys.* **83** (2011) 349–404.

[114] G. Koster, L. Klein, W. Siemons, G. Rijnders, J. S. Dodge, C.-B. Eom, D. H. A. Blank, and M. R. Beasley, "Structure, physical properties, and applications of $SrRuO_3$ thin films," *Rev. Mod. Phys.* **84** (2012) 253–298.

[115] E. Blount, "Solid state physics, formalisms of band theory," *Elsevier B.V.* **13** (1962) 305–373.

[116] N. Marzari, I. Souza, and D. Vanderbilt, "An introduction to maximally-localized wannier functions," *Psi-K Newsletter* **57** (2003) 129.

Acknowledgements

Ich möchte mich als erstes bei meinen Betreuern Ass.Prof. Dipl.-Ing. Dr.techn. Markus Aichhorn und Univ.-Prof. Dr.rer.nat. Enrico Arrigoni zur Verfügung dieses Themas für die sehr kompotente Betreuung und für die Geduld und für die sehr angenehme Arbeitsklima bedanken. Desweiteren möchte ich mich auch bei allen anderen Mitgliedern der Institut für Theoretische Physik - Computational Physics für die Unterstützung bedanken. Ich möchte mich auch bei den anderen Mitgliedern der Many Body Physics Group bedanken.

Bu vesileyle ailemede (özellikle küçük kardeşim Ismail'ede) teşekkür etmek isterim. Öğrenme hayatimda bana yaptiklari amansiz bitmek tükenmez katkilarindan dolayi.

This work was supported by the Austrian Science Fund (FWF) SFB-VICOM project F04103.